National Science Foundation
Under grants ATM-9529321 and ATM-9904218

A PDF-Based Parameterization for Boundary Layer Clouds

by Jean-Christophe Golaz

William R. Cotton, P.I.

Colorado State University

DEPARTMENT OF ATMOSPHERIC SCIENCE

PAPER NO. 715

A PDF-BASED PARAMETERIZATION FOR BOUNDARY LAYER CLOUDS

by

Jean-Christophe Golaz

Department of Atmospheric Science

Colorado State University

Fort Collins, Colorado 80523

Research Supported by

National Science Foundation

under Grants ATM-9529321 and ATM-9904218.

December 18, 2001

Atmospheric Science Paper No. 715

ABSTRACT

A PDF-BASED PARAMETERIZATION FOR BOUNDARY LAYER CLOUDS

A new parameterization for boundary layer clouds is presented. It is designed to be flexible enough to represent a variety of cloudiness regimes without the need for case-specific adjustments. The methodology behind the parameterization is the so-called assumed PDF method. The parameterization differs from traditional higher-order closure or mass-flux schemes in that it achieves closure by the use of a relatively sophisticated joint probability density function (PDF) of vertical velocity, temperature, and moisture. Because predicting the full subgrid-scale PDF is not feasible, a family of PDFs that is flexible enough to represent various cloudiness regimes is identified and used.

The methodology is as follows. Predictive equations for grid box means and a number of higher-order turbulent moments are advanced in time. These moments are in turn used to select a particular member from the family of PDFs, for each time step and grid box. Once a PDF member has been selected, the scheme integrates over the PDF to close higher-order moments, buoyancy terms, and diagnose cloud fraction and liquid water. Since all these are derived from a unique joint PDF, they are guaranteed to be consistent with one another.

Results from simulations of five different cases with the new parameterization are presented and contrasted with data simulated by large-eddy simulation (LES). The cases include a clear convective layer, trade-wind cumulus, cumulus clouds over land, marine stratocumulus and an intermediate and challenging regime of cumulus rising into stratocumulus.

The cloud cover in the cloudy cases varied widely, ranging from a few per cent cloud cover to nearly overcast. In each of the cloudy cases, the parameterization predicted cloud fractions that agree reasonably well with the LES. Typically, cloud fraction values tended to be somewhat smaller in the parameterization, and cloud base and top heights were slightly underestimated. Liquid water content was generally within 40% of the LES predicted values for a range of values spanning almost two orders of magnitude. This was accomplished without the use of any case-specific adjustments.

Jean-Christophe Golaz
Department of Atmospheric Science
Colorado State University
Fort Collins, Colorado 80523
Spring 2002

A la mémoire de mon Père.

ACKNOWLEDGEMENTS

First and foremost, I would like to thank my advisor, Dr. William R. Cotton for providing me with the unique opportunity to conduct graduate study in the Department of Atmospheric Science at Colorado State University. His guidance and support over the past four years have been immensely appreciated. I also would like to acknowledge my committee members Dr. David A. Randall and Dr. Wayne H. Schubert from the Atmospheric Science department, Dr. David A. Krueger from the Physics department and Dr. Chin-Hoh Moeng from NCAR.

Numerous people have helped making this work become a reality. In particular, I would like to acknowledge Dr. Vincent E. Larson whose ideas, suggestions, and contributions have been most helpful to this research. I also would like to thank past and current members of the Cotton group for their help, as well as for making the Cotton group a great working environment.

This research was supported by the National Science Foundation under grants ATM-9529321 and ATM-9904218.

TABLE OF CONTENTS

Chapter 1

Introduction

Boundary layer clouds play an important role in the energy and hydrological cycle of the atmosphere. Slingo (1990) showed, using a general circulation model, that small changes in low level cloud amount or cloud properties could significantly affect the global radiation budget. Using satellite observations, Hartmann et al. (1992) demonstrated that low level clouds, with 60% of the total cloud radiative forcing, are the largest contributors to the planetary net cloud forcing.

Boundary layer clouds affect the radiative budget so strongly in large part because of the contribution from marine stratocumulus clouds. Stratocumulus have extensive areal coverage. They overlie large portions of the eastern Pacific and eastern Atlantic oceans (e.g Cotton and Anthes 1989). They form at the edge of subtropical highs, in regions characterized by cold upwelling waters and large-scale atmospheric divergence that brings relatively warm and dry air near the cool and moist surface resulting in a marked inversion at the top of the marine boundary layer. Stratocumulus sharply reduce the net incoming shortwave radiation owing to their high albedo ($\approx$0.6-0.8) compared to the underlying ocean surface ($\approx$ 0.05), while at the same time leaving the longwave radiation to space essentially unaffected owing to their low altitude.

Stratocumulus have been a subject of research for nearly a century [see Stevens (1996) for an historical perspective]. The interest in stratocumulus has been heightened over the

past two decades by a necessity to understand how stratocumulus clouds might respond to global atmospheric changes. Twomey (1974) argued that an increase in cloud condensation nuclei (CCN) might alter the cloud droplet size distribution leading to an increase in cloud albedo. It has also been estimated that a 4% increase in the area covered by stratocumulus could results in a global cooling sufficient to offset the expected warming from a doubling in CO_2 concentration (Randall et al. 1984). Albrecht (1989) discussed the possibility that an increase in CCN concentration over the oceans might lead to a reduction in drizzle formation, resulting in an increase in low-level cloud amount. Ackerman et al. (1993) suggested a mechanism by which the depletion of CCN in stratocumulus clouds could lead to a collapse of the marine boundary layer, therefore affecting the radiative balance.

Since sheets of stratocumulus often break up into trade-wind cumulus layers with much lower albedo, it is important to be able to accurately predict which cloud regime is present. The trade-wind regime has also long been recognized as playing an important role in the general circulation (Riehl et al. 1951, and references therein). Using numerical simulations, Tiedtke et al. (1988) showed that large-scale circulations are sensitive to the parameterization of trade-wind cumulus. The areal coverage of active convective elements in the trades is typically of the order of a few per cents, while the total cloud cover might be significantly larger due to the presence of decaying elements (e.g. Albrecht 1981). As for stratocumulus, cloud cover in the trades might also be susceptible to aerosol concentrations. However, Ackerman et al. (2000) suggested that an opposite effect on cloud cover might take place in which absorption of solar radiation by dark aerosols could actually decrease the cloud coverage of the trade cumulus.

The transition from the stratocumulus-topped to the trade-wind cumulus layer is frequently regarded as involving a mixed regime, where cumulus clouds form underneath the stratocumulus deck. Krueger et al. (1995a,b) performed a two-dimensional Lagrangian

simulation of the subtropical marine boundary layer over the Pacific ocean southwest of California. The sea surface temperature (SST) was increased following the Lagrangian trajectory. Their results showed that the transition from the stratocumulus-topped boundary layer to the trade cumulus layer involved two intermediate stages. The first one was a deep, well-mixed stratus-topped boundary layer followed by a second stage of cumulus-under-stratus. This stage was characterized by a two-layer structure consisting of a well-mixed subcloud layer and a stratified cloud layer.

Wyant and Bretherton (1997) also studied the stratocumulus to cumulus transition using a two-dimensional Lagrangian model. A two-stage model consistent with their Lagrangian simulations was proposed. During the first stage, increased latent heat flux resulting from the larger SSTs induced a deepening and decoupling of the marine boundary layer. The large cloud fraction persisted after the decoupling occurred, but the cloudiness regime changed from a purely stratocumulus layer to episodic cumulus clouds rising into the stratocumulus deck. The second stage was characterized by more vigorous and deeper cumulus clouds. They penetrated deeper into the inversion layer, and as a result entrained more dry air from above the inversion. This entrainment of dry air caused the evaporation of the cumulus before they could detrain, leading to a progressive drying and dissipation of the overlying cloud deck.

Because boundary layer clouds have characteristic sizes that are much smaller than large-scale model grid boxes, they must be parameterized. Their incorporation in present-day numerical models continues to pose a significant challenge. Parameterizations have frequently been developed for specific cloudiness regimes. With this approach, boundary layer clouds are first classifieds into various categories, such as stratocumulus clouds or shallow cumulus clouds, and then specific components are developed for each regime. The

categorization into regimes is, however, somewhat arbitrary and leads to the difficult problem of interfacing the various components to obtain a general-purpose parameterization.

Below, we review some of the boundary layer cloud parameterization categories that have been proposed in the past. This review is not intended to be exhaustive, but rather to provide some basic information about various approaches to boundary layer parameterization and their associated difficulties.

One class of parameterizations used for boundary layer clouds are higher-order turbulence closure models. As of yet, no single turbulence closure model has succeeded in modeling both cumulus and stratocumulus regimes without case-specific adjustments. Bougeault (1981a,b) developed a higher-order closure scheme coupled with a statistical representation of the subgrid-scale cloudiness. He used the scheme to simulate a trade-wind cumulus layer observed during the Puerto Rico Experiment. However, in order to model a different regime like a marine stratocumulus layer, Bougeault (1985) changed the statistical cloudiness scheme and the representation of the mixing length from the ones in his original model.

Similarly, low-order closure schemes have been used quite successfully to simulate stratocumulus layers (e.g Chen and Cotton 1987; Duynkerke and Driedonks 1987, 1988; Bechtold et al. 1992), but Bechtold et al. (1995) showed that the closure assumptions had to be modified in order to simulate trade-wind cumulus. They found that a statistical subgrid-scale cloudiness scheme using a Gaussian distribution was well suited for stratocumulus clouds but that a positively skewed distribution was necessary to represent cumulus convection, implying that different variants of the subgrid-scale cloudiness scheme were needed for different cloud regimes, similarly to the findings of Bougeault (1985).

Another category of parameterizations is mass-flux models. Following Arakawa and Schubert (1974), such models simulate subgrid-scale convection by representing cloud en-

sembles as one-dimensional plumes embedded in the environment. Some large-scale models have incorporated mass-flux parameterizations for shallow convection, such as trade-wind cumulus clouds. (e.g. Tiedtke 1989; Gregory and Rowntree 1990).

Since mass-flux parameterizations typically only handle convective clouds, models incorporating them include alternate schemes to account for other boundary layer cloud regimes. Lock et al. (2000) presented a parameterization consisting of various schemes coupled together, including a mass-flux convection scheme for cumulus layers, a nonlocal eddy-viscosity scheme for mixed layers, and a cloud-top entrainment parameterization. A total of six possible boundary layer regimes are identified, and a set of rules based on stability of the mean profiles and parcel buoyancy is used to activate the appropriate components of the parameterization at any given time. Although they found that the parameterization was "capable of switching reasonably smoothly and realistically between the different regimes", the use of trigger functions to decide which schemes to activate is a somewhat artificial idealization of how nature behaves, and it has not been fully established that a simple set of rules can trigger the correct scheme under the full set of conditions.

Lappen and Randall (2001a,b,c) simulated various cloudiness regimes with a single scheme that unifies mass-flux and higher-order closure approaches. The mass-flux approach was used to decompose the boundary layer into updraft and downdraft plumes, and in turn this decomposition was related to the turbulence moments as originally proposed in Randall et al. (1992). This is equivalent to assuming a double delta function PDF. Lappen and Randall improved upon this distribution by adding subplume variability in the up- and downdrafts. Their new scheme was applied to simulate a dry convective boundary layer, a trade-wind cumulus layer and stratocumulus-topped layer. The simulation of the dry convective layer and the stratocumulus case agreed well with observations, but the trade-wind cumulus simulation produced cloud fraction and liquid water values too large compared to

the observations. For the trade-wind case, the model also generated non-zero liquid water in both up- and downdrafts plume, amounting to an overcast layer at the top of the cumulus layer, in contrast to the observations.

In the present work, we propose a new scheme that is different from either mass-flux schemes or traditional higher-order moment schemes. The focus of our proposed scheme is not the separate prediction of cumulus mass-flux, turbulent moments, cloud cover, and other desired predictands *per se*. Rather, the focus is the prediction of the joint PDF of vertical velocity, temperature, and moisture content. This joint PDF varies in space and evolves in time. The joint PDF can be viewed as a more fundamental quantity than the mass flux, turbulent moments, and cloud cover, because the latter quantities can be diagnosed once the joint PDF is known. Explicitly predicting the shape of the PDF is not feasible, so we instead assume a functional form for the PDF. We choose a double Gaussian family of PDFs proposed by Larson et al. (2001c). The problem then reduces to the selection of a particular member from the family of PDFs for each grid box and time step. PDFs have been used in the past to parameterize subgrid-scale moisture variations to account for partial cloud cover (e.g. Sommeria and Deardorff 1977; Mellor 1977; Bougeault 1981a; Chen and Cotton 1987). They also have been used for the representation of cloudiness associated with deep convection (e.g. Xu and Randall 1996; Bony and Emanuel 2001). We extend the approach to all turbulent moments involving vertical velocity, temperature and moisture perturbations.

Our parameterization can be regarded as a traditional higher-order closure model that uses a new closure based on a double Gaussian family of PDFs. Alternatively, our parameterization can be regarded as an extension of Lappen and Randall's model, in which the double delta function PDF they used for closure is generalized to a double Gaussian PDF.

The generalization is inspired by the fact that Larson et al. (2001c) evaluated the performance of several families of joint PDFs and found that atmospheric PDFs resemble double Gaussians more than double delta functions.

The construction of the parameterization follows the so-called "assumed PDF method" in which the subgrid-scale variability of vertical velocity, temperature and moisture is represented using the pre-selected family of joint PDFs. The family of PDFs retained for this work depends on ten free parameters. These parameters are determined at each grid point and time step from the mean values of the vertical velocity (w), the liquid water potential temperature (θ_l), the total water specific humidity (q_t), the second-order moments as well as the third-order moment of the vertical velocity. Filtered moment equations are integrated in space and time to yield the evolution of these moments. Each model time step consists of three stages:

- Advance the prognostic equations for the mean and higher-order moments.
- Using these moments, select a specific member from the underlying family of PDFs.
- Compute cloud fraction, liquid water, and close higher-order turbulent moments by analytical integration over the PDF.

The parameterization is implemented in a single-column model (SCM) framework. It is tested against LES results for five different cases. They consist of a dry convective layer, a trade-wind cumulus layer, a continental cumulus layer, a stratocumulus-topped boundary layer, and a transitional layer of cumulus-under-stratus. The clear boundary layer is based on data collected during the Wangara experiment. The four cloudy cases are all based on GEWEX Cloud Study System (GCSS) boundary layer cloud intercomparison workshops. These cases were chosen because they represent a very large range of cloud fraction and

liquid water values. The parameterization is identically configured for each simulation, and no case-specific adjustments are performed.

This dissertation is organized as follows. In Chapter 2, we introduce the LES model used. We also present the five different test cases and give an overview of the LES results. In Chapter 3, we give a detailed description of the assumed PDF method and describe the construction of the SCM. Chapter 4 presents results comparing the LES and SCM for the selected test cases. We finish with some concluding remarks and suggestions for future research in Chapter 5.

Chapter 2

LES simulations of boundary layer clouds

2.1 Overview

LES models have been widely used as numerical tools to study the evolution of the atmospheric planetary boundary layer (e.g. Deardorff 1972; Moeng 1984). These models have the capability to explicitly resolve the large-scale turbulent eddies in the boundary layer while parameterizing the effect of the smaller, unresolved and less energetic eddies. To resolve the large-scale eddies, typical grid spacings used in LES are of the order of 100 m or less. A critical review of this modeling approach can be found in Mason (1994).

Many LES studies have focused on the structure of turbulence and statistical properties of clear convective boundary layers (e.g. Deardorff 1974; Moeng and Wyngaard 1984, 1988; Schmidt and Schumann 1989). Other have focused on marine stratocumulus-topped boundary layers (e.g. Stevens 1996; Moeng et al. 1996, and references therein) and cumulus boundary layers (e.g. Cuijpers and Duynkerke 1993; Cuijpers et al. 1996; Brown 1999, among others).

LESs have also been used extensively in this work and have proven to be an invaluable research tool. The use of LES here is twofold: (i) to provide high resolution numerical data needed for testing different families of PDFs for a variety of boundary layer regimes (see chapter 3), and (ii) to perform a detailed evaluation of the performance of the new

single-column model (see chapter 4).

The LES model selected for these purposes is the Regional Atmospheric Modeling System (RAMS) (Pielke et al. 1992; Cotton et al. 2002). It is non-hydrostatic and compressible. As customary in LES models, periodic boundary conditions are imposed in the horizontal directions. The subgrid-scale fluxes are computed following Deardorff (1980) using a prognostic equation for the subgrid-scale turbulence kinetic energy. Because the cloudy boundary layer cases retained in this work are non-precipitating, condensation is simply accounted for by a saturation adjustment scheme in which cloud water is diagnosed as the difference between total water and saturation mixing ratio. More sophisticated options, including a single-moment and two-moment microphysical schemes (Walko et al. 1995; Meyers et al. 1997) are available but were not used.

A total of five boundary layer cases have been selected for this work. They consist of a clear convective layer, a trade-wind cumulus layer, cumulus clouds over land, a stratocumulus-topped marine boundary layer and a mixed case of cumulus rising underneath a broken stratocumulus deck. The clear boundary layer is based on data collected during day 33 of the Wangara experiment. The four cloudy cases are all based on GCSS Working Group 1 intercomparison workshops. These cases were chosen because taken together, they span a very large range of cloudiness regimes as well as cloud fraction and liquid water values.

Although we do compare the SCM developed as part of this work with observational data from the Wangara field experiment, we compare the SCM mostly with numerical simulations. We have chosen to do so for several reasons. First, we want to test the SCM with data whose forcings,

initial conditions, and boundary conditions are identical to the LESs. This eliminates initialization and forcing uncertainties from the evaluation of the performance of the SCM.

Second, we want to compare the SCM with vertical profiles of higher-order moments, which are difficult to obtain from observational data. We also want to focus specifically on the parameterization's ability to predict turbulence statistics and cloud water, while excluding complications such as precipitation and land surface inhomogeneities. We can accomplish this by using GCSS intercomparison cases. They were specifically designed to be used as test beds for parameterizations. These simulations are based loosely on observed cases and therefore simulate realistic scenarios. In the next section, we give a brief overview of these five cases.

2.2 Case studies

2.2.1 Dry convective layer (Wangara)

The Wangara[1] experiment took place in Australia during the months of July and August 1967 and is described in Clarke et al. (1971). The main goal of this field experiment was to study the influence of cold fronts and squall lines on the vertical flux of angular momentum in the west wind belts of the world. A secondary objective was to provide data for more adequate description of the boundary layer.

The center of the experiment was a large area of flat land with low vegetative cover located in Hay, N.S.W. (34° 30′S., 144° 56′E.). Four additional measurement stations were located approximately at the corners of a square of side 60 km. (Fig. 2.1). Observations included hourly balloon wind profiles at the five stations and radiosonde temperatures and mixing ratios at three hours interval at the central station.

We choose day 33 of the field experiment, which has been selected by many prior authors (e.g Deardorff 1974; André et al. 1978; Lappen and Randall 2001c) because clear skies and little horizontal heat and moisture advection were present. The LES is initialized

[1] Australian Aboriginal for "west wind"

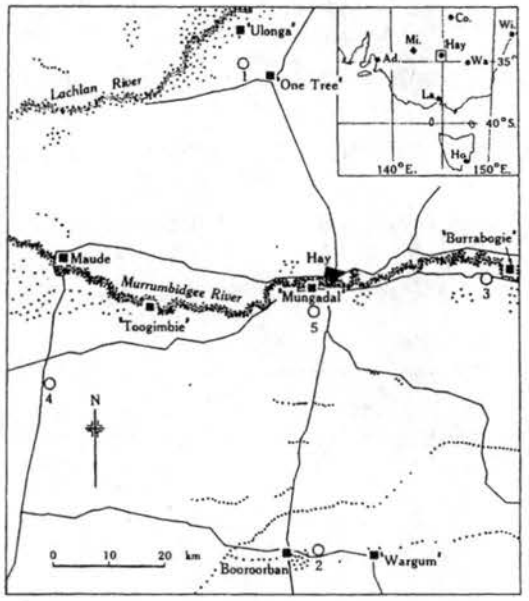

Figure 2.1: Location of the five sites for the Wangara experiment. From Clarke et al. (1971).

with profiles of horizontal winds, potential temperature, and water vapor measured on 16 August 1967 at 0900 Local Standard Time (LST), approximately two hours after sunrise. We simulate eight hours of turbulence evolution in order to capture the daytime growth of the boundary layer. Surface sensible and latent heat fluxes are prescribed as functions of time as in André et al. (1978):

$$\overline{w'\theta'}(t) = 0.18 \cos\left(\frac{t - 45000}{36000}\pi\right) \qquad \left[\frac{\text{Km}}{\text{s}}\right] \tag{2.1}$$

$$\overline{w'q_t'}(t) = 1.3 \times 10^{-4} \ \overline{w'\theta'}(t) \qquad \left[\frac{\text{m}}{\text{s}}\right] \tag{2.2}$$

where t is in seconds from 0000 LST on 16 Aug 1967. No radiation is imposed. Details of the simulation set-up are given in Table 2.1.

The observed and LES profiles of potential temperature are shown in Fig. 2.2. A convective mixed-layer forms and deepens during the course of the day. The mixed-layer potential temperature differs between the observations and LES by only a fraction of a

Table 2.1: LES setup and forcings for the Wangara experiment.

Surface heat fluxes	Prescribed, Eqs. (2.1) and (2.2)
Radiative cooling	None
Large-scale advection	None
Large-scale subsidence	None
Surface pressure	1023 (hPa)
Start of simulation	16 August 1967, 0900 LST
Length of simulation	8 hours
LES: time step	$\Delta t = 2$ s
grid spacing	$\Delta x = \Delta y = 100$ m; $\Delta z = 40$ m
domain size	$N_x = N_y = 53$; $N_z = 50$
Case references:	Clarke et al. (1971); Deardorff (1974).

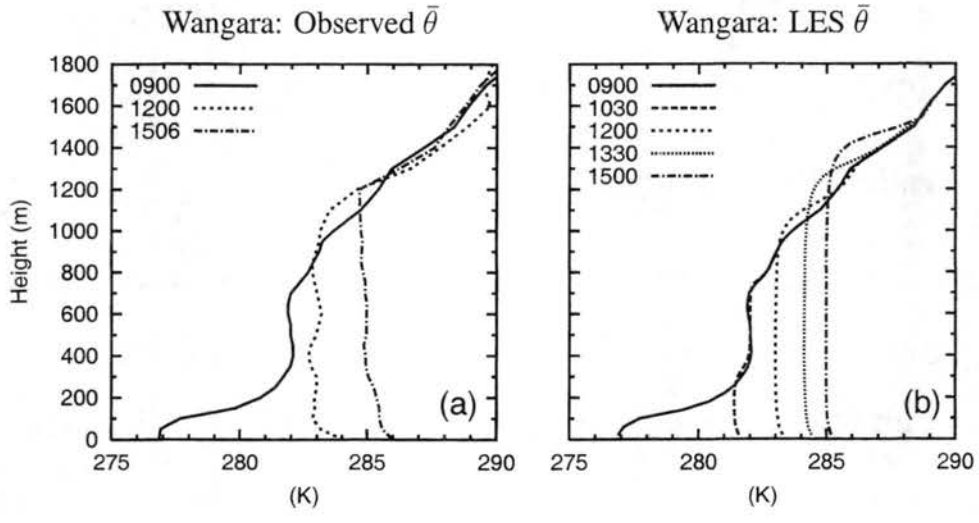

Figure 2.2: Observed (a) and LES (b) profiles of potential temperature for the Wangara experiment at various times (LST).

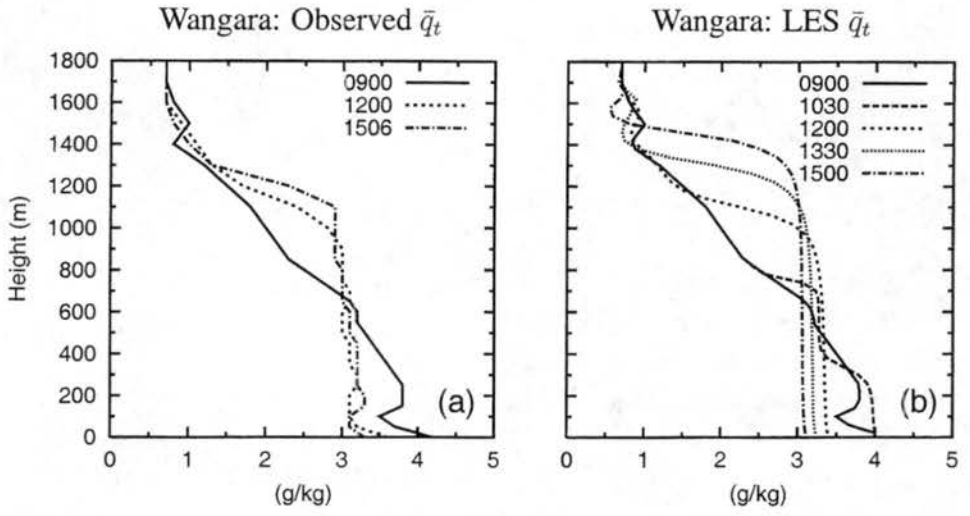

Figure 2.3: Same as Fig. 2.2 but for total water specific humidity.

degree, both at 1200 and 1500 LST. The mixed-layer top is almost identical at 1200 LST but is too high in the LES at later times. Deardorff (1974) observed a similar difference and attributed it to a possible overestimation of the surface fluxes and the lack of imposed large-scale vertical motion. The water vapor profiles (Fig. 2.3) follow a similar pattern. The LES profile at 1200 LES is comparable to the observations, but the deepening of the boundary layer is exaggerated at later times.

2.2.2 Trade-wind cumulus (BOMEX)

The trade-wind cumulus simulation is derived from the Barbados Oceanographic and Meteorological Experiment (BOMEX), which took place on 22-30 June 1969 (Holland and Rasmusson 1973). The simulation set-up is based on the fourth GCSS boundary layer clouds intercomparison workshop. The LES is initialized with profiles of horizontal winds, temperature, and moisture and run for six hours. Details of the experiment are given in Table 2.2. A complete specification of the case and comparison of the results produced by numerous cloud resolving models can be found in Siebesma et al. (2001). The LES results presented here used a newer version of RAMS that corrected the problems mentioned in

Table 2.2: Models setup and forcings for BOMEX.

Surface heat fluxes	$\overline{w'\theta'} = 8 \times 10^{-3}$ (Km/s), $\overline{w'q_t'} = 5.2 \times 10^{-2}$ (m/s).
Radiative cooling	Prescribed as a function of height
Large-scale advection	Prescribed as a function of height
Large-scale subsidence	Imposed
Surface pressure	1015 (hPa)
Length of simulation	6 hours
LES: time step	$\Delta t = 1.5$ s
grid spacing	$\Delta x = \Delta y = 100$ m; $\Delta z = 40$ m
domain size	$N_x = N_y = 64$; $N_z = 75$
Case reference:	Siebesma et al. (2001).

Siebesma et al. (2001). The newer simulation shows considerably less temporal variations in all the fields. The profile of $\overline{w'^2}$ in the subcloud layer is also now in good agreement with the other LES models.

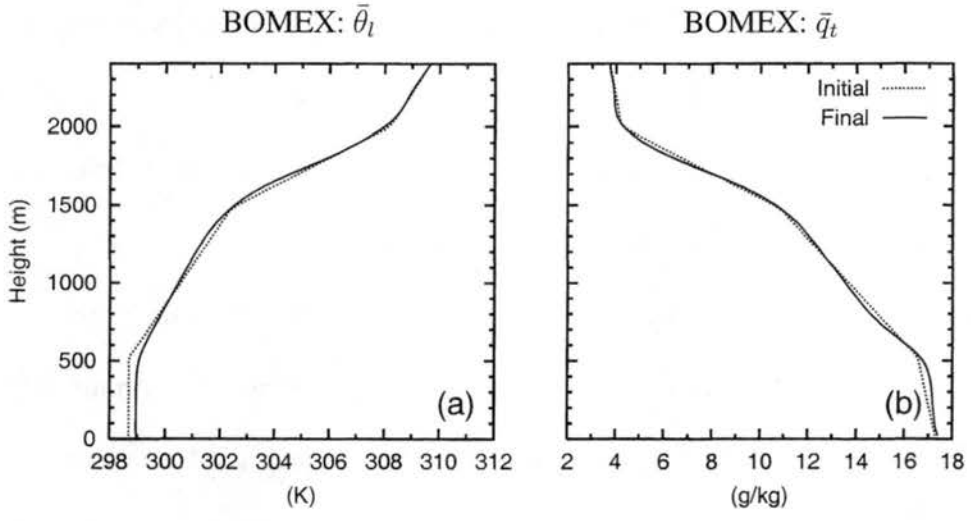

Figure 2.4: LES initial and final profiles of liquid water potential temperature (a) and total water specific humidity (b) for BOMEX.

The initial profiles of liquid water potential temperature and total water specific humidity are shown in Fig. 2.4. They consist of the three layers typically found in trade-wind cumulus: a mixed-layer from the surface up to 500 m, a conditionally unstable layer from 500 to 1500 m, and a stable layer between 1500 and 2000 m (Siebesma and Cuijpers 1995).

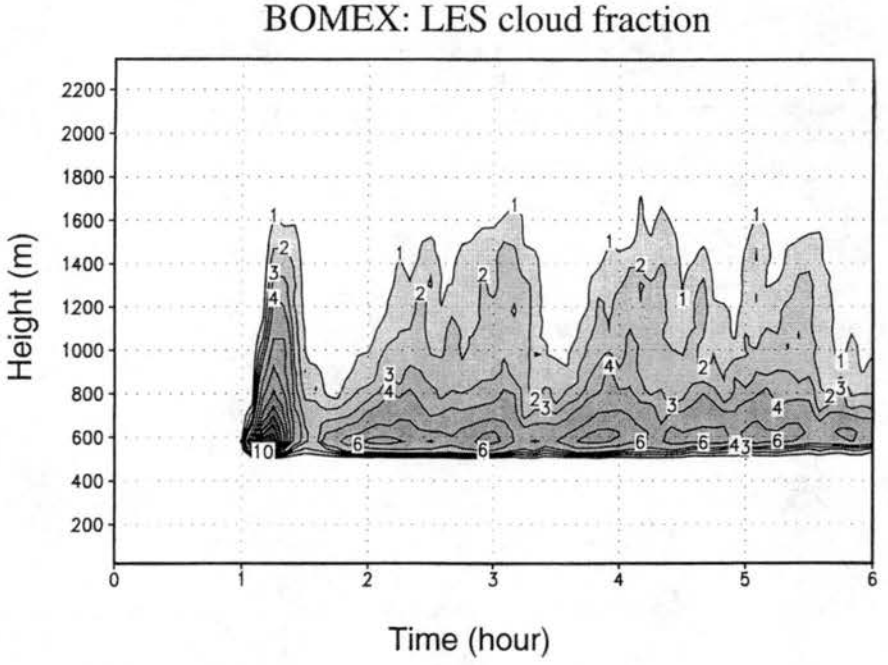

Figure 2.5: Time evolution of the LES cloud fraction (%) for BOMEX.

Also shown in Fig. 2.4 are the profiles at the end of the six hours simulation. They are almost identical to the initial conditions, reflecting a near steady-state regime. This is because the intercomparison case was designed so that the surface fluxes are balanced by the vertically-integrated large-scale forcings (Siebesma et al. 2001).

The evolution of the LES cloud fraction during the course of the simulation is depicted in Fig. 2.5. The first clouds form approximately one hour after the beginning of the run with an initial burst of convection that produces cloud fraction values as high as 18%. The cloud fraction diminishes later in the simulation and becomes steadier, although some intermittency persists. Such temporal fluctuations were also observed in other LES models, and a three hours time average period (between hour 3 and 6) was chosen to analyze the results (Siebesma et al. 2001).

The average cloud fraction and liquid water during this period is shown in Fig. 2.6. The cloud fraction peaks near cloud base with a value of 6.5% and then decreases sharply with height. Liquid water also maximizes near cloud base, but the decrease with height

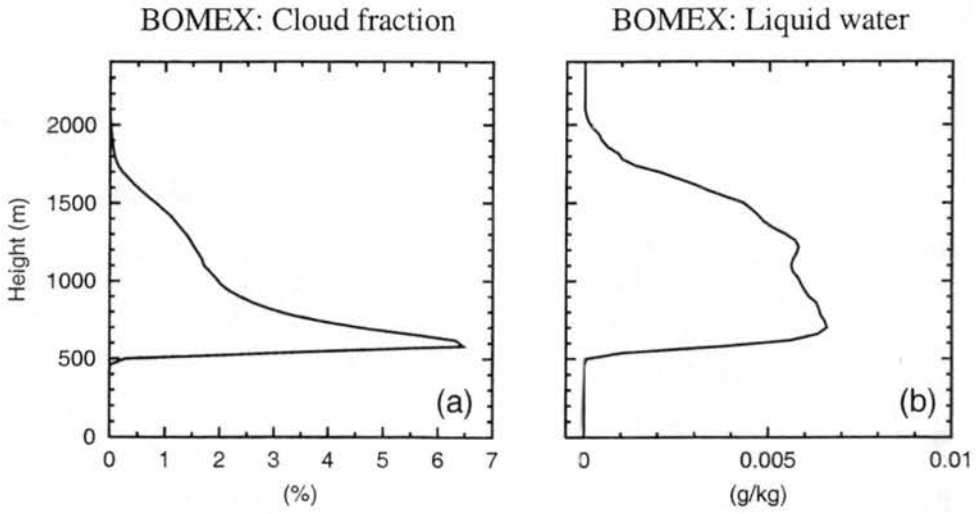

Figure 2.6: LES profiles of cloud fraction (a) and liquid water (b) averaged over the last three hours of the BOMEX simulation.

is less sharp between 600 and 1600 m. This indicates that, on average, clouds have a liquid water profiles that increase with height in this layer, as a similar liquid water amount occupies a much smaller surface area. Note also that the domain-averaged cloud water values are extremely small (< 0.007 g kg^{-1}). Parameterizations typically have difficulties representing such low liquid water amounts.

2.2.3 Cumulus over land (ARM)

In addition to the trade-wind cumulus case, we also use a continental cumulus cloud case. The simulation is based on the sixth GCSS boundary layer clouds intercomparison workshop, which focused on a case of daytime, non-precipitating cumulus clouds over land developing on top of an initially clear convective boundary layer. The case was based on observations taken from the Southern Great Plains (SGP) Atmospheric Radiation Measurement (ARM) site on 21 June 1997. A complete description of the intercomparison case can be found in Brown et al. (2002). We will only briefly outline some key features here. The models were initialized at 1130 Universal Time Coordinate (UTC) (530 LST) with profiles of potential temperature, total water mixing ratio, and horizontal winds that were idealized

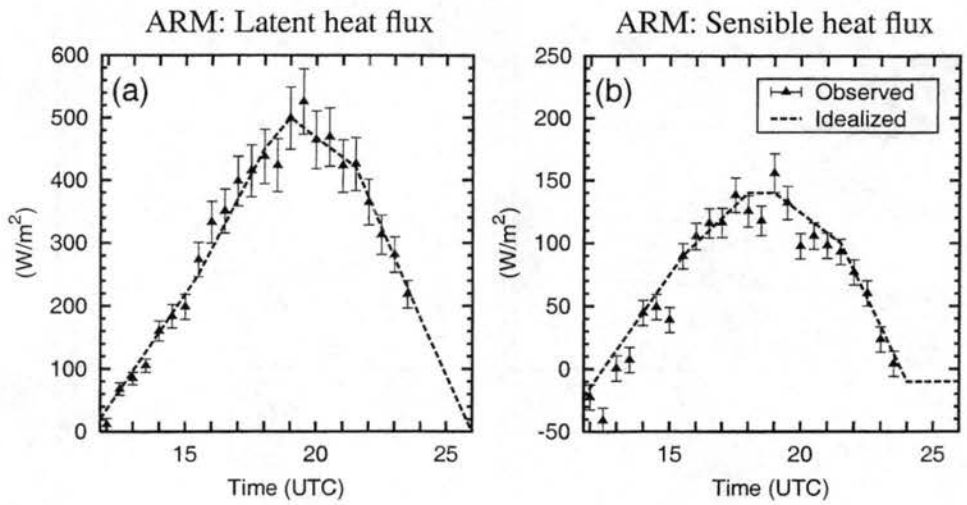

Figure 2.7: Time evolution of observed and idealized surface latent heat flux (a) and sensible heat flux (b) for the ARM case. The idealized fluxes are used to force the LES model.

from observed soundings at the ARM site. Time-varying surface latent and sensible heat fluxes derived from observations were used to force the models (Fig. 2.7). The latent heat flux reaches a maximum value of 500 W m^{-2}, and the sensible flux a much smaller value of 140 W m^{-2}. Large-scale heat and moisture forcings intended to mimic advective and radiative forcings were also imposed, but no interactive radiation transfer calculation was used. Results from the intercomparison workshop and a series of sensitivity experiments (Golaz et al. 2001) have shown that RAMS compared favorably with other models and observations. Table 2.3 gives details of the model configuration.

This case complements BOMEX nicely. In contrast to BOMEX, the clouds have larger values of cloud fraction and liquid water, and are much more strongly forced by surface heating. These clouds also exhibit a diurnal cycle which represents an additional challenge for parameterizations.

The time evolution of the cloud fraction is shown in Fig. 2.8. The first cumulus clouds form at the top of the convective layer around 1530 UTC. Cloud base steadily rises throughout the course of the day from 750 m to approximately 1300 m at 0300 UTC when the last

Table 2.3: Models setup and forcings for ARM.

Surface heat fluxes	Prescribed as a function of time based on observations.
Radiative cooling	Prescribed as a function of height
Large-scale advection	Prescribed as a function of height
Large-scale subsidence	None
Surface pressure	970 (hPa)
Start of simulation	21 June 1997, 1130 UTC
Length of simulation	14.5 hours
LES: time step	Δt between 1 and 5 s
grid spacing	$\Delta x = \Delta y = 100$ m; $\Delta z = 40$ m
domain size	$N_x = N_y = 67$; $N_z = 110$
Case reference:	Brown et al. (2002).

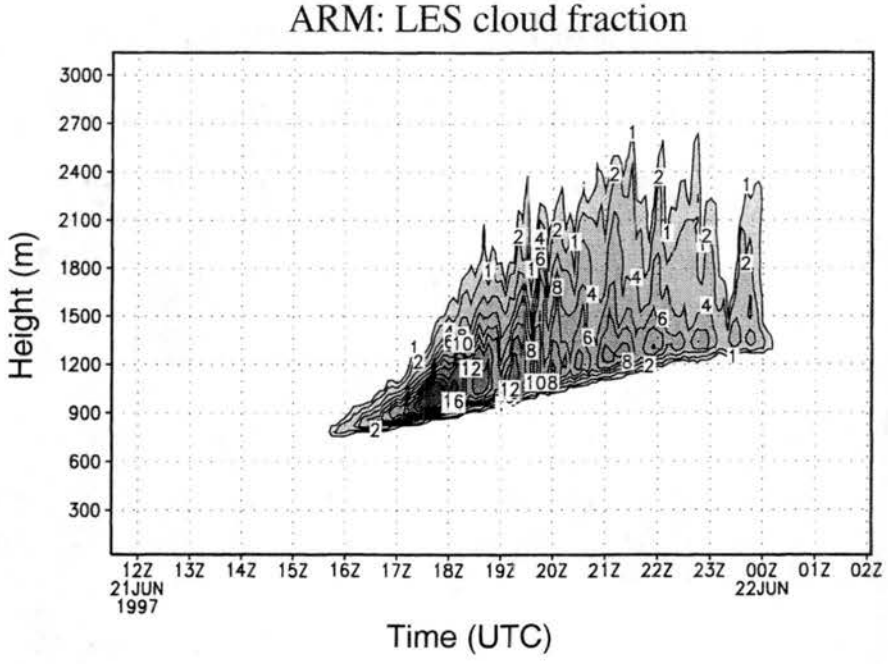

Figure 2.8: Time evolution of the LES cloud fraction (%) for the ARM simulation.

clouds dissipate. As in BOMEX, the LES cloud fraction exhibits some time fluctuations. The maximum value of 22% occurs two hours after the first clouds appear and later decreases as the clouds grow taller, with maximum values of the order of 10 to 12%.

2.2.4 Stratocumulus (FIRE)

For stratocumulus, we use the case based on the first GCSS boundary layer clouds intercomparison workshop. It is based on 7 July 1987 data collected during the First ISCCP Regional Experiment (FIRE) that took place off the coast of California. The initial soundings are based on the solid stratocumulus National Center for Atmospheric Research (NCAR) Electra aircraft measurements reported in Betts and Boers (1990), but are idealized for the purpose of the intercomparison. Detailed description of the intercomparison case and analysis of LES output are given in Moeng et al. (1996). Intercomparisons between one-dimensional codes and LESs are presented in Bechtold et al. (1996). The idealized case is a nighttime case with no drizzle, no solar radiation, little wind shear and little surface heating. Turbulence in the boundary layer is mainly generated by longwave cooling at cloud top. A very simple longwave radiative transfer model based on liquid water path is used:

$$F_{\text{rad}}(z) = F_0 \exp\left(-\kappa \int_0^\infty \rho(z')q_l(z')dz'\right) \tag{2.3}$$

where ρ is the basic state density and q_l the liquid water. The constants are $F_0 = 74$ (W/m^2) and $\kappa = 130$ (m^2 kg^{-1}). This simple radiative model has been used other intercomparison studies (e.g. Duynkerke et al. 1999; Stevens et al. 2001). Other details of the simulation set-up are given in Table 2.4.

The initial profiles of dry potential temperature, total water, and liquid water specific humidity are depicted in Fig. 2.9. The initial boundary layer is approximately 700 m deep and is capped by a strong temperature and moisture jump as is typical in stratocumulus. The initial diagnosed cloud water maximizes at cloud top with a value of 0.55 g kg^{-1}.

Table 2.4: Models setup and forcings for FIRE.

Surface heat fluxes	Bulk aerodynamic formulas, SST = 288 K.
Radiative cooling	LW based on liquid water path [Eq. (2.3)]. No SW radiation.
Large-scale advection	None
Large-scale subsidence	Imposed at 5×10^{-6} s^{-1}.
Surface pressure	1000 (hPa)
Length of simulation	3 hours
LES: time step	$\Delta t = 2$ s
grid spacing	$\Delta x = \Delta y = 50$ m; $\Delta z = 25$ m
domain size	$N_x = N_y = 60$; $N_z = 48$
Case references:	Moeng et al. (1996); Bechtold et al. (1996).

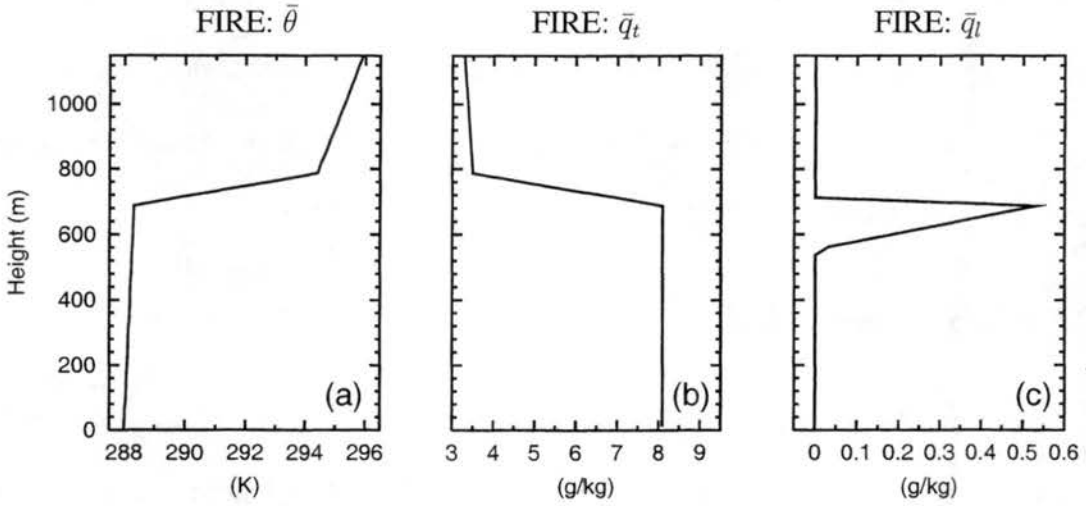

Figure 2.9: Initial profiles of dry potential temperature (a), total water (b) and liquid water specific humidity (c) for the FIRE simulation.

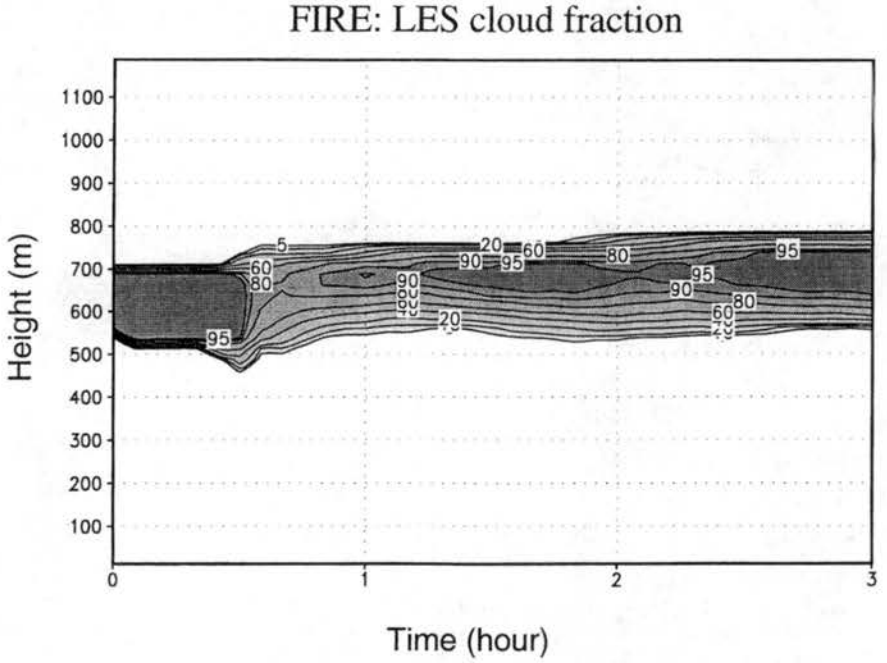

Figure 2.10: Time evolution of the LES cloud fraction (%) for FIRE.

The LES was run for a total of three hours, one additional hour compared to the GCSS intercomparison to allow for the model to reach a stable steady-state regime. An example of the time evolution of the LES is given by the cloud fraction shown in Fig. 2.10. The solid stratocumulus deck is maintained during the course of the simulation. Cloud top rises slightly to just under 800 m at the end of the three hours, despite the presence of an imposed large-scale subsidence.

2.2.5 Mixed-case (ATEX)

The last reference case selected is a case of trade-wind cumulus clouds under a strong inversion. It is the fifth GCSS intercomparison case and is based on data collected during the Atlantic Trade Wind Experiment (ATEX) which took place in February 1969 (e.g Augstein et al. 1973, 1974; Brümmer et al. 1974). Most of the measurements taken during ATEX were from three ships located in the Atlantic northeast trade-wind region during a three weeks period.

The intercomparison case is described in Stevens et al. (2001). It represents an intermediate case between (i) a regime with large cloud fraction and a shallow boundary layer capped by a strong inversion such as the FIRE stratocumulus case, and (ii) a regime with low cloud fraction and relatively deep boundary layer capped by a weak inversion, like the BOMEX trade-wind cumulus.

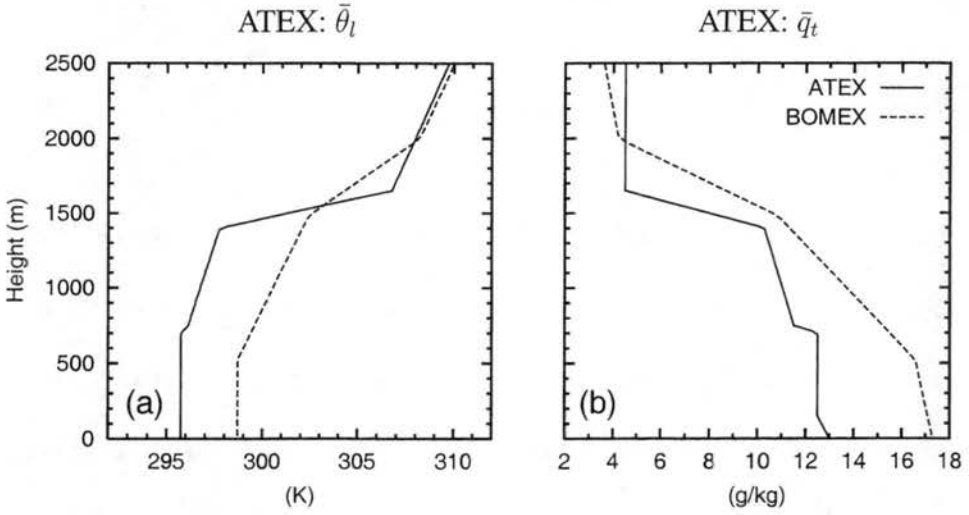

Figure 2.11: LES initial and final profiles of liquid water potential temperature (a) and total water specific humidity (b). Initial ATEX profiles are shown with solid lines and initial BOMEX profiles are plotted with dashed line for comparison.

The initial profiles of $\bar{\theta}_l$ and $\bar{q}_t$ are shown in Fig. 2.11 and compared with the initial BOMEX soundings. The larger SSTs of BOMEX compared to ATEX are reflected in the profile differences. The ATEX case also has a shallower boundary layer capped by a much stronger inversion than BOMEX.

The LES simulation was run for a total of 8 hours. Large-scale forcings and subsidence were imposed except during the first 5400 s of the simulation. Longwave radiative cooling was also imposed using Eq. 2.3. Other details of the simulation set-up are given in Table 2.5.

Unlike the other GCSS intercomparison cases presented previously, the interpretation

Table 2.5: Models setup and forcings for ATEX.

Surface heat fluxes	Bulk aerodynamic formulas, SST = 298 K.
Radiative cooling	LW based on liquid water path [Eq. (2.3)]. No SW radiation.
Large-scale advection	Imposed after 5400 s
Large-scale subsidence	Imposed after 5400 s
Surface pressure	1015 (hPa)
Length of simulation	8 hours
LES: time step	Δt = 1-2 s
grid spacing	$\Delta x = \Delta y = 100$ m; $\Delta z = 20$ m
domain size	$N_x = N_y = 64$; $N_z = 150$
Case references:	Stevens et al. (2001).

of LES results for the ATEX case is complicated by the fact that various LESs had results with widely different cloud fraction. They ranged from just under 20% to nearly overcast. The difference in cloud fraction was largest in the detrainment region just below the inversion where a stratiform cloud layer formed. The amount of condensate in this layer also exhibited large differences between the various models. Differences below this region were smaller and all models were predicting comparable cumulus convection. The longwave radiative feedback at the top of the stratiform cloud layer is likely to have played a large role in the cloud fraction sensitivity by amplifying smaller differences among the simulations (Stevens et al. 2001). It was further found that the cloud fraction was not only sensitive to a particular model's numerics, but also to the horizontal and vertical grid spacings.

Figure 2.12 shows the time evolution of the cloud fraction during the eight hours of the simulation produced by the RAMS LES. Two layers can be distinguished. Between 700 m and approximately 1300 m, the cloud fraction is small, typically below 5%, reflecting cumulus clouds. This layer is topped by a stratiform cloud with much higher cloud cover, up to 40%. The presence of a dual regime of cumulus clouds rising underneath a broken stratocumulus-like layer makes the ATEX case a particularly challenging one for testing parameterizations.

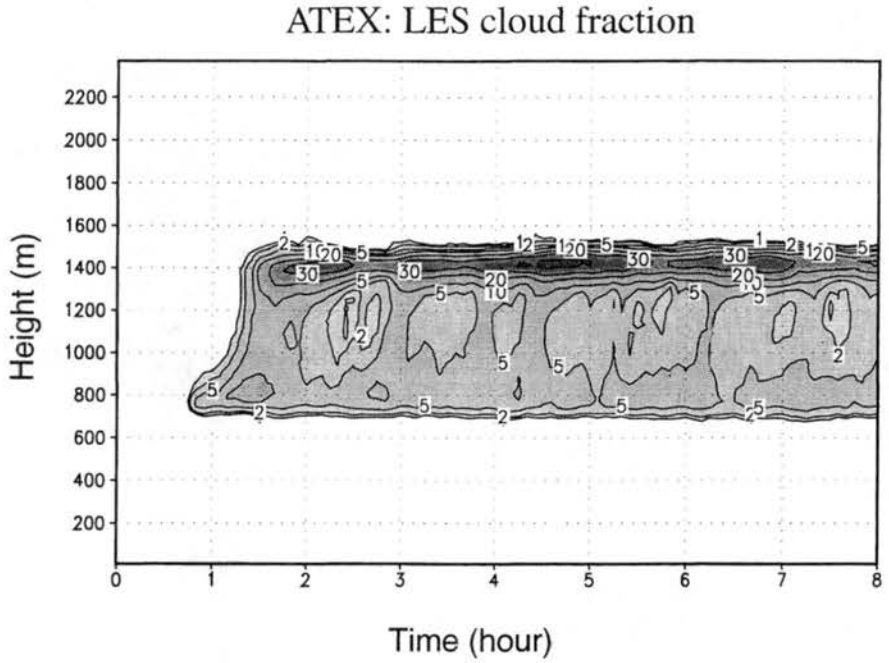

Figure 2.12: Time evolution of the LES cloud fraction (%) for ATEX.

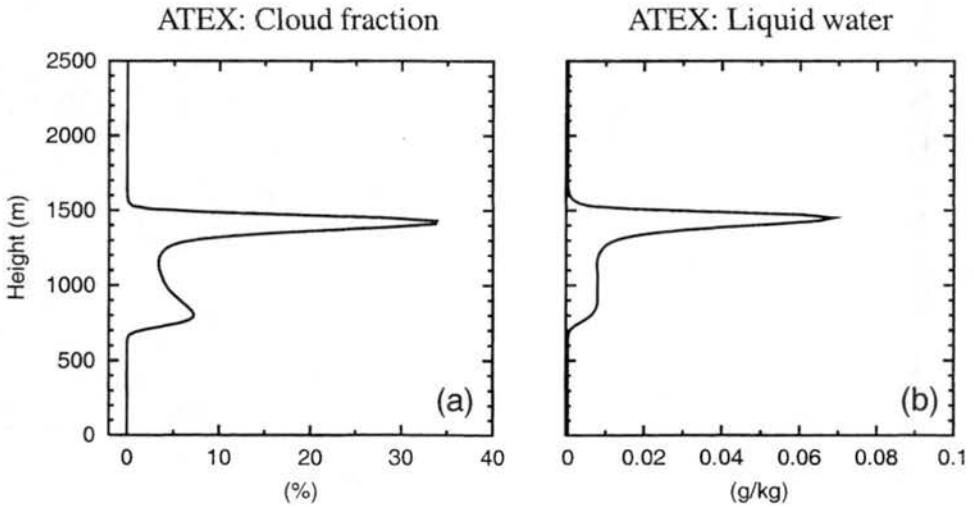

Figure 2.13: LES profiles of cloud fraction (a) and liquid water (b) averaged over the last five hours of the ATEX simulation.

The results of the LES are analyzed over the last five hours of the simulation. Cloud fraction and liquid water averaged over this time period are shown in Fig. 2.13. The cumulus and broken stratiform cloud layers can clearly be identified. Cloud fraction in the cumulus layer maximizes near cloud base with a value of 8%. The maximum cloud fraction in the stratiform layer is approximately 35%. The liquid water content is of the order of 0.01 g kg^{-1} in the cumulus layer and increases to 0.07 g kg^{-1} near the top of the stratiform region. The RAMS results lie approximately in the middle of the range of cloud fraction and liquid water values predicted by the GCSS intercomparison participants (see Stevens et al. 2001, their Figs. 3a and 7a).

Chapter 3

A new single-column model

3.1 The assumed PDF method

3.1.1 General description

We denote the joint PDF of vertical velocity w, liquid water potential temperature θ_l, and total specific water content q_t by $P(w, \theta_l, q_t)$. If $P(w, \theta_l, q_t)$ is a joint PDF, then $P(w, \theta_l, q_t)\, dw\, d\theta_l\, dq_t$ is the probability of obtaining a value of (w, θ_l, q_t) within the range $(w - dw/2) < w < (w + dw/2)$, $(\theta_l - d\theta_l/2) < \theta_l < (\theta_l + d\theta_l/2)$, and $(q_t - dq_t/2) < q_t < (q_t + dq_t/2)$ at a specific location and time. For the purpose of this work, we are interested in the joint PDF associated with a particular model grid box and time step. The joint PDF then becomes a characterization of the unresolved subgrid variations that occur within this particular box. However, the PDF does not provide any information about the spatial organization of this variability within the box of interest.

Because directly predicting the full subgrid-scale joint PDF is computationally too expensive, we require the PDFs to lie within a pre-selected family of PDFs, such as the multivariate Gaussian. Although this family of PDFs is not recommended for large-scale grid boxes (Larson et al. 2001c), it serves as a familiar example. The Gaussian shape defines a family of joint vertical velocity, temperature and moisture PDFs whose positions, widths, and correlations vary. This particular family depends on nine PDF parameters: three for

the positions of the Gaussian along the three dimensions w, θ_l, q_t, three for their respective widths, and three for the covariances between the dimensions. Within this family of PDFs, one needs to select a particular member – identified by its values of the nine PDF parameters – for each grid box and time step.

How can we determine the PDF parameters? To do so, we use the numerical model to predict moments in each grid box and require the PDF's moments to match the predicted moments. For our example of the multivariate Gaussian distribution, a logical choice of moments to predict would be the means $\overline{w}$, $\overline{\theta_l}$, $\overline{q_t}$, the variances $\overline{w'^2}$, $\overline{\theta_l'^2}$, $\overline{q_t'^2}$, and the covariances $\overline{w'\theta_l'}$, $\overline{w'q_t'}$, $\overline{\theta_l'q_t'}$. For this simple example, these moments also happen to be the nine PDF parameters characterizing the PDF family. This is generally not the case, however, and a mapping must then be constructed between the grid box moments and the PDF parameters. Examples of such mappings are described in Larson et al. (2001b,c). To predict the needed moments, the assumed PDF method requires that the model include additional prognostic equations for the desired higher-order moments. Mean quantities are typically predicted by atmospheric models. The number of additional equations depends upon the complexity of the chosen family of PDFs, i.e. the number of PDF parameters required to characterize the family.

The prognostic moments equations needed are the standard higher-order moment equations based on the Navier-Stokes and advection-diffusion equations (e.g. Stull 1988). These equations contain unclosed higher-order and buoyancy terms. In many models, the higher-order terms are closed by assuming that the quantity of interest diffuses down the gradient of that quantity (e.g. Donaldson 1973; Wyngaard et al. 1974; Lumley and Khajeh-Nouri 1974). This assumption is often poor (Moeng and Wyngaard 1989). The quasi-normal assumption (Millionshchikov 1941), which expresses the fourth-order correlations in term of the second-order moments as if the underlying distribution was a multivariate Gaussian,

has also been used in numerous third-order closure models (e.g. André et al. 1976a,b). However, third-order moments are not required to vanish, as would be required for strict consistency with the Gaussian PDF. The assumptions used to close buoyancy terms are typically inconsistent with the closure of the higher-order moments. For example, Bougeault (1981b) used the quasi-normal assumption to close the fourth-order moments and used a positively-skewed PDF to close the buoyancy terms. One of the advantages of the assumed PDF method is that once the joint PDF of w, θ_l, and q_t is known, then any moments or correlations involving these variables can be computed by integration over the PDF. In particular, the unclosed terms that involve only these variables can be computed from the PDF without any additional assumptions. For example, any correlation of the form $\overline{w'^l \theta_l'^m q_t'^n}$ – where l, m, n are positive integers – can be computed as follows:

$$\overline{w'^l \theta_l'^m q_t'^n} = \iiint (w - \overline{w})^l (\theta_l - \overline{\theta_l})^m (q_t - \overline{q_t})^n \, P(w, \theta_l, q_t) \, dw \, d\theta_l \, dq_t. \tag{3.1}$$

Cloud fraction and cloud water can be diagnosed directly by integrating over the saturated portion of the PDF. Buoyancy related moments (involving the virtual potential temperature θ_v') can also be computed directly from the joint PDF. For example, Sommeria and Deardorff (1977) and Mellor (1977) proposed formulas for a Gaussian distribution. Using a double delta PDF, Randall (1987) derived a different expression for the buoyancy flux. The higher-order moment equations also contain pressure terms involving correlations between pressure and scalar perturbations. Because pressure is not included in the PDF, these terms are closed using standard parameterizations (see Section 3.3.1, p. 42).

3.1.2 Advantages

The assumed PDF method has some advantages that in principle may help address several difficulties confronting parameterizations of boundary layer clouds.

- **General foundation.** Well-accepted equations form the foundation of the scheme. The moment equations are derived directly from the Navier-Stokes and advection-diffusion equations, and only then does modeling of the pressure and dissipation terms occur. These equations are closed using a family of PDFs that can be validated against observations. For instance, Larson et al. (2001b,c) have tested numerous families of PDFs against aircraft data and output from large-eddy simulations models for a variety of boundary layer cloudiness regimes. We also present test results in Section 3.2 (p. 33).

- **Consistency.** In some schemes, cloud fraction and cloud water content are predicted separately from each other; in other schemes, different closure methods are used for higher-order moments and buoyancy terms (Bougeault 1981b). When this is the case, there is no guarantee of consistency among the various components forming a parameterization. With the PDF method, in contrast, the prediction of cloud fraction, cloud water, higher-order moments, and buoyancy terms are guaranteed to be internally consistent, since all of them are derived from the same PDF (Lappen and Randall 2001a).

- **Flexibility.** A PDF parameterization is somewhat modular, with the prognostic equations separated to some degree from the choice of the PDF family. Therefore, the family of PDFs can be changed without having to entirely rewrite a parameterization. This makes the assumed PDF method very flexible. Changing the PDF involves rewriting the mapping between the moments and the PDF parameters, and involves modifying the diagnosis of higher-order moments, buoyancy terms, cloud fraction, and liquid water. If the number of PDF parameters changes from one family of PDFs to another, one also has to add or remove prognostic equations.

- **Avoiding biases.** Even when cloud fraction is taken into account, systematic biases remain due to the neglect of subgrid-scale variability (Cahalan et al. 1994; Rotstayn 2000; Pincus and Klein 2000; Larson et al. 2001a). For instance, the autoconversion process by which cloud droplets grow to drizzle-sized drops is frequently represented using the Kessler autoconversion parameterization (Kessler 1969). If one uses this parameterization and neglects subgrid variability within a grid box, one systematically underpredicts autoconversion in the grid box relative to what one would obtain if subgrid variability were taken into account. But the PDF approximates the subgrid information needed to remove such a bias.

- **Avoiding trigger functions.** Some parameterization packages contain separate schemes for separate regimes and use trigger functions to activate the correct scheme. For example, Lock et al. (2000) use a mixed-layer scheme for stratocumulus and a separate mass-flux scheme for cumulus. The algorithm then decides which scheme to activate via a set of rules, the trigger function. It is difficult to formulate a sufficiently general trigger function to use under a wide range of conditions. For instance, the transition from stratocumulus to cumulus depends on many factors, including surface latent heat fluxes, surface shear, and drizzle rate (Lenschow 1998). Furthermore, the use of a trigger function introduces an artificially sharp transition between meteorological regimes. However, if one uses the assumed PDF method and chooses a sufficiently general family of PDFs, then one can avoid the use of trigger functions. A single scheme can then be applied to all regimes and can simulate a smooth transition from one regime to another.

3.1.3 Disadvantages

The disadvantages of the assumed PDF method are mostly related to the computational cost of implementing a PDF-based parameterization. The computational cost falls into three categories.

- **Additional prognostic equations.** The assumed PDF method requires an equal number of prognostic moments as there are free parameters in the chosen family of PDFs. The PDF used for this work needs seven additional moment equations beyond the mean equations already present in the host model (see next section). The added cost is comparable to second-order closure models, but it is considerably less than third-order models. For example, Krueger (1988) implemented a full third-order closure model into a two dimensional cloud resolving model. The turbulence closure added 36 prognostic equations, 11 for the second-order moments, and 24 for the third-order moments. Even after excluding the moment equations involving the horizontal winds (our family of PDFs does not include them), the closure still amounts to an additional 16 prognostic equations, considerably more than the seven required for our PDF-based parameterization.

- **Robustness and timestep.** The addition of prognostic equations for the higher-order moments has an impact on the numerical stability of the scheme and acts to limit the allowable time step. Typically, time steps of a few seconds have been used in higher-order closure models (e.g. Bougeault 1981b). Through the use of a nested time stepping scheme presented in Section 3c, we were able to increase the main time step to approximately 20 seconds. This becomes comparable to typical time increments in mesoscale models, but is still well below increments used in general circulation models.

- **Vertical grid spacing.** Because the model must explicitly resolve boundary layer features such as inversions, a relatively fine vertical grid spacing is needed. This limitation is, however, not particular to the assumed PDF method, but applies to many other closure models as well. Sample results obtained at coarser resolution are shown in Section 4.6 (p. 93).

- **Momentum fluxes.** The joint PDF family does not include perturbations involving horizontal winds u' and v' and the momentum fluxes are currently closed using a traditional downgradient diffusion approach (see Section 3.3.1). Generalizing the PDF to include horizontal winds would add complexity (Lappen 1999; Lappen and Randall 2001a).

3.2 Evaluating families of PDFs

3.2.1 Procedure

The selection of the family of PDFs is a critical component of the assumed PDF method. In broad terms, the chosen family should satisfy two contradictory requirements: flexibility and simplicity. On the one hand, the family of PDFs should be flexible enough so that it can represent with enough accuracy a wide range of expected boundary layer cloudiness regimes, such as cumulus and stratocumulus. On the other hand, the family of PDFs should be as simple as possible to limit the number of free parameters it depends on, therefore limiting its cost. Our experience has also shown that the assumed PDF method is much more robust if the computation of the PDF parameters from the predicted moments can be done analytically.

In a sense, the choice of the family of PDFs then involves striking the right balance between flexibility and simplicity. But how does one go about finding what the right balance

is? If the family of PDFs is not flexible enough, a PDF parameterization will likely fail when simulating all the desired regimes. It might, for example, do well for stratocumulus but fail for cumulus clouds, or vice-versa. If the family of PDFs is not simple enough, the parameterization becomes too expensive and of little practical use.

Fortunately, data can help us answer the question about finding the right balance. Families of PDFs can be tested diagnostically against observational or numerical data. Larson et al. (2001c) evaluated various PDFs using aircraft data from the FIRE and Atlantic Stratocumulus Experiment (ASTEX) experiments. They also supplemented their analysis with numerical data derived from LESs.

The diagnostic testing procedure is as follows. One first computes the means and higher-order moments from the data that are needed to determine the PDF free parameters. Those moments are typically the mean vertical velocity, temperature, and moisture content as well as select second- and third-order moments. These moments are then used to determine the PDF parameters for a specific family of PDFs. Once the PDF is fixed, it can be integrated to yield secondary quantities, such as cloud properties, that can then be compared directly with their counterparts in the original data.

The cloud properties we choose to compare are the cloud fraction, liquid water, and liquid water flux. Cloud fraction and liquid water are of primary importance since we desire a family of PDFs that is capable of representing boundary layer regimes that have very different cloud amounts. The liquid water flux is also a very important cloud property. It is a major contribution to the buoyancy flux in the cloud layer, and therefore by extension to the dynamics of the boundary layer. Very different expressions for the liquid water and buoyancy fluxes in partly cloudy layers have been derived depending on the assumed shape of the underlying joint PDF. For instance, Mellor (1977) and Sommeria and Deardorff (1977) derived a formula using a Gaussian PDF. Randall (1987) obtained a very different

expression by assuming a double delta PDF. It is therefore important to also test the ability of a family of PDFs to produce fluxes of liquid water that are realistic.

3.2.2 Families to be tested

We will evaluate the performance of five different families of PDFs: double delta, single Gaussian, and three double Gaussian families.

1. Double delta function. This PDF family depends on 7 parameters that are determined from the following moments: $\bar{w}$, $\bar{\theta}_l$, $\bar{q}_t$, $\overline{w'^2}$, $\overline{w'^3}$, $\overline{w'\theta'_l}$, $\overline{w'q'_t}$. This PDF consists of two Dirac delta functions whose locations and relative amplitude vary. A double delta PDF corresponds to a mass-flux scheme consisting of an updraft and downdraft plume, with no subplume variability. Following Randall et al. (1992) and Lappen and Randall (2001a), the relative amplitude of the delta functions and their positions in the w coordinate is chosen such that the resulting PDF matches the observed values of the moments $\bar{w}$, $\overline{w'^2}$, and $\overline{w'^3}$. The positions of the delta functions in the θ_l coordinate are determined by $\bar{\theta}_l$ and $\overline{w'\theta'_l}$. Likewise, the positions in the q_t coordinate are determined by $\bar{q}_t$ and $\overline{w'q'_t}$.

2. Single Gaussian. This PDF depends on 9 free parameters that are determined from $\bar{w}$, $\bar{\theta}_l$, $\bar{q}_t$, $\overline{w'^2}$, $\overline{\theta'^2_l}$, $\overline{q'^2_t}$, $\overline{w'\theta'_l}$, $\overline{w'q'_t}$, and $\overline{q'_t\theta'_l}$. It consists of a single Gaussian that in general has non-zero correlations between the variables. Unlike the double delta PDF, the single Gaussian PDF does not allow the possibility of skewness or bimodality, but it does exactly satisfy all the second-order moments.

3. Double Gaussian (LY). This is a double Gaussian family proposed by Lewellen and Yoh (1993). This PDF consist of the sum of two Gaussians whose positions and relative amplitudes may vary, permitting skewed and bimodal shapes. The number

of degrees of freedom is reduced from a full double Gaussian so that the PDF depends on 12 parameters that can be determined from $\bar{w}$, $\bar{\theta}_l$, $\bar{q}_t$, $\overline{w'^2}$, $\overline{w'^3}$, $\overline{\theta_l'^2}$, $\overline{\theta_l'^3}$, $\overline{q_t'^2}$, $\overline{q_t'^3}$, $\overline{w'\theta_l'}$, $\overline{w'q_t'}$, and $\overline{q_t'\theta_l'}$. The LY scheme contains two complications. First, its PDF parameters cannot be solved analytically. Second, a host model may predict moments that result in unphysical values of the PDF parameters (Larson et al. 2001c). It also requires prediction of all third-order moments which adds cost and complexity.

4. Double Gaussian (LGC). This family of PDFs was proposed by Larson et al. (2001c). This scheme depends on 10 PDF parameters that can be determined from $\bar{w}$, $\bar{\theta}_l$, $\bar{q}_t$, $\overline{w'^2}$, $\overline{w'^3}$, $\overline{\theta_l'^2}$, $\overline{q_t'^2}$, $\overline{w'\theta_l'}$, $\overline{w'q_t'}$, and $\overline{q_t'\theta_l'}$. The width of the individual Gaussian in w are assumed to be equal and the PDF parameters can be found analytically. The only third-order moment needed id $\overline{w'^3}$.

5. Double Gaussian (LHH). This is another family of double Gaussian PDFs proposed by Luhar et al. (1996) and extended by Larson et al. (2001c) to three dimensions. Like the LGC family, it also depends on 10 free parameters that are determined from $\bar{w}$, $\bar{\theta}_l$, $\bar{q}_t$, $\overline{w'^2}$, $\overline{w'^3}$, $\overline{\theta_l'^2}$, $\overline{q_t'^2}$, $\overline{w'\theta_l'}$, $\overline{w'q_t'}$, and $\overline{q_t'\theta_l'}$. Unlike the LGC scheme, the two Gaussians along the w coordinate are not required to be of equal width. The PDF parameters can also be found analytically.

Among these five schemes, the double delta is the least expensive one since it depends only on 7 parameters. It is followed by the single Gaussian PDF. The double Gaussian families are all slightly more expensive. The LGC and LHH scheme need 10 parameters and the LY 12. Detailed procedures to fit these various families of PDFs to data is given by Larson et al. (2001c) and is also reproduced in Appendix A for completeness.

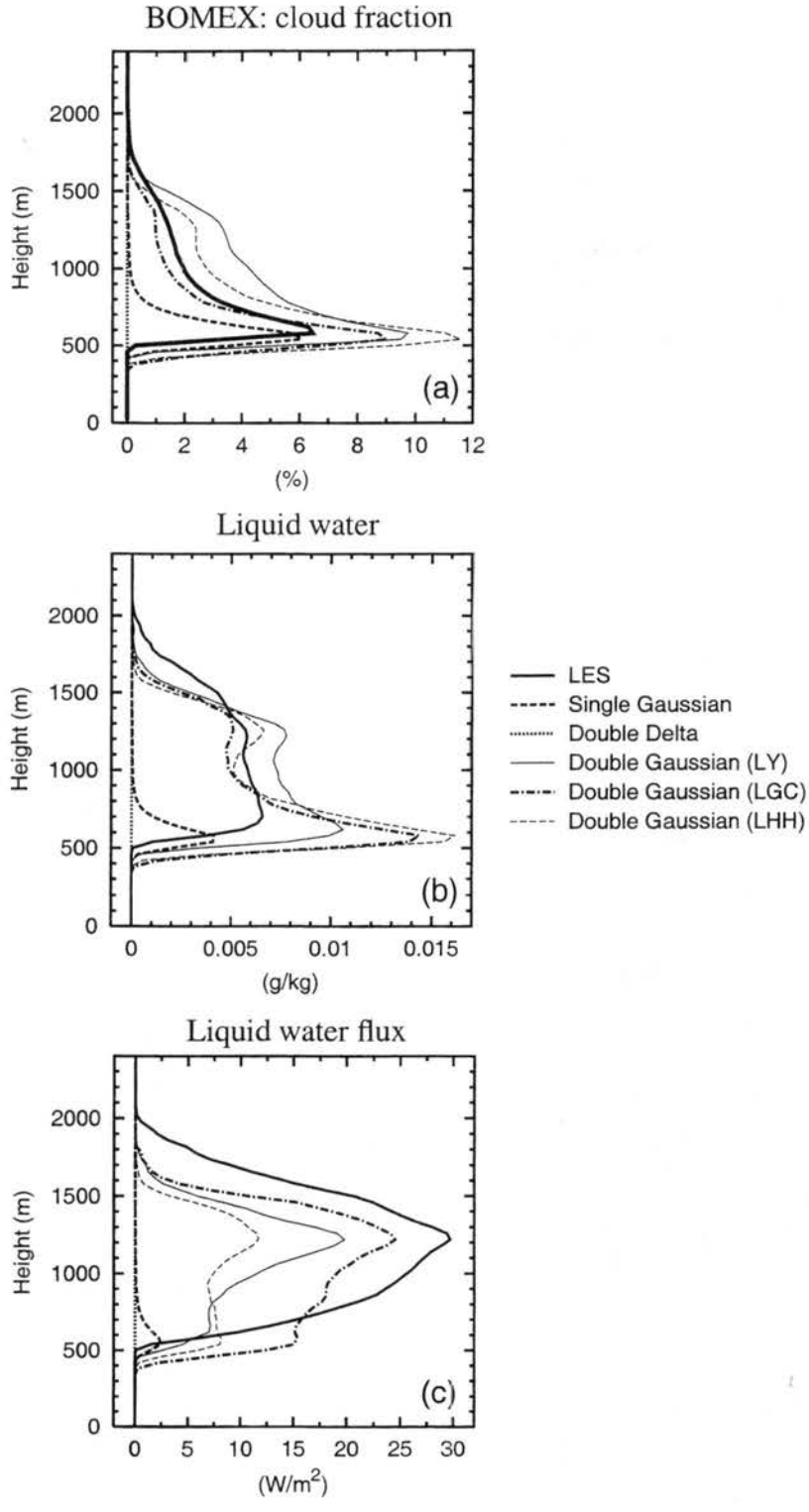

Figure 3.1: Plots of cloud fraction (a), liquid water (b), and liquid water flux (c) averaged over the last three hours of the BOMEX simulation. Both original LES fields and results obtained by fitting various families of PDFs to the LES moments are shown.

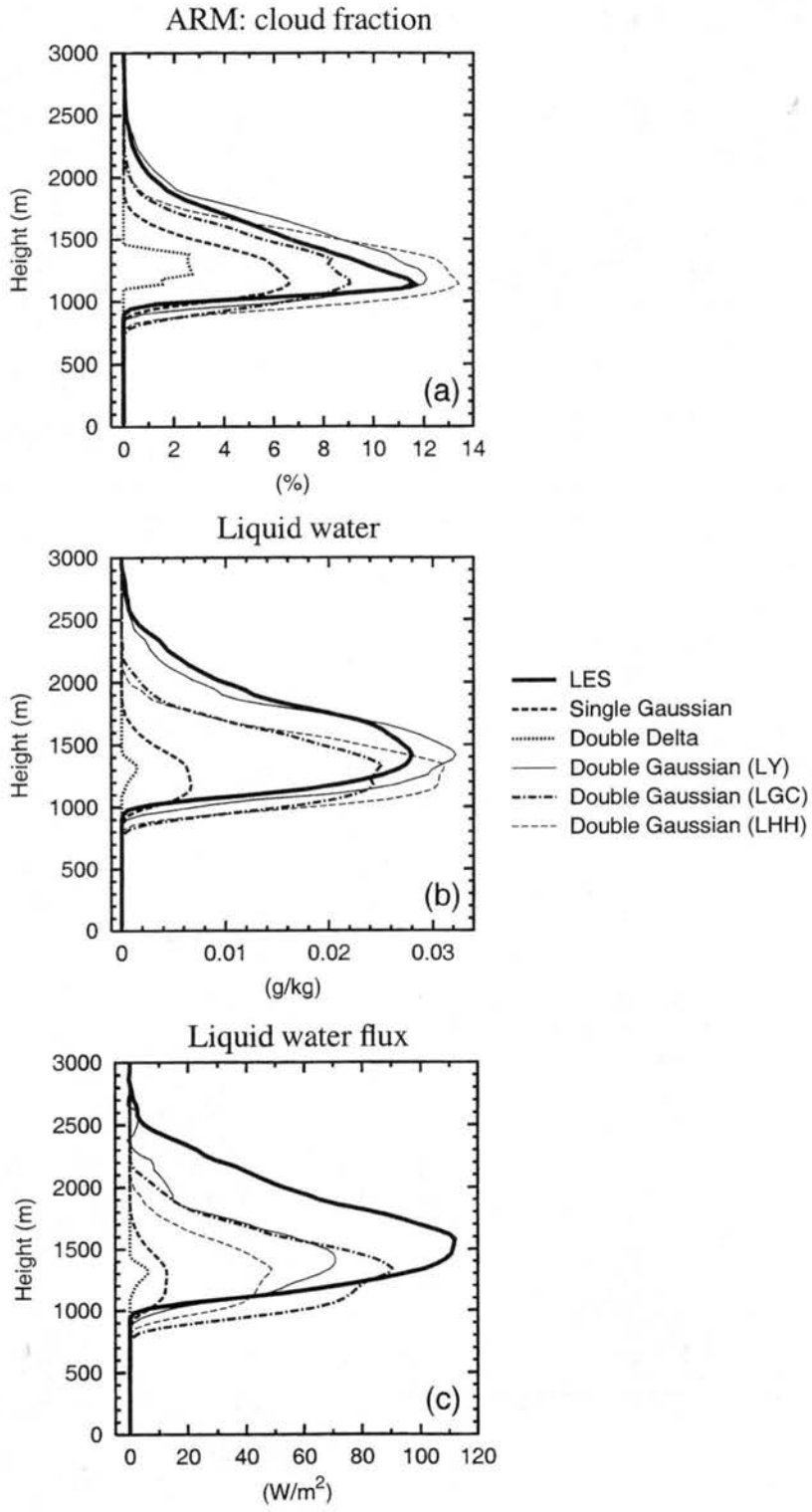

Figure 3.2: Same as Fig. 3.1 but for the ARM simulation between 1900 and 2000 UTC.

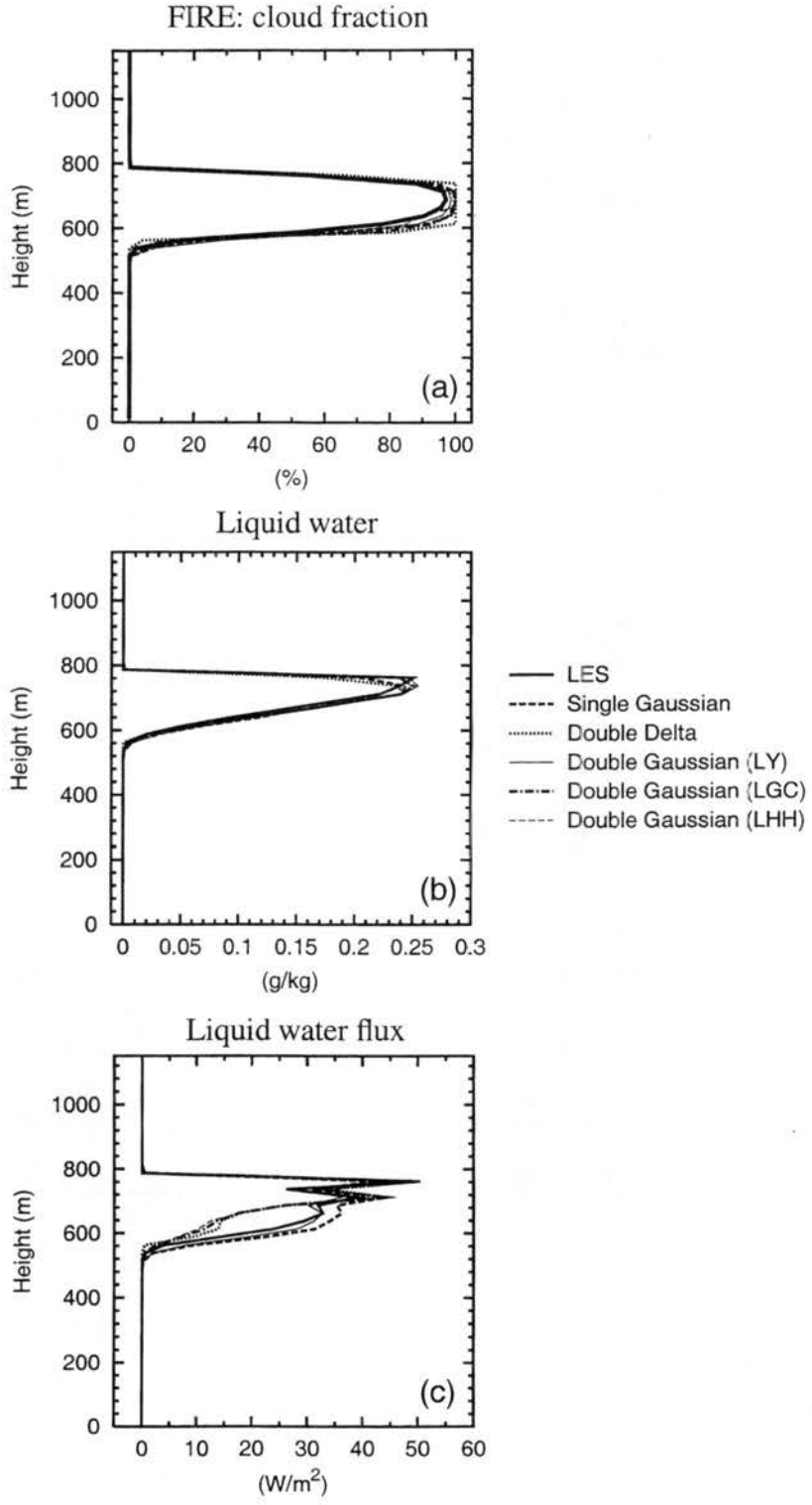

Figure 3.3: Same as Fig. 3.2 but for the last hour of the FIRE simulation.

3.2.3 Test results

We present results from PDF fits to LES data for three of our LESs. Two cumulus cases (BOMEX and ARM) and one stratocumulus case (FIRE). The results of fitting the five families of PDFs to the LES BOMEX data are shown in Fig. 3.1. The top panel (a) shows the cloud fraction. The LES produces a cloud fraction that maximizes near cloud base and decreases with height. For this case, the double delta PDF does not produce any cloud, as the two diagnosed delta functions lie in unsaturated air. The single Gaussian produces a profile that is reasonable in the lowest 300 m of the cloud, but does not produce any cloud above 900 m, probably due to the fact that the single Gaussian PDF is unable to represent skewed distributions. The three families of double Gaussian PDFs produce much better cloud fractions. They all tend to overestimate cloud cover in the lowest part of the cloud, and the LY and LHH also overestimate it higher up. The altitude of cloud base is underpredicted by all three double Gaussian families, although the LY scheme does a slightly better job.

Similar characteristics can be observed for the profiles of liquid water (Fig. 3.1b). The double delta does not produce any condensate. The single Gaussian has only a small amount of condensate over a very shallow layer. The three double Gaussians are again in much better agreements with the LES, except that they tend to overestimate the condensate amount in the lowest part of the cloud.

The liquid water flux (Fig. 3.1c) is underpredicted by all families of PDFs. The best result is given by the LGC double Gaussian, followed by the LY scheme. Interestingly, the LHH scheme, which produces a liquid water profile very similar to the LGC scheme, has a liquid water flux that is only half as large.

Results for the continental cumulus cloud case are depicted in Fig. 3.2. They exhibit similar trends than the BOMEX case. The double delta PDF now produces a small amount

of cloud. The single Gaussian family has a slightly more realistic cloud fraction, but underestimates both cloud water and liquid water flux by a significant margin. The double Gaussian families generally produce profiles in much better agreement with the LES. The LY scheme has the most realistic cloud fraction and liquid water, followed by the LHH scheme and the LGC double Gaussian. The situation is reversed for the liquid water flux. The best results are from the LGC PDF, followed by the LY and LHH families. The LHH family has a liquid water flux that is about half as large as the the LGC family. As for BOMEX, the LGC and LHH double Gaussian schemes underestimate the altitude of cloud base and top, but by a larger amount for cloud top. The LY family produces a more realistic cloud top, except for the liquid water flux.

Finally, results for the solid stratocumulus cloud are shown in Fig. 3.3. Compared to the cumulus cases, the differences between the five different families of PDFs are small. All schemes appear to produces realistic profiles of cloud fraction, liquid water, and liquid water flux. The biggest differences are observed for the liquid water flux, with the single Gaussian and the LY double Gaussian predicting larger values in the lowest part of the cloud.

In summary, it appears that although the single Gaussian and double delta PDFs perform adequately for the stratocumulus case, they do not perform satisfactorily for the two cumulus cases. The three families of double Gaussian PDFs are much better candidates in the sense that they produce reasonable fits for all three cases.

Choosing a winner among the double Gaussian families is a more subtle task. The LY scheme appears to have a slight edge, which is not unexpected since it is the most expensive of all schemes (12 free parameters). It however performs worse than the LGC scheme for the liquid water flux in cumulus layers, which is of concern if one is to use the PDF family for a parameterization. Another concern with the LY scheme is that it requires prediction

of the third-order moments $\overline{\theta_l'^3}$ and $\overline{q_t'^3}$ which adds cost. Also, its PDF parameters cannot be obtained analytically from the moments, rendering its use in a parameterization more difficult. Among the two other double Gaussian schemes, which have identical cost, the LGC scheme appears to be a better choice as it produces more realistic liquid water fluxes.

As mentioned earlier, choosing a family of PDFs requires making a delicate compromise between cost and flexibility. We believe that the added benefits of using the more flexible LY scheme do not warrant the added cost and complexity. We therefore retain the LGC double Gaussian scheme as our family of PDFs for the parameterization.

3.3 Application to a single-column model

3.3.1 Basic equations

We now describe the construction of the new boundary layer parameterization. The family of PDFs retained is the LGC double Gaussian introduced in the previous section. It is a double Gaussian with correlation between θ_l and q_t within each individual Gaussian:

$$G(w, \theta_l, q_t) = aG_1(w, \theta_l, q_t) + (1-a)G_2(w, \theta_l, q_t) \tag{3.2a}$$

with $G_i(w, \theta_l, q_t)$

$$\begin{aligned} &= \frac{1}{(2\pi)^{3/2}\,\sigma_{wi}\,\sigma_{q_{ti}}\,\sigma_{\theta_{li}}\,(1-r_{q_t\theta_l}^2)^{1/2}} \\ &\times \exp\left\{-\tfrac{1}{2}\left(\tfrac{w-(w_i-\tilde{w})}{\sigma_{wi}}\right)^2\right\} \\ &\times \exp\left\{-\tfrac{1}{2(1-r_{q_t\theta_l}^2)}\left[\left(\tfrac{q_t-(q_{ti}-\bar{q}_t)}{\sigma_{q_{ti}}}\right)^2+\left(\tfrac{\theta_l-(\theta_{li}-\bar{\theta}_l)}{\sigma_{\theta_{li}}}\right)^2-2r_{q_t\theta_l}\left(\tfrac{q_t-(q_{ti}-\bar{q}_t)}{\sigma_{q_{ti}}}\right)\left(\tfrac{\theta_l-(\theta_{li}-\bar{\theta}_l)}{\sigma_{\theta_{li}}}\right)\right]\right\}. \end{aligned} \tag{3.2b}$$

This family of PDFs depends on a number of free parameters:

- a: relative weight of the first Gaussian.
- $\psi 1$, $\psi 2$, $\sigma_{\psi 1}$, $\sigma_{\psi 2}$: locations and widths of the vertical velocity (w), liquid water potential temperature (θ_l), and total specific water content (q_t) Gaussians.

- $r_{q_t\theta_l}$: intra-Gaussian correlation between liquid water potential temperature and total specific water content.

Some examples of double Gaussian PDFs projected on the vertical velocity axis are depicted in Fig. 3.4. They demonstrate some of the flexibility of the family of PDFs. It can represent symmetric distributions (Figs 3.4a and 3.4b) that could, for instance, occur in stratocumulus layers, but it can also represent skewed distributions. Figure 3.4f, with its long tail extending on the positive side of the vertical velocity axis, is typical of what might be encountered in a cumulus layer.

The PDF parameters used to characterize a particular member from the family of PDFs are obtained analytically from ten moments. They are the mean vertical velocity $\bar{w}$, liquid water potential temperature $\bar{\theta}_l$, and total water specific humidity $\bar{q}_t$; the second-order moments $\overline{w'\theta_l'}$, $\overline{w'q_t'}$, $\overline{q_t'\theta_l'}$, $\overline{w'^2}$, $\overline{\theta_l'^2}$, $\overline{q_t'^2}$; and the third-order of the vertical velocity $\overline{w'^3}$. Details of the procedure are given in Larson et al. (2001c) and Appendix A. We only briefly outline the methodology here. The vertical velocity moments $\bar{w}$, $\overline{w'^2}$ and $\overline{w'^3}$ are used to compute the PDF parameters a, w_1, w_2, σ_{w1} and σ_{w2}. The width of each Gaussian along the w coordinate are defined as $\sigma_{w1} = \tilde{\sigma}_w\sqrt{\overline{w'^2}}$ and $\sigma_{w2} = \tilde{\sigma}_w\sqrt{\overline{w'^2}}$. We choose $\tilde{\sigma}_w = 0.4$. The relative weight of each Gaussian a, as well as their locations w_1 and w_2 are obtained by integrating the PDF to obtain expressions for $\bar{w}$, $\overline{w'^2}$ and $\overline{w'^3}$. We define the skewness $Sk_w \equiv \overline{w'^3}/(\overline{w'^2}^{3/2})$ and find:

$$a = \frac{1}{2}\left\{1 - Sk_w\left[\frac{1}{4(1-\tilde{\sigma}_w^2)^3 + Sk_w^2}\right]^{1/2}\right\}, \tag{3.3}$$

$$\tilde{w}_1 \equiv \frac{w_1 - \overline{w}}{\sqrt{\overline{w'^2}}} = \left(\frac{1-a}{a}\right)^{1/2}(1-\tilde{\sigma}_w^2)^{1/2}, \tag{3.4}$$

$$\tilde{w}_2 \equiv \frac{w_2 - \overline{w}}{\sqrt{\overline{w'^2}}} = -\left(\frac{a}{1-a}\right)^{1/2}(1-\tilde{\sigma}_w^2)^{1/2}. \tag{3.5}$$

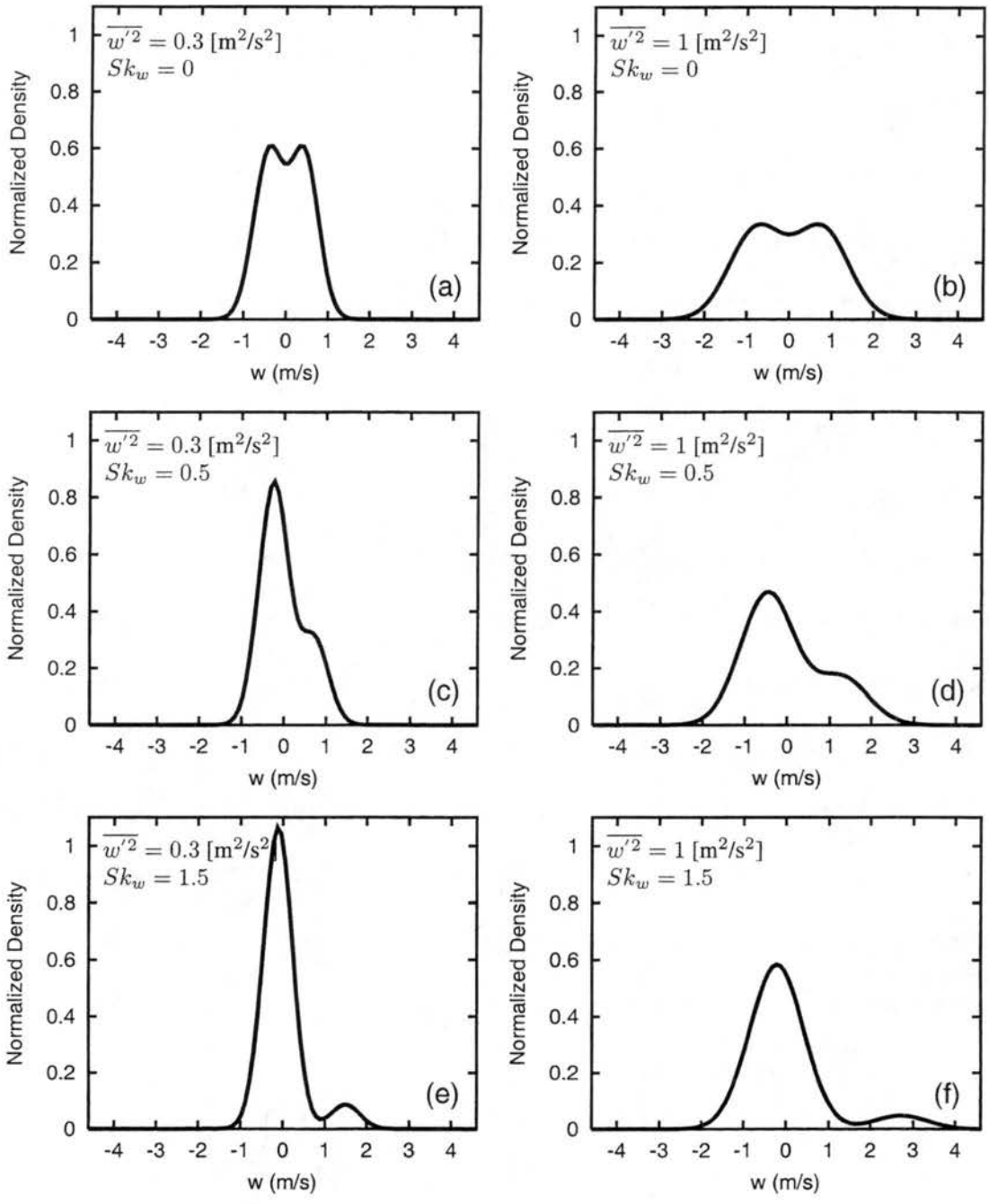

Figure 3.4: Examples of double Gaussian PDFs projected on the vertical velocity axis with differing variances and skewnesses. Two variance values ($\overline{w'^2} = 0.3, 1$ [m^2/s^2]) and three skewness values ($Sk_w = \overline{w'^3}/\overline{w'^2}^{1.5} = 0, 0.5, 1.5$) are shown.

The parameters θ_{l1} and θ_{l2} are obtained from the equations for $\bar{\theta}_l$ and $\overline{w'\theta'_l}$:

$$\tilde{\theta}_{l1} \equiv \frac{\theta_{l1} - \overline{\theta_l}}{\sqrt{\overline{\theta'^2_l}}} = -\frac{\overline{w'\theta'_l} \Big/ \left(\sqrt{\overline{w'^2}}\sqrt{\overline{\theta'^2_l}}\right)}{\tilde{w}_2} \tag{3.6}$$

$$\tilde{\theta}_{l2} \equiv \frac{\theta_{l2} - \overline{\theta_l}}{\sqrt{\overline{\theta'^2_l}}} = -\frac{\overline{w'\theta'_l} \Big/ \left(\sqrt{\overline{w'^2}}\sqrt{\overline{\theta'^2_l}}\right)}{\tilde{w}_1}. \tag{3.7}$$

Unlike the widths of the Gaussians along the w axis, the widths along the θ_l axis, $\sigma_{\theta_l 1}$ and $\sigma_{\theta_l 2}$, are allowed to differ. Their are computed from the equations for $\overline{\theta'^2_l}$ and $\overline{\theta'^3_l}$. Since $\overline{\theta'^3_l}$ is not a prognostic variable, an additional assumption regarding the skewness of θ_l is needed. We simply assume that it is zero. The procedure to obtain the parameters q_{t1}, q_{t2}, $\sigma_{q_t 1}$ and $\sigma_{q_t 2}$ is similar. The skewness of q_t is assumed to be proportional to Sk_w with a proportionality coefficient of 1.2. We realize that the skewness assumptions made here are not very realistic. In the previous sections, we also tested the more costly family of Lewellen and Yoh (1993) which does not make such assumptions. However, we believe that the potential gains do not justify the additional cost and complexity of using the Lewellen and Yoh family. Finally, the subplume correlation $r_{q_t\theta_l}$ is obtained from the $\overline{q'_t\theta'_l}$ equation. Note also that special cases arise when any of the predicted moment is vanishingly small. The procedure in these cases is detailed in Larson et al. (2001c) and Appendix A.

We now introduce the prognostic equations governing the time evolution of the ten moments required by the parameterization. Since the parameterization is implemented in a single-column framework, the mean vertical velocity is imposed by the large-scale forcing and does not need to be explicitly prognosed. Additionally, the mean horizontal winds $\bar{u}$ and $\bar{v}$ are also predicted in the single-column model. The filtering approach, in which the model resolved fields are taken as a running spatial average of finite width, is followed to derive the predictive equations (Germano 1992). As a notational shorthand, we will write

$\overline{a'b'}$, but this is meant to be interpreted as $\overline{ab} - \bar{a}\,\bar{b}$, and similarly for other moments. The probability distribution associated with the filtering approach is the probability of finding w, θ_l, and q_t within a *spatially filtered* region. The PDFs referred to in this paper are therefore strictly speaking "filtered density functions" as discussed in Colucci et al. (1998).

The filtered equations describing the time evolution of the grid box mean values are

$$\frac{\partial \bar{u}}{\partial t} = -\bar{w}\frac{\partial \bar{u}}{\partial z} - f(v_g - \bar{v}) - \frac{\partial}{\partial z}\overline{u'w'} \tag{3.8}$$

$$\frac{\partial \bar{v}}{\partial t} = -\bar{w}\frac{\partial \bar{v}}{\partial z} + f(u_g - \bar{u}) - \frac{\partial}{\partial z}\overline{v'w'} \tag{3.9}$$

$$\frac{\partial \bar{q}_t}{\partial t} = -\bar{w}\frac{\partial \bar{q}_t}{\partial z} - \frac{\partial}{\partial z}\overline{w'q_t'} + \left.\frac{\partial \bar{q}_t}{\partial t}\right|_{\text{ls}} \tag{3.10}$$

$$\frac{\partial \bar{\theta}_l}{\partial t} = -\bar{w}\frac{\partial \bar{\theta}_l}{\partial z} - \frac{\partial}{\partial z}\overline{w'\theta_l'} - \bar{R} + \left.\frac{\partial \bar{\theta}_l}{\partial t}\right|_{\text{ls}}, \tag{3.11}$$

where $\bar{R}$ is the radiative heating rate, f the Coriolis parameter and u_g, v_g the geostrophic winds. $\left.\frac{\partial \bar{q}_t}{\partial t}\right|_{\text{ls}}$ and $\left.\frac{\partial \bar{\theta}_l}{\partial t}\right|_{\text{ls}}$ are large-scale moisture and temperature forcings.

The time evolution of the second-order turbulent moments is given by equations similar to André et al. (1978), with the following differences: (i) the mean advection terms have been retained for all moments, (ii) the conservative liquid water potential temperature (θ_l) is used as prognostic temperature variable with the buoyancy related moments written in terms of virtual potential temperature (Bougeault 1981b):

$$\frac{\partial \overline{w'^2}}{\partial t} = -\bar{w}\frac{\partial \overline{w'^2}}{\partial z} - \frac{\partial \overline{w'^3}}{\partial z} - 2\overline{w'^2}\frac{\partial \bar{w}}{\partial z} + \frac{2g}{\theta_0}\overline{w'\theta_v'} - \frac{2}{\rho_0}\overline{w'\frac{\partial p'}{\partial z}} - \frac{2}{3}\epsilon \tag{3.12}$$

$$\frac{\partial \overline{q_t'^2}}{\partial t} = -\bar{w}\frac{\partial \overline{q_t'^2}}{\partial z} - \frac{\partial \overline{w'q_t'^2}}{\partial z} - 2\overline{w'q_t'}\frac{\partial \bar{q}_t}{\partial z} - \epsilon_{q_t q_t} \tag{3.13}$$

$$\frac{\partial \overline{\theta_l'^2}}{\partial t} = -\bar{w}\frac{\partial \overline{\theta_l'^2}}{\partial z} - \frac{\partial \overline{w'\theta_l'^2}}{\partial z} - 2\overline{w'\theta_l'}\frac{\partial \bar{\theta}_l}{\partial z} - \epsilon_{\theta_l\theta_l} \tag{3.14}$$

$$\frac{\partial \overline{q_t'\theta_l'}}{\partial t} = -\bar{w}\frac{\partial \overline{q_t'\theta_l'}}{\partial z} - \frac{\partial \overline{w'q_t'\theta_l'}}{\partial z} - \overline{w'q_t'}\frac{\partial \bar{\theta}_l}{\partial z} - \overline{w'\theta_l'}\frac{\partial \bar{q}_t}{\partial z} - \epsilon_{q_t\theta_l} \tag{3.15}$$

$$\frac{\partial \overline{w'q_t'}}{\partial t} = -\bar{w}\frac{\partial \overline{w'q_t'}}{\partial z} - \frac{\partial \overline{w'^2 q_t'}}{\partial z} - \overline{w'^2}\frac{\partial \bar{q}_t}{\partial z} - \overline{w'q_t'}\frac{\partial \bar{w}}{\partial z} + \frac{g}{\theta_0}\overline{q_t'\theta_v'} - \frac{1}{\rho_0}\overline{q_t'\frac{\partial p'}{\partial z}} - \epsilon_{wq_t} \tag{3.16}$$

$$\frac{\partial \overline{w'\theta_l'}}{\partial t} = -\bar{w}\frac{\partial \overline{w'\theta_l'}}{\partial z} - \frac{\partial \overline{w'^2\theta_l'}}{\partial z} - \overline{w'^2}\frac{\partial \bar{\theta}_l}{\partial z} - \overline{w'\theta_l'}\frac{\partial \bar{w}}{\partial z} + \frac{g}{\theta_0}\overline{\theta_l'\theta_v'} - \frac{1}{\rho_0}\overline{\theta_l'\frac{\partial p'}{\partial z}} - \epsilon_{w\theta_l}\,, \tag{3.17}$$

with g the gravity, ρ_0 and θ_0 the reference density and potential temperature, and $\epsilon_{\psi\psi}$ the dissipation terms.

The prognostic equation for the third-order moment of the vertical velocity ($\overline{w'^3}$) differs slightly from the one in André et al. (1978) because the quasi-Gaussian approximation has not been used and therefore the fourth-order moment of the vertical velocity ($\overline{w'^4}$) is left unclosed:

$$\frac{\partial \overline{w'^3}}{\partial t} = -\bar{w}\frac{\partial \overline{w'^3}}{\partial z} - \frac{\partial \overline{w'^4}}{\partial z} + 3\overline{w'^2}\frac{\partial \overline{w'^2}}{\partial z} - 2\overline{w'^3}\frac{\partial \bar{w}}{\partial z} + \frac{3g}{\theta_0}\overline{w'^2\theta_v'} - \frac{3}{\rho_0}\overline{w'^2\frac{\partial p'}{\partial z}} - \epsilon_{www}\,. \tag{3.18}$$

Equations (3.12), (3.16) and (3.17) contain pressure correlation terms that must be parameterized. André et al. (1978) used a formulation based on Rotta (1951) and Launder (1975):

$$\begin{aligned} -\frac{2}{\rho_0}\overline{w'\frac{\partial p'}{\partial z}} = &-\frac{C_4}{\tau}\left(\overline{w'^2} - \frac{2}{3}\bar{e}\right) - C_5\left(-2\overline{w'^2}\frac{\partial \bar{w}}{\partial z} + \frac{2g}{\theta_0}\overline{w'\theta_v'}\right) \\ &+ \frac{2}{3}C_5\left(\frac{g}{\theta_0}\overline{w'\theta_v'} - \overline{u'w'}\frac{\partial \bar{u}}{\partial z} - \overline{v'w'}\frac{\partial \bar{v}}{\partial z}\right) \end{aligned} \tag{3.19}$$

$$-\frac{1}{\rho_0}\overline{q_t'\frac{\partial p'}{\partial z}} = -\frac{C_6}{\tau}\overline{w'q_w'} - C_7\left(-\overline{w'q_w'}\frac{\partial \bar{w}}{\partial z} + \frac{g}{\theta_0}\overline{q_w'\theta_v'}\right) \tag{3.20}$$

$$-\frac{1}{\rho_0}\overline{\theta_l'\frac{\partial p'}{\partial z}} = -\frac{C_6}{\tau}\overline{w'\theta_l'} - C_7\left(-\overline{w'\theta_l'}\frac{\partial \bar{w}}{\partial z} + \frac{g}{\theta_0}\overline{\theta_l'\theta_v'}\right)\,. \tag{3.21}$$

where τ is a dissipation time scale described below. The damping constants C_i are also given later in the text.

Because the model does not predict any higher-order moments of the horizontal winds, we assume that the turbulent kinetic energy, $\bar{e}$, is proportional to the vertical velocity variance $\overline{w'^2}$:

$$\bar{e} = \frac{3}{2}\overline{w'^2}. \tag{3.22}$$

With a proportionality coefficient of 3/2, the first term on the right hand side of (3.19) effectively drops out. However, we tried various values for the proportionality constant, ranging from 1 to 2, and the model showed almost no sensitivity.

For the pressure correlation term in eq. (3.18), Bougeault (1981b) suggested the addition of a "rapid" term to the formulations used by André et al. (1978):

$$-\frac{3}{\rho_0}\overline{w'^2\frac{\partial p'}{\partial z}} = -\frac{C_8}{\tau_{www}}\overline{w'^3} - C_{11}\left(-2\overline{w'^3}\frac{\partial \bar{w}}{\partial z} + \frac{3g}{\theta_0}\overline{w'^2\theta_v'}\right). \tag{3.23}$$

The dissipation parameterizations for the second-order moments are expressed as:

$$\epsilon = \frac{C_1}{\tau}\overline{w'^2} - \nu_1\nabla_z^2\overline{w'^2} \tag{3.24a}$$

$$\epsilon_{q_tq_t} = \frac{C_2}{\tau}\overline{q_t'^2} - \nu_2\nabla_z^2\overline{q_t'^2};\quad \epsilon_{\theta_l\theta_l} = \frac{C_2}{\tau}\overline{\theta_l'^2} - \nu_2\nabla_z^2\overline{\theta_l'^2};\quad \epsilon_{q_t\theta_l} = \frac{C_2}{\tau}\overline{q_t'\theta_l'} - \nu_2\nabla_z^2\overline{q_t'\theta_l'} \tag{3.24b}$$

$$\epsilon_{wq_t} = -\nu_6\nabla_z^2\overline{w'q_t'};\quad \epsilon_{w\theta_l} = -\nu_6\nabla_z^2\overline{w'\theta_l'}; \tag{3.24c}$$

where ∇_z^2 denotes the second-order vertical derivative. The dissipation parameterizations, with the exception of the turbulent fluxes, are composed of two terms: a Newtonian damping term inversely proportional to a characteristic dissipation time scale τ, and a background diffusion term. The diffusion term was found to be a needed complement since the Newtonian damping term can not damp small-scale noise. Its magnitude is typically much smaller than all the other terms in the prognostic equation. The dissipation for the fluxes

only incorporate a background diffusion term; a damping term is part of the parameterization of the pressure correlation. The time scale τ is taken as the ratio of an eddy length scale, L, and a characteristic velocity scale, $\sqrt{\overline{w'^2}}$:

$$\tau = \begin{cases} \dfrac{L}{\sqrt{\overline{w'^2}}}; & L/\sqrt{\overline{w'^2}} \leqslant \tau_{\max} \\ \tau_{\max}; & L/\sqrt{\overline{w'^2}} > \tau_{\max} \,. \end{cases} \tag{3.25}$$

A maximum dissipation time $\tau_{\max}$ of 900 s is imposed in order to prevent the damping terms from becoming too small in regions with little turbulent activity.

When the PDF parameter a defining the relative weight of each Gaussian is very close to either 0 or 1, instabilities can develop due to large values of the higher-order moments $\overline{w'^2\theta_v'}$ and $\overline{w'^4}$ diagnosed by the closure. It was found that this problem can be overcome by decreasing the dissipation time scale τ_{www} appearing in Eq. (3.23) relative to the general time scale τ when a is close to 0 and 1:

$$\tau_{www} = \begin{cases} \tau \left[1 + 3\left(1 - \frac{a-0.01}{0.04}\right)\right]^{-1}; & 0.01 \leqslant a < 0.05 \\ \tau; & 0.05 \leqslant a \leqslant 0.95 \\ \tau \left[1 + 3\left(1 - \frac{0.99-a}{0.04}\right)\right]^{-1}; & 0.95 < a \leqslant 0.99 \,. \end{cases} \tag{3.26}$$

This modification effectively decreases the dissipation time scale in the predictive equation for $\overline{w'^3}$ by up to a factor four when a is close to either 0 or 1. The PDF closure enforces that a must lie in the range 0.01 to 0.99 (Larson et al. 2001c).

Finally, the dissipation parameterization for the third-order moment of the vertical velocity $\overline{w'^3}$ is of the form:

$$\epsilon_{www} = -\left(K_w + \nu_8\right) \nabla_z^2 \overline{w'^3} \,. \tag{3.27}$$

A larger diffusion coefficient was found necessary to maintain stability of the model. The eddy diffusivity coefficient K_w is

$$K_w = 0.27\, L \left(\overline{w'^2}\right)^{1/2} . \tag{3.28}$$

The constant appearing in Eq. (3.28) is comparable to the one used by Moeng and Randall (1984) to damp oscillations appearing near the boundary layer inversion.

The traditional closure problem is regarded as closing the higher-order terms appearing in the predictive moment equations. For the set of equations (3.12)-(3.18), they are: $\overline{w'q_t'^2}$, $\overline{w'\theta_l'^2}$, $\overline{w'q_t'\theta_l'}$, $\overline{w'^2q_t'}$, $\overline{w'^2\theta_l'}$, and $\overline{w'^4}$. Additionally, buoyancy terms ($\overline{w'\theta_v'}$, $\overline{q_t'\theta_v'}$, $\overline{\theta_l'\theta_v'}$, $\overline{w'^2\theta_v'}$) must also be related to prognostic quantities. This has frequently been regarded as distinct from the closure problem. However, the assumed PDF method allows us to close all these terms in a consistent manner directly from the PDF.

The higher-order moments that need to be closed are computed by integration over the PDF as in Eq. (3.1). For the analytical double Gaussian PDF family, we obtain after integration

$$\overline{w'\theta_l'^2} = a(w_1 - \bar{w})\left((\theta_{l1} - \bar{\theta}_l)^2 + \sigma_{\theta_{l1}}^2\right) + (1-a)(w_2 - \bar{w})\left((\theta_{l2} - \bar{\theta}_l)^2 + \sigma_{\theta_{l2}}^2\right) \quad (3.29)$$

$$\overline{w'^2\theta_l'} = a\left((w_1 - \bar{w})^2 + \sigma_{w1}^2\right)(\theta_{l1} - \bar{\theta}_l) + (1-a)\left((w_2 - \bar{w})^2 + \sigma_{w2}^2\right)(\theta_{l2} - \bar{\theta}_l) \quad (3.30)$$

$$\begin{aligned}\overline{w'q_t'\theta_l'} = {} & a(w_1 - \bar{w})[(\bar{q}_{t1} - \bar{q}_t)(\theta_{l1} - \bar{\theta}_l) + r_{q_t\theta_l}\sigma_{\theta_{l1}}\sigma_{q_{t1}}] \\ & + (1-a)(w_2 - \bar{w})[(\bar{q}_{t2} - \bar{q}_t)(\theta_{l2} - \bar{\theta}_l) + r_{q_t\theta_l}\sigma_{\theta_{l2}}\sigma_{q_{t2}}]\end{aligned} \quad (3.31)$$

$$\begin{aligned}\overline{w'^4} = {} & a\left((w_1 - \bar{w})^4 + 6(w_1 - \bar{w})^2\sigma_{w1}^2 + 3\sigma_{w1}^4\right) \\ & + (1-a)\left((w_2 - \bar{w})^4 + 6(w_2 - \bar{w})^2\sigma_{w2}^2 + 3\sigma_{w2}^4\right) .\end{aligned} \quad (3.32)$$

Expressions for $\overline{w'q_t'^2}$ and $\overline{w'^2q_t'}$ are similar to Eqs (3.29) and (3.30), respectively. In order to compute the buoyancy terms ($\overline{w'\theta_v'}$, $\overline{q_t'\theta_v'}$, $\overline{\theta_l'\theta_v'}$, $\overline{w'^2\theta_v'}$), we first rewrite them as (Bougeault 1981b)

$$\overline{\chi'\theta_v'} = \overline{\chi'\theta_l'} + \frac{1-\epsilon}{\epsilon}\theta_0\overline{\chi'q_t'} + \left(\frac{L_v}{c_p}\left(\frac{p_0}{p}\right)^{R_d/c_p} - \frac{1}{\epsilon}\theta_0\right)\overline{\chi'q_l'}\,, \quad (3.33)$$

where χ' represents w', q_t', θ_l' or w'^2. Here $\epsilon = R_d/R_v$, R_d is the gas constant of dry air, R_v is the gas constant of water vapor, L_v is the latent heat of vaporization, c_p is the heat capacity of air, and p_0 is a reference pressure. The correlations involving liquid water ($\overline{\chi' q_l'}$) can be computed for a given family of PDFs (Larson et al. 2001c, and Appendix A).

As currently formulated, the PDF family does not include the horizontal winds u and v as independent variables. Therefore, we use a traditional down-gradient approach to close the momentum fluxes appearing in Eqs (3.8) and (3.9):

$$\overline{u'w'} = -K_m \frac{\partial \bar{u}}{\partial z} \tag{3.34a}$$

$$\overline{v'w'} = -K_m \frac{\partial \bar{v}}{\partial z} \tag{3.34b}$$

where the turbulent-transfer coefficient K_m is given by:

$$K_m = c_K L \left(\frac{3}{2} \overline{w'^2} \right)^{1/2} \tag{3.35}$$

with $c_K = 0.548$ as in Duynkerke and Driedonks (1987).

The specific values of the constants C_i and ν_i are as follows: $C_1 = 1.7$; $C_2 = 1.04$; $C_4 = 4.5$; $C_5 = 0$; $C_6 = 4.85$; $C_7 = 0.8$; $C_8 = 2.73$; $C_{11} = 0.2$; $\nu_1 = \nu_2 = \nu_8 = 20$ (m^2/s); and $\nu_6 = 30$ (m^2/s). Compared to the values suggested by Bougeault (1981b), C_4, C_5, C_6 are identical. C_2, which controls the damping terms on the variances, was reduced by 20% to bring the variances in cumulus layers more in line with LES. C_7 was also adjusted to improve the magnitude of the turbulent fluxes as compared to the LES. C_8 was significantly reduced and C_{11} was set to the value suggested by André et al. (1982). Bougeault (1981b) selected the constants C_8 and C_{11} to artificially reduce the magnitudes of the third-order moments as compared to the LES, because he found "that large values of the third-order moments lead almost systematically to instability". He speculated that "a

possible lack of consistency between the quasi-Gaussian assumption and the non-Gaussian cloud parameterization may be responsible for this instability". Although the assumed PDF method does not get rid of all sources of instability, it avoids this particular inconsistency and we found it necessary to adjust the values of C_8 and C_{11} to obtain realistic values of $\overline{w'^3}$.

3.3.2 Eddy length formulation

To compute the dissipation time scale τ or the eddy diffusivity coefficient K_w, we need to calculate an eddy length scale, L. To do so, we adopt the method of Bougeault and André (1986) and Bechtold et al. (1992). They construct L from an upward free path, $L_{\rm up}(z)$, and a downward free path, $L_{\rm down}(z)$. They let $L_{\rm up}(z) > 0$ be the distance that a parcel at altitude z can be carried upwards by buoyancy until it overshoots and exhausts its initial kinetic energy. The initial kinetic energy is approximated as the turbulent kinetic energy $\overline{e(z)}$ (Eq. 3.22). Therefore,

$$-\int_z^{z+L_{\rm up}} \frac{g}{\overline{\theta_v(z')}} \left[\overline{\theta_v(z)} - \overline{\theta_v(z')}\right] \, dz' = \overline{e(z)}. \tag{3.36}$$

Similarly, $L_{\rm down}(z) > 0$ is the distance that a parcel can travel downwards under the influence of buoyancy:

$$\int_{z-L_{\rm down}}^{z} \frac{g}{\overline{\theta_v(z')}} \left[\overline{\theta_v(z)} - \overline{\theta_v(z')}\right] \, dz' = \overline{e(z)}. \tag{3.37}$$

Then L must be written as some average of $L_{\rm up}$ and $L_{\rm down}$. We choose the same average as Bougeault and Lacarrère (1989)

$$L = \sqrt{L_{\rm up} L_{\rm down}}. \tag{3.38}$$

When L is large, turbulence is weakly damped; when L is small, turbulence is strongly damped. Equation (3.38) ensures that L tends to become small if either $L_{\rm up}$ or $L_{\rm down}$ becomes small.

We modify these formulas to make them more appropriate for cumulus layers. The formulas for $L_{\rm up}$ and $L_{\rm down}$ assume that a parcel is lifted without dilution or condensation. In a cumulus layer, however, this leads to unrealistically low values of $L_{\rm up}$. To increase the upward free path, we assume that the parcel is moist and entraining. That is, we replace (3.36) with:

$$-\int_{z}^{z+L_{\rm up}} \frac{g}{\overline{\theta_v(z')}} \left[\theta_{v,parcel}(z') - \overline{\theta_v(z')}\right] \, dz' = \overline{e(z)}, \tag{3.39}$$

where $\theta_{v,parcel}$ is the virtual potential temperature of a parcel that starts its ascent with the mean value of θ_v at altitude z and entrains with fractional entrainment rate $\mu = (1/M)dM/dz$. Here M is the mass of the parcel, and we choose $\mu = 6 \times 10^{-4}$ m^{-1}. The calculation of $\theta_{v,parcel}$ assumes that condensation occurs when the parcel exceeds saturation. Lappen and Randall (2001b) also include condensation effects in L.

Despite this modification, our experience is that Eq. (3.39) still appears to underestimate $L_{\rm up}$ in cumulus layers. This is probably because Eq. (3.39) represents a "local" length scale, whereas for cumulus layers in particular a "nonlocal" length scale may be more appropriate. By a local length scale, we mean that Eq. (3.39) assumes that $L_{\rm up}(z)$ is determined by lifting a parcel with the *mean* value of θ_v at the *local* altitude z. In some cases, parcels initiated in the cumulus layer with $\theta_v = \overline{\theta_v(z)}$ may ascend little if at all, whereas parcels initiated at the ground with $\theta_v = \overline{\theta_v(0)}$ may reach a much higher altitude than z. In these cases, it is reasonable to base the length scale at z on the displacement of parcels lifted from lower levels. Therefore, we use the following procedure to make the length scale nonlocal. After computing $L_{\rm up}(z)$, we find the highest altitude, $a_{\rm max} = z'' + L_{\rm up}(z'')$,

attained by all parcels lifted from lower altitudes $z'' < z$. If $a_{\max}$ exceeds the altitude attained by the parcel started at z, i.e. if $a_{\max} > z + L_{\text{up}}(z)$, then we set $L_{\text{up}}(z) = a_{\max} - z$. Then L_{up} equals the highest distance above z reached by parcels ascending through z from below. We follow an analogous procedure to non-localize L_{down}. That is, after computing $L_{\text{down}}(z)$, we find the lowest altitude, $a_{\min} = z''' - L_{\text{down}}(z''')$, attained by all parcels descending from higher altitudes $z''' > z$. If $a_{\min}$ is less than the altitude attained by the parcel started at z, i.e. $a_{\min} < z - L_{\text{down}}(z)$, then we set $L_{\text{down}}(z) = z - a_{\min}$. We can calculate nonlocal versions of L_{up} and L_{down} without adding loops beyond those needed to calculate the local L_{up} and L_{down}.

Finally, we limit the values of L as follows. Following Bechtold et al. (1992), we set a lower limit, $L_{\min}$, on L_{up} and L_{down}. We choose $L_{\min} = 20$ m, so that it is smaller than the vertical grid spacing. Also, instability can develop if L is too large. Therefore, we set an upper limit, $L_{\max}$, on L. When L is used to compute dissipation of variances or K_w, we set $L_{\max} = 400$ m. When L is used to compute dissipation of fluxes, we set $L_{\max} = 2000$ m. The same maximum length scales are used in all simulations. It might, however, be more judicious to have the maximum values scale with the boundary layer depth.

3.3.3 Numerical discretization

Equations (3.8)-(3.18) are discretized on a vertically staggered grid as shown in Fig. 3.5. First and third-order moments are located at grid box centers (zt levels), whereas second and fourth-order moments reside on grid box edges (zm levels). The staggering simplifies the spatial discretization of the prognostic equations; turbulent advection terms, such as $\partial \overline{w'^3}/\partial z$ and $\partial \overline{w'^4}/\partial z$ appearing in the predictive equations for $\overline{w'^2}$ and $\overline{w'^3}$, can be computed directly with a centered in space difference without any interpolation. The production terms ($\overline{w'^2}\ \partial \bar{q}_t/\partial z, \ldots$) in the second-order moments equations can also be discretized

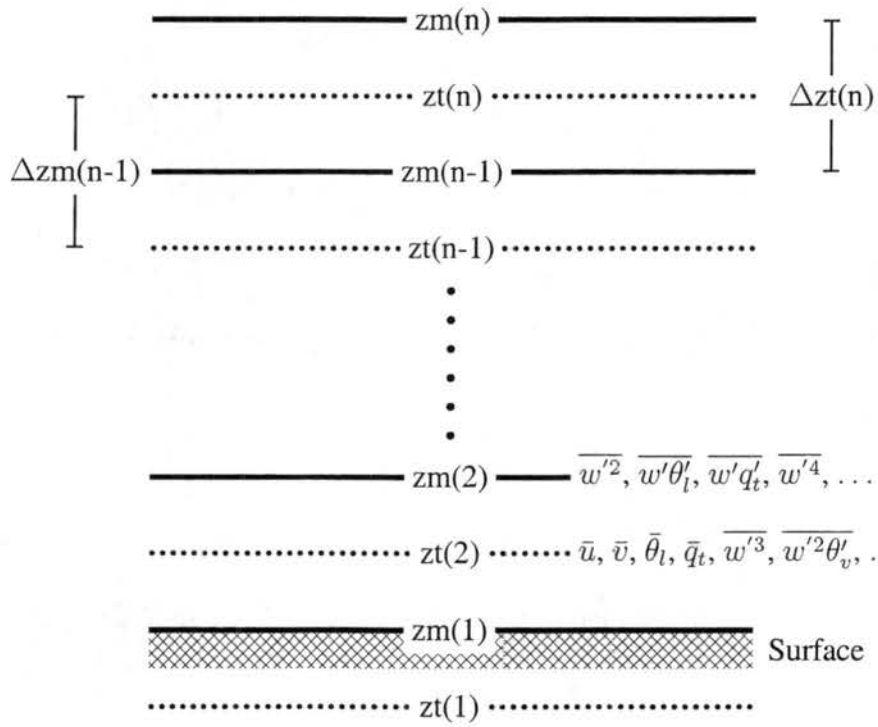

Figure 3.5: Model grid setup. The surface is located at the zm(1) level. First- and third-order moments reside on zt levels, and second- and fourth-order moments on zm levels.

without interpolation. Advection terms by the mean flow ($\bar{w}\ \partial\overline{w'^2}/\partial z, \ldots$) require interpolation from the zm levels to the zt levels or vice versa, which is done using a linear scheme. The PDF closure algorithm is applied at the grid box centers (zt levels); the second-order moments are thus interpolated to the zt levels on input to the PDF closure and the fourth-order moment of the vertical velocity ($\overline{w'^4}$) is interpolated back to the zm levels after output from the PDF closure.

The time discretization uses a nested time step. A short time increment is used to integrate the equations involving the vertical velocity moments (Eqs 3.12 and 3.18), while all the other moment equations are integrated on the regular time step. This makes it possible to significantly increase the main model time increment without causing instability. The time stepping method is explicit, forward in time, for all terms except for the dissipation terms, which are treated implicitly. The horizontal momentum fluxes are also computed implicitly.

Because of the staggered grid configuration, we only need to impose surface boundary conditions for the second and fourth-order moments. The turbulent fluxes of momentum ($\overline{u'w'}$, $\overline{v'w'}$), heat ($\overline{w'\theta_l'}$), and moisture ($\overline{w'q_t'}$) can either be imposed or computed using a bulk aerodynamic formula. The surface values of the variances ($\overline{w'^2}$, $\overline{\theta_l'^2}$, $\overline{q_t'^2}$) are computed as in André et al. (1978). The PDF closure scheme is also called at the surface to obtain a boundary condition for $\overline{w'^4}$ and the second-order buoyancy moments. As input, it uses surface values for the second-order moments and interpolated values from the first level above ground for the means and third-order moments. At the upper boundary, all turbulent moments are set to zero since this level is located high enough above the top of the atmospheric boundary layer.

Finally, Fig. 3.6 gives a visual summary of the various steps involved within each model time step. The model starts by computing large-scale forcings such as advective and

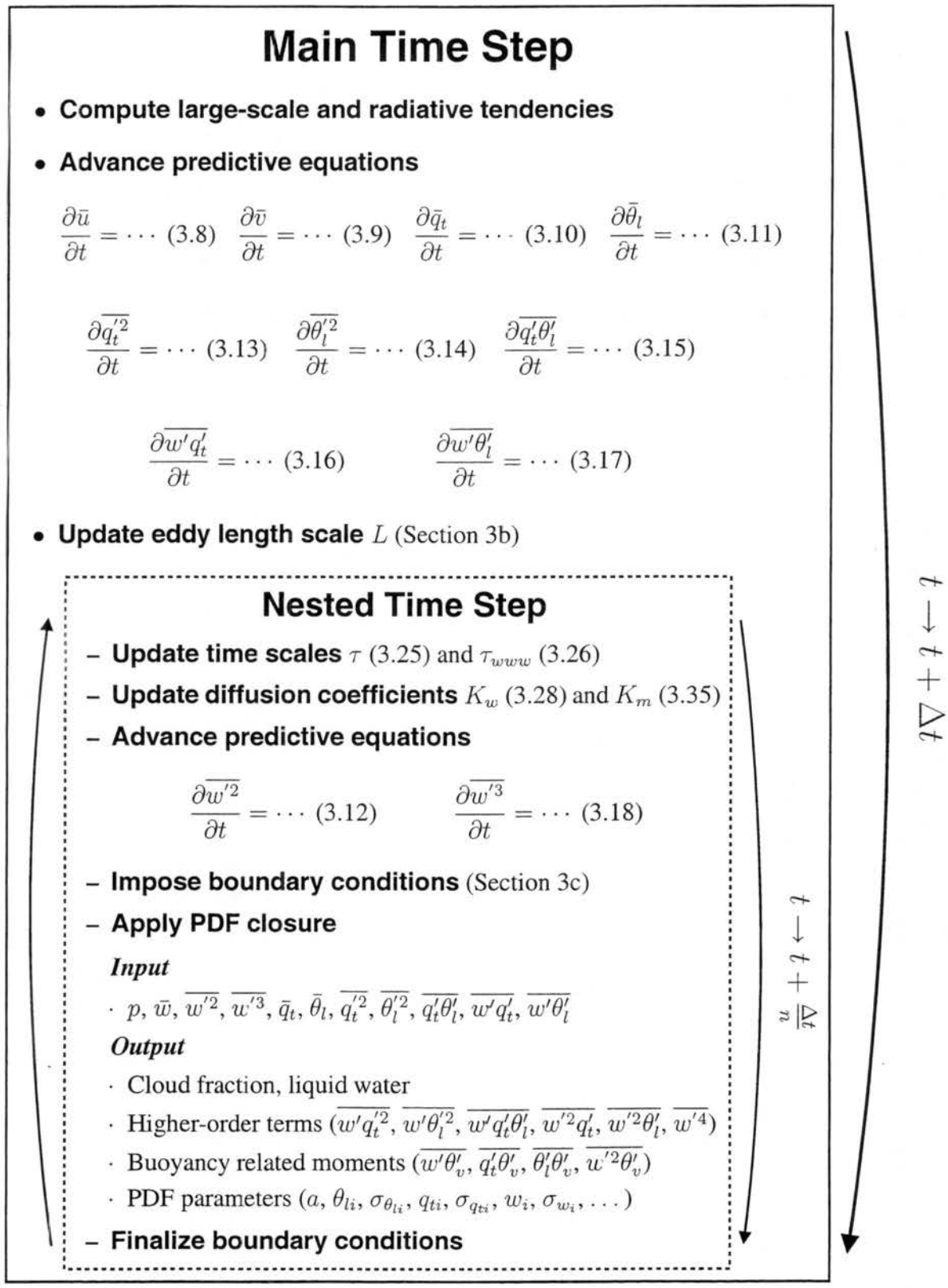

Figure 3.6: Schematic representation of the model time step. Numbers in parentheses refer to equations in the text. Δt is the main time step, and n the time stepping ratio for the nested time step.

radiative tendencies. Equations for the means, as well as equations for the second-order moments with the exception of the vertical velocity variance are then advanced by one time increment. The eddy length scale is then updated using the new mean profiles. The nested time step follows; it updates the dissipation times and diffusivity coefficients, advances the predictive equations for $\overline{w'^2}$ and $\overline{w'^3}$, imposes boundary conditions and calls the PDF closure to close all higher-order and buoyancy terms. The nested time step procedure is typically repeated between 5 and 7 times within each main model time step.

Chapter 4

Single-column model results

4.1 Dry convective layer (Wangara)

As mentioned in Section 2.2.1, the LES and SCM are initialized with profiles of horizontal winds, potential temperature, and water vapor specific humidity measured during day 33 of the Wangara experiment at 0900 LST. The simulations are eight hours long and capture the daytime development of the clear convective layer. The SCM was initialized and configured identically to the LES. The vertical grid increment was 40 m, the main model timestep 12 s, and the nested time step 2 s.

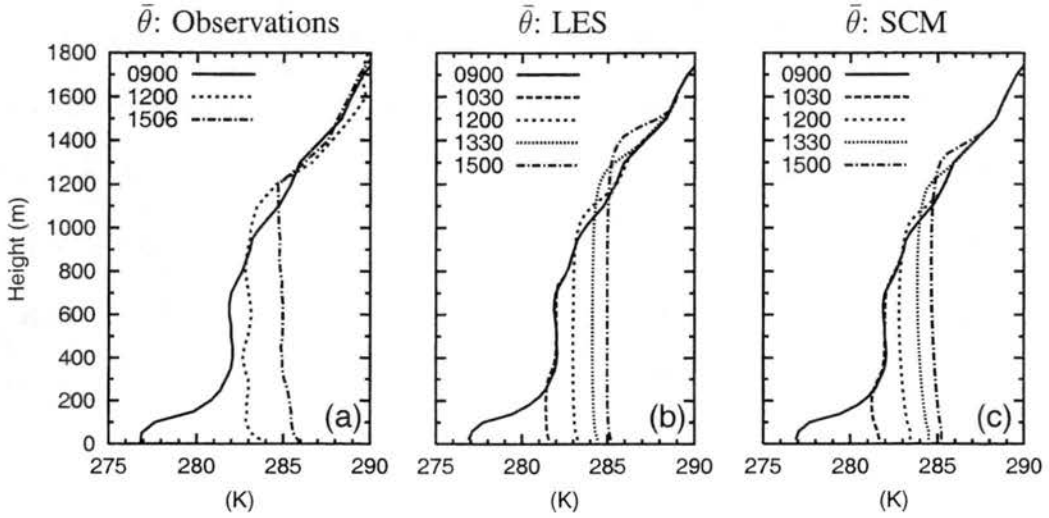

Figure 4.1: Profiles of potential temperature observed during the Wangara day 33 (a) and simulated by the LES (b) and the parameterization (c).

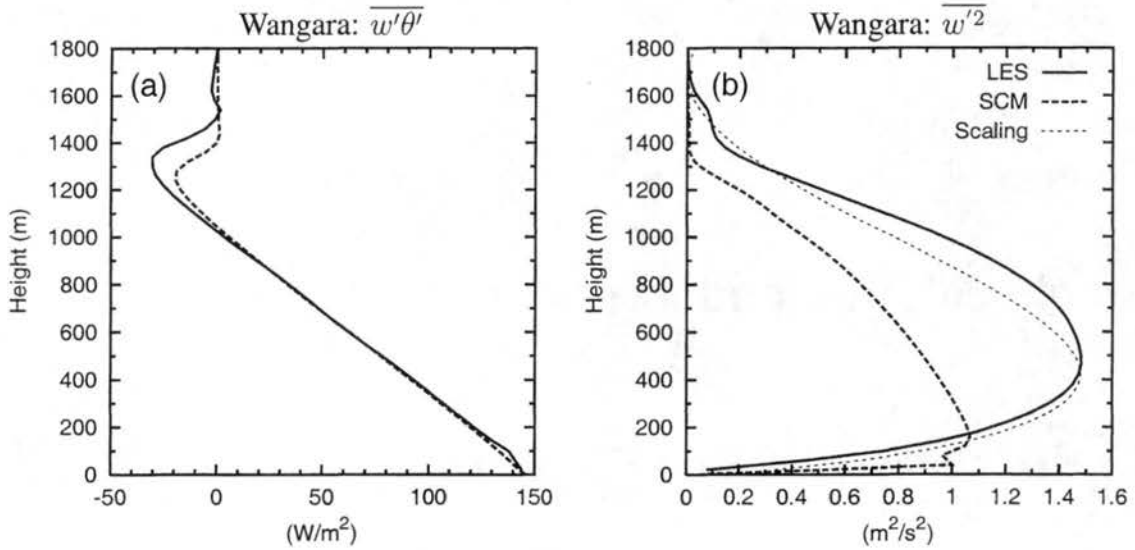

Figure 4.2: Comparison of heat flux (a) and vertical velocity variance (b) between the LES and the SCM; averaged between 1400 and 1500 LST of the Wangara day 33 experiment. LES results are shown in thick solid lines, and SCM in thick dashed lines. The thin dashed line in (b) is the mixed layer scaling proposed by Lenschow et al. (1980).

Figure 4.1 depicts the observed profiles of the potential temperature along with the LES and the SCM results at various times. As mentioned in Section 2.2.1, the mixed-layer values of potential temperature are very similar between the observations and the LES. The main difference is an overestimation of the boundary layer depth by the LES at 1330 and 1500 LST. Boundary layer growth in the parameterization differs only in minor ways from the LES. The SCM tends to produce a convective layer that is less well mixed than the LES, and that has a smaller entrainment rate. At 1500 LST, the top of the boundary layer is located near 1300 m for the parameterization compared to 1400 m in the LES. The inversion capping the top of the convective layer is also slightly less sharp in the SCM than the LES.

The entrainment rate is physically linked to the magnitude of the heat flux at the top of the convective layer. Although the heat flux is essentially the same between the SCM and the LES throughout most of the boundary layer, it exhibits a larger difference in the

entrainment zone where the LES produces a more negative flux (Fig. 4.2a). The minimum values are -32 for the LES and -20 W m^{-2} for the SCM. The ratios of the heat flux at the top of the mixed layer to the surface values are -0.22 and -0.14, respectively. Compared to the generally accepted value of -0.2, the smaller SCM ratio is another indication of the lower entrainment rate. A look at the LES and SCM heat flux budgets (not shown) reveals that the probable cause for this difference is the smaller buoyancy term ($\overline{\theta_l' \theta_v'}$) in the SCM compared to the LES. This is the case because the temperature variance ($\overline{\theta_l'^2}$) is itself smaller than in the LES.

It well recognized than in the upper half of a convective boundary layer, the heat flux is generally positive and the temperature lapse rate slightly stable, implying that the heat flux is counter-gradient (e.g. Deardorff 1966). Parameterizations that utilize a local down-gradient closure for the fluxes cannot capture the proper sign of the potential temperature gradient in the upper part of a convective layer. This has frequently been seen as a shortcoming of these local schemes (e.g. Stull 1988; Ebert et al. 1989). Although not visually apparent in Fig. 4.1b, the LES simulation of Wangara day 33 generates a slightly stable lapse rate in the upper half of the mixed layer. Interestingly, it is also the case for the SCM, although the gradient is exaggerated. This indicates that the parameterization is capable of producing a counter-gradient heat flux.

The vertical velocity variance ($\overline{w'^2}$) is depicted in Fig. 4.2b. The LES has a maximum variance of 1.5 $m^2 s^{-2}$ at a height of 500 meters, whereas the SCM exhibits a smaller maximum value of 1.1 $m^2 s^{-2}$ located at a lower height, around 200 meters above ground. Also shown is the mixed layer scaling proposed by Lenschow et al. (1980):

$$\frac{\overline{w'^2}}{w_*^2} = 1.8\,(z/z_i)^{2/3}\,(1 - 0.8z/z_i)^2 \tag{4.1}$$

where w_* is the convective velocity scale and z_i the mixed layer depth. These values are $w_* = 1.78$ m/s and $z_i = 1350$ m for the data shown in Fig. 4.2b. The agreement between

the scaled velocity variance given by (4.1) and the LES variance is good. The agreement with the SCM is less satisfying, the two main deficiencies are that the SCM produces values of $\overline{w'^2}$ that are too small with a peak that is located too low in the mixed layer. Three terms dominate the budget for $\overline{w'^2}$. They are buoyancy production, turbulent transport and dissipation. The buoyancy production term follows the heat flux (Fig. 4.2a). The turbulent transport term has a similar shape as the LES, but with a slightly smaller magnitude in the SCM. The biggest difference is the dissipation term, which is generally too large and tends to decrease more with height in the SCM than in the LES. The shape of the eddy mixing length profile is a likely cause of this difference and therefore by extension of the difference between the LES and SCM $\overline{w'^2}$ profiles.

Overall, the simulation of day 33 of the Wangara experiment shows that the SCM is capable of simulating the time evolution of a dry convective boundary layer reasonably well. The main differences are a slightly lower entrainment rate and a less well-mixed layer in the SCM as compared to the LES.

4.2 Trade-wind cumulus (BOMEX)

The trade-wind cumulus simulation is based on BOMEX (Section 2.2.2, p. 14). The LES and the SCM were both initialized with identical profiles of horizontal winds, temperature, and moisture. They were run for six hours. The SCM used the same vertical grid spacing as the LES (40 m). The SCM main time step was 20 s and the nested time step 4 s. Similarly to Siebesma et al. (2001), results presented here are averaged over the last three hours of the simulation, unless denoted otherwise explicitly.

Figures 4.3a,b show the initial profiles of θ_l and q_t, as well as the LES and SCM outputs. The LES mean profiles obtained after six hours of simulation are almost identical to the initial conditions, reflecting a near steady-state regime. Profiles from the SCM are

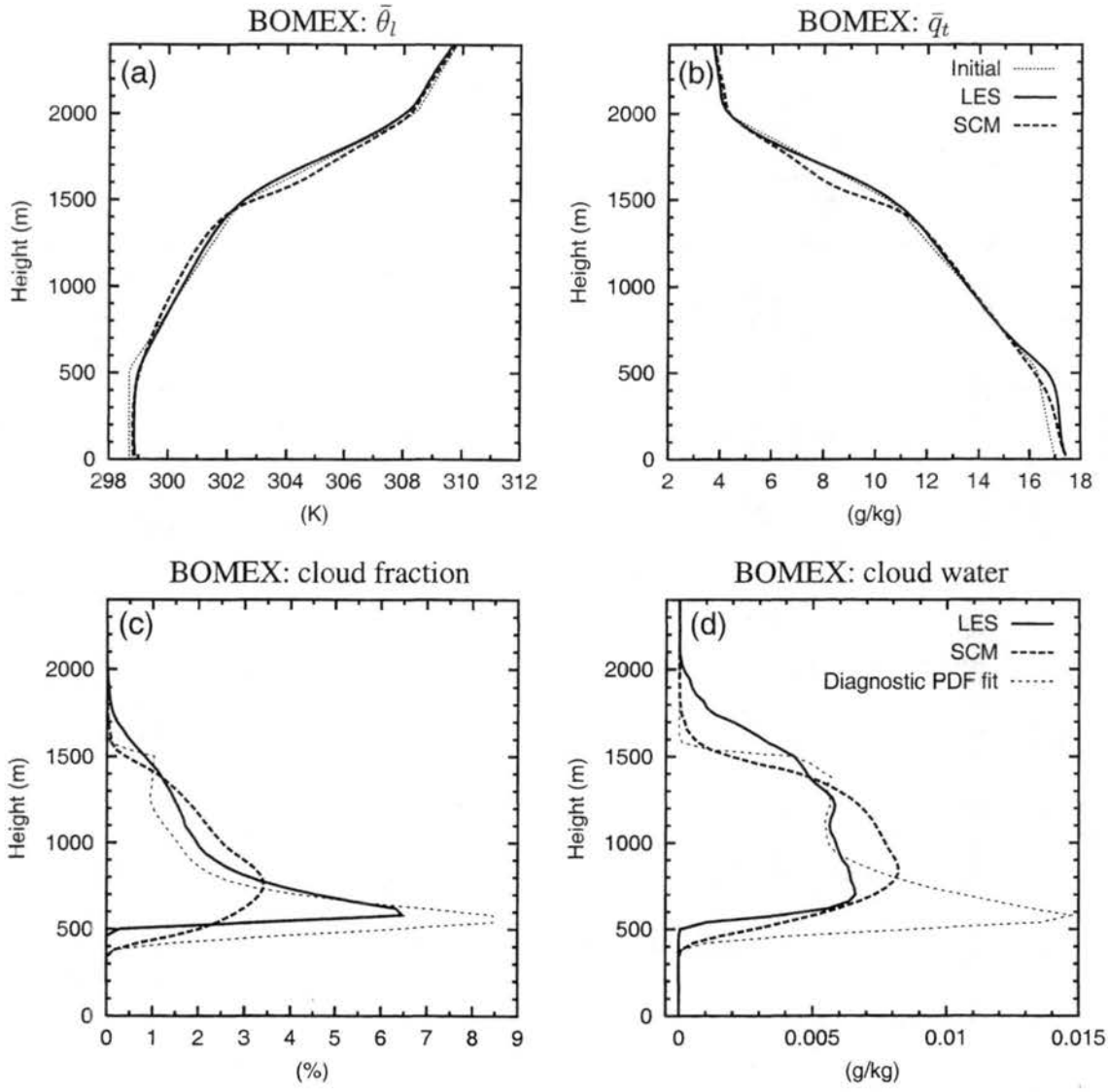

Figure 4.3: Mean profiles of liquid water potential temperature (a), total water specific humidity (b), cloud fraction (c), and liquid water (d) for BOMEX. Thick solid lines represent LES results and thick dashed line SCM results, both averaged over the last three hours of the simulation. Thin dotted lines in panels (a) and (b) represent initial profiles; thin dashed lines in (c) and (d) show cloud properties obtained using a diagnostic PDF fit to the LES data.

very similar to those of the LES. The mixed layer q_t profile is not as well mixed as in the LES but θ_l is identical in this layer. The moisture gradient in the conditionally unstable layer between 600 and 1500 m is well preserved by the SCM, but the temperature lapse rate becomes a little bit more unstable. Larger differences are observed in the stable layer. The SCM tends to alter the strength of this layer as evidenced by the θ_l and q_t differences between 1500 and 1800 meters. Nevertheless, the parameterization is capable of maintaining the three layer structure of the trade-wind cumulus atmosphere throughout the duration of the simulation.

Cloud profiles are depicted in Figs. 4.3c,d. The LES produces maximum cloud fraction and liquid water values near cloud base, with profiles decreasing with height. This is typical of a layer-average over an ensemble of cumulus clouds where there is a relatively large number of shallow clouds with only a few clouds reaching the domain-maximum cloud top. Even though individual cumuli have liquid water profiles that increase with height in their core (e.g. Stevens et al. 2001; Siebesma et al. 2001), the averaged cloud water profile decreases with height due to the predominance of smaller clouds. The SCM, whose predictive equations are intended to model layer averages, is capable of representing the average decrease in cloud fraction and liquid water with height. The maximum cloud fraction produced by the LES is approximately 6% at cloud base. Although the SCM also exhibits a maximum near cloud base, it is smaller (3.5%). In the upper portion of the cloud, between 800 and 1500 m, the SCM slightly overestimates cloud amount. Small differences in cloud base and cloud top are also noticeable. The parameterization underestimates cloud base by approximately 100 m, and cloud top by a larger amount. Results from the GCSS intercomparison workshop showed that many parameterizations had difficulty simulating the low cloud fraction of this trade-wind cumulus case [1].

[1] Cara-Lyn Lappen, personal communication

Similar trends are apparent in the liquid water profiles (Fig. 4.3d). In the main part of the cloud layer, between 600 and 1500 m, the parameterization generates a maximum liquid water approximately 30% larger than the LES, but underestimates the amount of condensate higher up. The LES liquid water path (LWP) is 5.92 g m^{-2} and the SCM is 7.43 g m^{-2}. One should note, however, that the total layer-averaged amount of liquid water is extremely small, in large part due to the low cloud fraction. Parameterizations typically have difficulties predicting such low amounts of condensate. For instance, results presented at the GCSS intercomparison for this case show that the LES models predict a maximum cloud water amount of about 0.006 g kg^{-1}, whereas one-dimensional parameterizations obtained between 0.02 and 1 g kg^{-1} [2]. Lappen and Randall (2001b) obtain a cloud water profile that varies between 0.02 and 0.05 g kg^{-1}.

SCM cloud fraction and cloud water are diagnosed using the joint PDF. The PDF is selected from the underlying family of PDFs based on the values of the turbulent moments. The differences between the LES and SCM cloud properties can therefore be a result of two different factors: (i) a difference between the SCM and LES predicted moments, or (ii) even if the SCM and LES moments coincide, the assumed shape of the SCM PDF may differ from the LES PDF, leading to differences in the SCM diagnosed cloud fraction, liquid water, and higher-order moments. Of course, errors in the assumed PDF shape (factor ii) can lead to errors in prognosed moments (factor i) at later times. The limitations of the family of PDFs can be tested by simply applying the PDF closure *diagnostically* to the LES predicted moments to obtain cloud properties. The resulting cloud fraction and liquid water are depicted in Figs. 4.3c,d with thin dashed line. These profiles exhibit lower cloud base and cloud top, similarly to the SCM. This indicates that the underestimation of cloud base and top by the parameterization is largely a result of factor (ii). The shape of the

[2] http://www.knmi.nl/~ siebesma/gcss/bomex.html

cloud fraction produced by the PDF fit is closer to the LES cloud fraction than it is to the SCM, and so is the liquid water, except in the lowest part of the cloud where the PDF fit significantly overestimates cloud water. Differences between SCM and LES cloud amount thus appear to result from a combination of factors (i) and (ii).

Now we examine how close the LES and SCM moments are. Second and third order moments of the vertical velocity ($\overline{w'^2}$, $\overline{w'^3}$) are shown in Figs. 4.4a,b. The LES $\overline{w'^2}$ has two regions of maximum values, one in the subcloud layer near 200 m and one within the upper part of the cloud layer between 1000 and 1800 m. Between the two, $\overline{w'^2}$ minimizes near cloud base. The subcloud layer has a structure similar to a dry convective layer and similarity theory can be applied there (Siebesma et al. 2001). The $\overline{w'^2}$ structure is typical of cumulus boundary layers. The SCM produces a similar profile with maxima in the subcloud and cloud layers, and a minimum at cloud base. The SCM $\overline{w'^2}$ is, however, approximately 30% larger than in the LES within the lowest 1400 m of the boundary layer. This may be a reflection that the eddy mixing length causes the dissipation term to be slightly too weak in the SCM. $\overline{w'^2}$ extends higher in the LES, likely due to higher cloud tops and wave activity in the stable layer above the clouds. Even though the lower cloud tops are partly due to the family of PDFs, the absence of liquid water in the upper part of the domain feeds back into the turbulent moments due to the lack of condensational heating. $\overline{w'^3}$ obtained by the LES and the SCM are very similar. Both exhibit a maximum in the upper part of the cloud layer and a local minimum near cloud base, although it is not nearly as pronounced in the SCM. The general increase in $\overline{w'^3}$ throughout the cloud layer indicates that the cloud updrafts become narrower and more vigorous with height. This is to be expected. The area occupied by updrafts becomes narrower because only a fraction of the cumulus clouds extend to the domain-maximum cloud top. They become more vigorous because the vertical velocity at the cloud core increases with height (e.g. Siebesma and Cuijpers 1995).

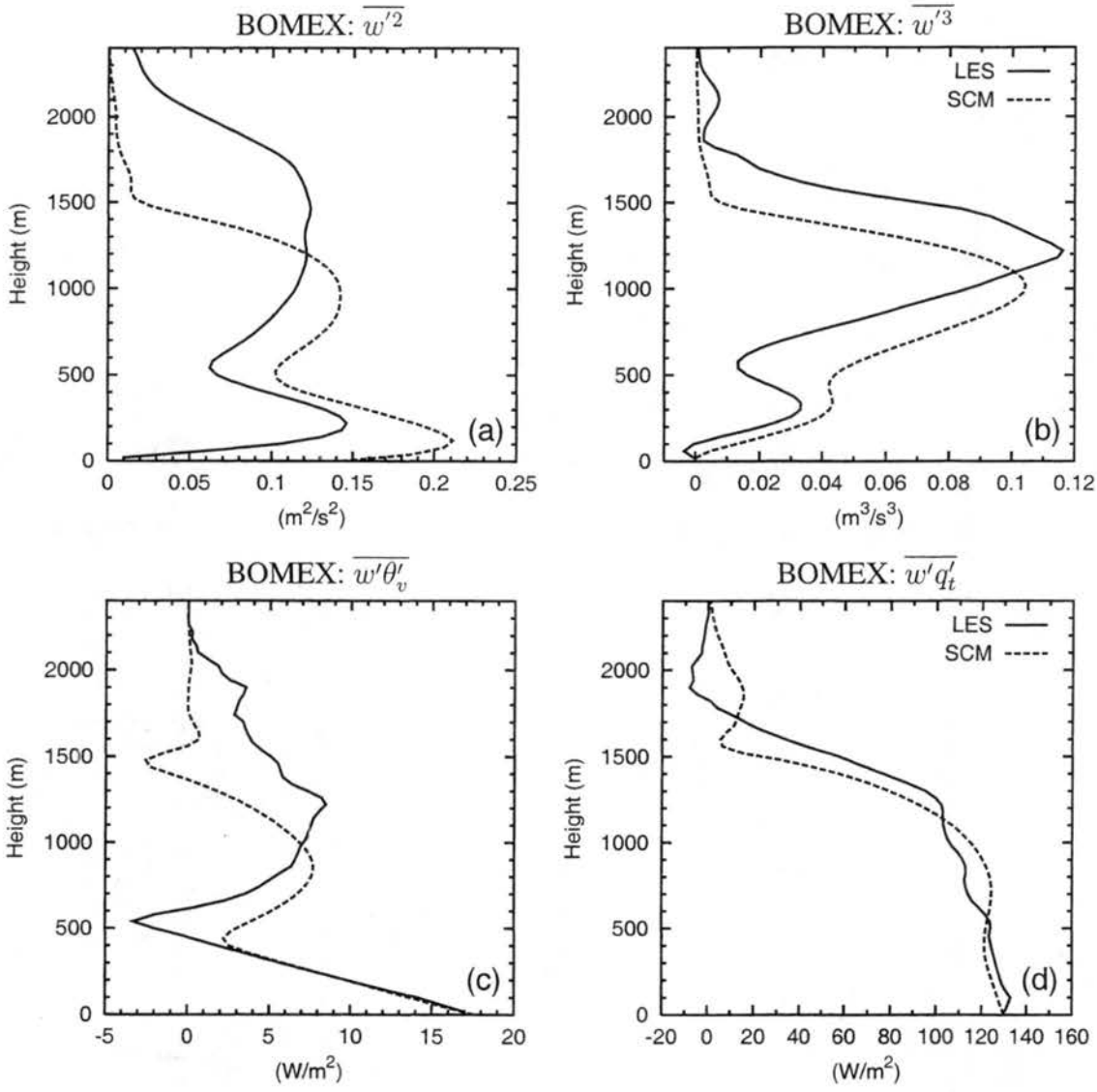

Figure 4.4: Profiles of $\overline{w'^2}$ (a), $\overline{w'^3}$ (b), $\overline{w'\theta'_v}$ (c), and $\overline{w'q'_t}$ (d) averaged over the last three hours of the BOMEX simulation. Solid lines are LES results and dashed lines SCM outputs.

The buoyancy flux ($\overline{w'\theta_v'}$, Fig. 4.4c) decreases linearly in the subcloud layer reaching a minimum near cloud base. It increases again in the cloud layer due to the contribution of the liquid water flux. Because buoyancy generates turbulence, the cloud $\overline{w'\theta_v'}$ base minimum is colocated with the $\overline{w'^2}$ minimum and so are the cloud maxima. The LES and SCM fluxes are comparable, with the major difference in the upper part of the domain. Because the SCM produces shallower clouds, it does not generate any liquid water flux above 1600 m, in contrast to the LES. For the total water fluxes (Fig. 4.4d), the LES exhibits a moderate negative gradient from the surface up to 1300 m, indicating a slight moistening of this layer, topped by a larger gradient between 1300 to 1900 m, where most of the surface moisture ventilated by the clouds is deposited. The SCM flux is generally comparable, with two notable exceptions. The gradient of the water flux reverses sign between 400 and 700 m and 1600 and 1900 m, reflecting a drying of these two layers. Not surprisingly, these layers are where the mean humidity profile of the SCM differs the most from the LES (Fig. 4.3b).

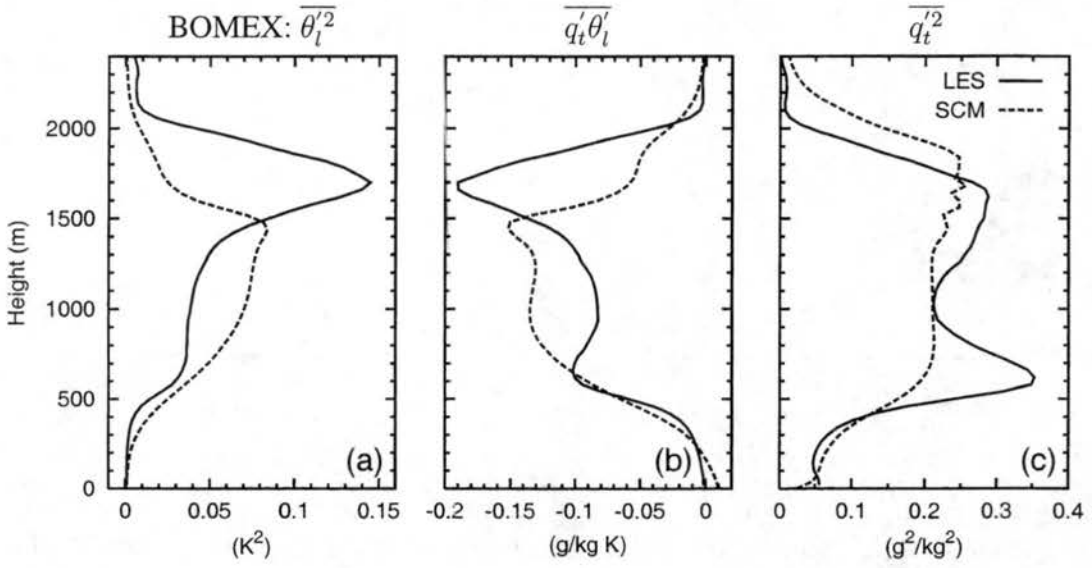

Figure 4.5: Profiles of $\overline{\theta_l'^2}$ (a), $\overline{q_t'\theta_l'}$ (b) and $\overline{q_t'^2}$ (c) averaged over the last three hours of the BOMEX simulation. Solid lines are LES results and dashed lines SCM outputs.

The variances $\overline{\theta_l'^2}$ and $\overline{q_t'^2}$, and the covariance $\overline{q_t'\theta_l'}$ are shown in Fig. 4.5. $\overline{\theta_l'^2}$ reach their

maximum values near cloud top with a variance of 0.14 K^2 at 1700 m for the LES and 0.08 K^2 at 1500 m for the parameterization, reflecting again the lower cloud tops. The increase in variance with height below cloud top is slightly more gradual in the SCM than it is in the LES. Differences between the LES and SCM $\overline{q_t'\theta_l'}$ mirror those of $\overline{\theta_l'^2}$. $\overline{q_t'^2}$ are comparable except near cloud base where the LES predicts a large maximum in variance not present in the SCM model. The LES maximum is a reflection of the larger moisture gradient between the subcloud and cloud layers (Fig. 4.3b). It might even hint to the presence of a transitional layer between the subcloud and cloud layers. Stevens et al. (2001) notes that transitional layers are typically more readily identified from the humidity than from the temperature profiles, which might explain why a similar cloud base maximum is not apparent in the temperature variance. Surprisingly, and in contrast to all the other moments shown previously, the SCM-generated moisture variance drops off at a higher elevation than it does in the LES. It is not exactly clear to us why this is happening. One hypothesis is that the relatively large moisture gradient between 1600 and 2000 m acts in conjunction with the residual total water flux in this layer to generate spurious total moisture variance through the production term $-2\overline{w'q_t'}\frac{\partial \bar{q}_t}{\partial z}$. This may not happen for $\overline{\theta_l'^2}$ because $\overline{w'\theta_l'}$ (not shown) is comparatively smaller than $\overline{w'q_t'}$ in the layer between 1600 and 2000 m.

The comparison of the LES and SCM results would not be complete without showing some examples of PDFs. PDFs from the LES and SCM as well as diagnostic PDF fits to the LES data are displayed in Fig. 4.6 for the last hour of the simulation. Two heights have been selected; near cloud base (z=620 m) and in the middle of the cloud layer (z=1020 m). Projections of the joint PDFs are shown on the w, θ_l, and q_t axes. The PDFs of w are positively skewed, with a long tail extending on the positive side of the distribution. The LES PDF has a tail extending up to 2 m s^{-1} at 620 m and up to 4 m s^{-1} at 1020 m. This long tail is characteristic of cumulus layers and is composed of the cloud cores, where

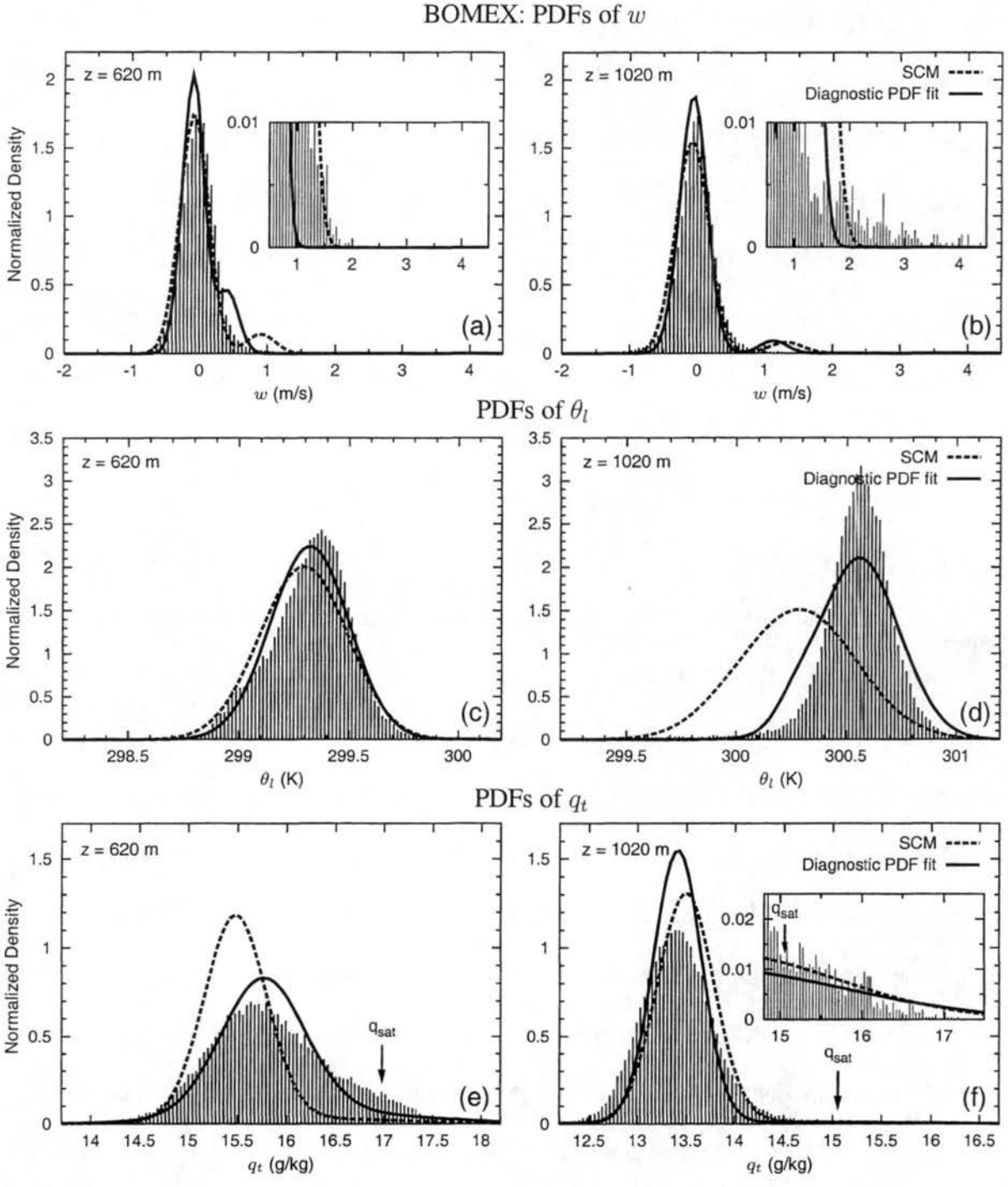

Figure 4.6: Examples of PDFs of w, θ_l, and q_t over the last hour of the BOMEX simulation. Thin vertical lines show the actual LES distributions, thick dashed lines the PDFs predicted by the SCM, and thick solid lines the PDF fits to the LES data. Vertical arrows in (e) and (f) indicate the mean state saturation specific humidity.

the vertical velocity and moisture content are high. Because velocities at the core of the clouds increase with height, it is not surprising that the tail of the distribution is longer at 1020 m than at 620 m. The tail is captured by the SCM and the LES PDF fit, except that it is narrower than in the original distribution. For the PDFs of θ_l and q_t, the LES PDF fit produces distributions that more closely resemble the original data, which is expected since the fitted PDF is exactly matches the LES moments. The differences between the SCM and LES PDF fit reflect the mismatch of some of the SCM moments. For example, the SCM PDF of θ_l at z=1020 m (Fig. 4.6d) is shifted to the left and is too broad. This is because at this height, the SCM predicts a lower mean (Fig. 4.3a) and a higher variance (Fig. 4.5a).

The mean state saturation specific humidity is shown along with the PDFs of q_t. It is the saturation value given by the layer-averaged $\bar{\theta}_l$ and $\bar{q}_t$ and provides an indication of where the distribution lies relative to the mean saturation. However, this does not imply that all the points to the right of the arrows are cloudy and the ones to the left are clear. This is because the saturation curve is a line on the θ_l and q_t plane [see for instance Figs. 1 and 2 in Larson et al. (2001c)] which does not project to a single point on the q_t axis. Nevertheless, the mean saturation provides useful information. At 620 m (Fig. 4.6e), a significant fraction of the distribution lies to the right of the mean saturation, whereas at 1020 m, a much smaller fraction does so (Fig. 4.6f), reflecting the decrease in cloud fraction between these levels. The PDF of q_t at 1020 m exhibits a long tail extending up to 17 g kg^{-1}, which is almost to the surface q_t value. This illustrates the well-recognized fact that a portion of the air found in cloud cores has risen almost undiluted from the surface. The long q_t tail at 1020 m is captured quite realistically by the diagnostic PDF fit as well as the SCM.

4.3 Cumulus over land (ARM)

The second case of cumulus cloud is a continental case based on observations from the ARM site (Section 2.2.3, p. 17). The SCM used the same initialization and forcings as the LES simulation. The SCM vertical grid spacing was 40 m, the main time step 20 s, and the nested time step 2.86 s. The ARM case complements BOMEX in the sense that the convection is more vigorous, with higher cloud fraction and liquid water values. It is also not a steady-state case, as the imposed surface fluxes exhibit large diurnal variations. This diurnal cycle is reflected in the cumulus cloud field, which allows us to test the timing of the onset and decay of the convection between the LES and the SCM.

The time evolution of the LES and SCM cloud fraction is shown in Fig. 4.7. A one-hour running filter was applied to the LES cloud fraction because the instantaneous domain-averaged cloud fractions exhibited large intermittency on time scales shorter than one hour. This intermittency is a consequence of the relatively small horizontal LES domain and would presumably decrease with larger domains capable of containing a more representative sample of clouds at any given time. No such filtering was applied to the SCM results. Using the 1% contour line as a measure of the onset and decay of the convection, the timing is very similar between the two models, with the first clouds appearing around 1530 UTC and the last ones dissipating around 0030 UTC. The evolution of cloud base during the course of the simulation is also in good agreement, with the main difference being a slightly lower cloud base in the SCM. Cloud top is also underestimated in the SCM by a few hundreds meters. The LES produces a large maximum in cloud fraction of 18% around 1800 UTC. In comparison, the SCM produces a much smaller maximum value just over 10%, delayed by approximately 30 minutes and at a higher altitude. The reason for the smaller SCM maximum cloud fraction is probably twofold. First, as mentioned earlier, the

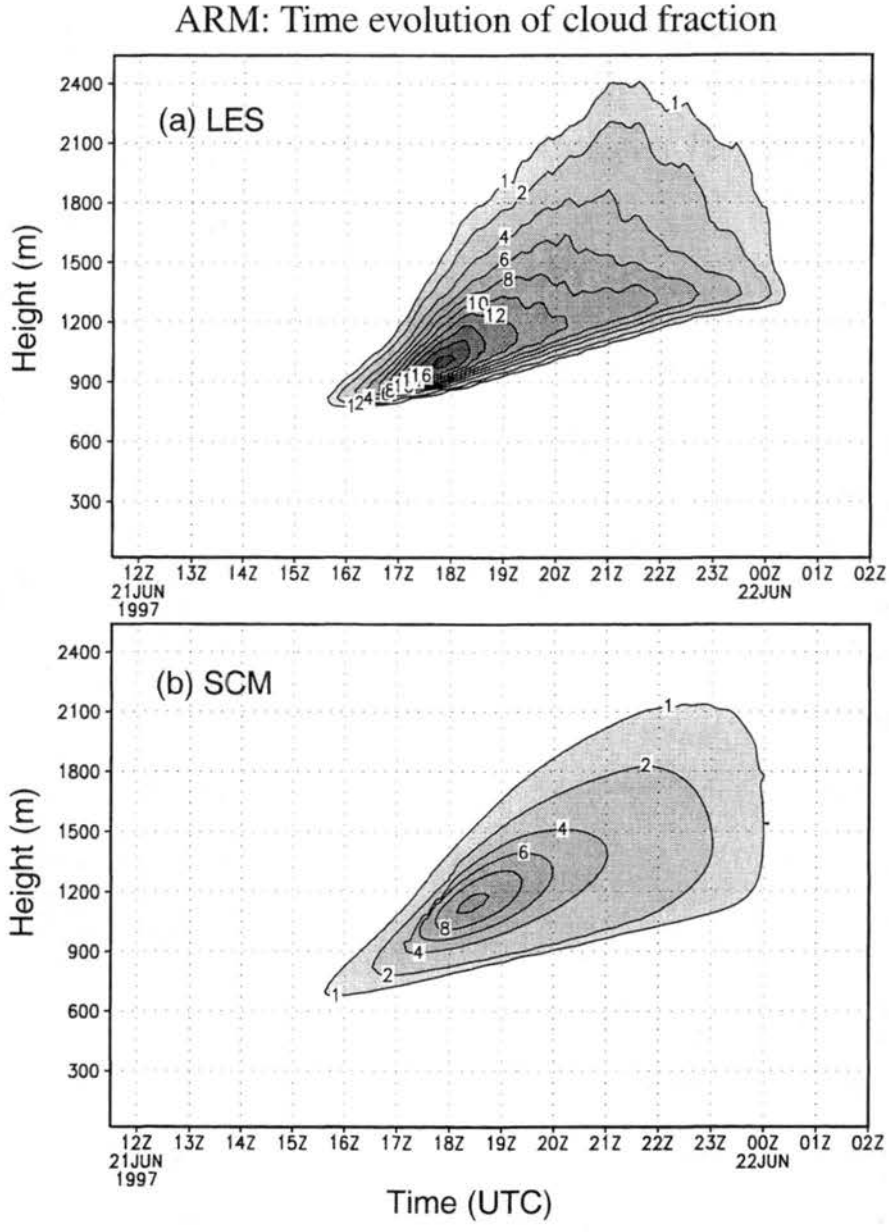

Figure 4.7: Time evolution of the cloud fraction (%) produced by the LES (a) and the SCM (b) for the ARM case. A 60 minutes running average has been applied to the LES cloud fraction to smooth out intermittency.

LES exhibits considerable intermittency not present in the SCM, and therefore produces larger extreme values. Second, as we show later in the text, the family of PDFs tends to underestimate maximum cloud fraction.

We now present profiles of various quantities averaged between 1900 and 2000 UTC, corresponding to the period when the surface heating is the strongest. Figures 4.8a,b depict $\bar{\theta}_l$ and $\bar{q}_t$ for both models during this time along with their initial values. The LES $\bar{\theta}_l$ increases in the lower part of the domain under the influence of surface heating and a subcloud mixed-layer approximately 1000 m deep develops. The venting of near surface air by the clouds causes θ_l to decrease between 1100 and 2000 m. The LES humidity profile becomes moister throughout most of the domain, with the biggest increase in the subcloud layer as a result of the large surface latent heat flux. The SCM profiles at the same time are almost identical to the LES. This demonstrates that the SCM can realistically simulate the evolution of $\bar{\theta}_l$ and $\bar{q}_t$.

Cloud fraction and liquid water profiles for the same time period are shown in Figs. 4.8c,d. As was the case for BOMEX, the LES cloud fraction maximizes near cloud base and then decreases with height. The parameterization generates a similar shape, but with overall smaller cloud fraction values; the maximum is 8% compared to 12% for the LES. As in BOMEX, both cloud base and cloud top are underestimated, cloud base by approximately 100 m and cloud top by a larger amount of 200 to 300 m. The maximum amount of liquid water produced by the LES is approximately 0.028 (g/kg), which is almost five times larger than in BOMEX. The SCM underestimates cloud water by 30%. It is encouraging to note that for both BOMEX and ARM, the SCM model was capable of producing cloud water amounts within 30% of the LES, despite nearly a factor five increase in overall liquid water. The differences in LWP are accentuated by the difference in cloud depth. The LES LWP is 22.04 g m^{-2} and the SCM value is 12.47 g m^{-2}, approximately 43% smaller.

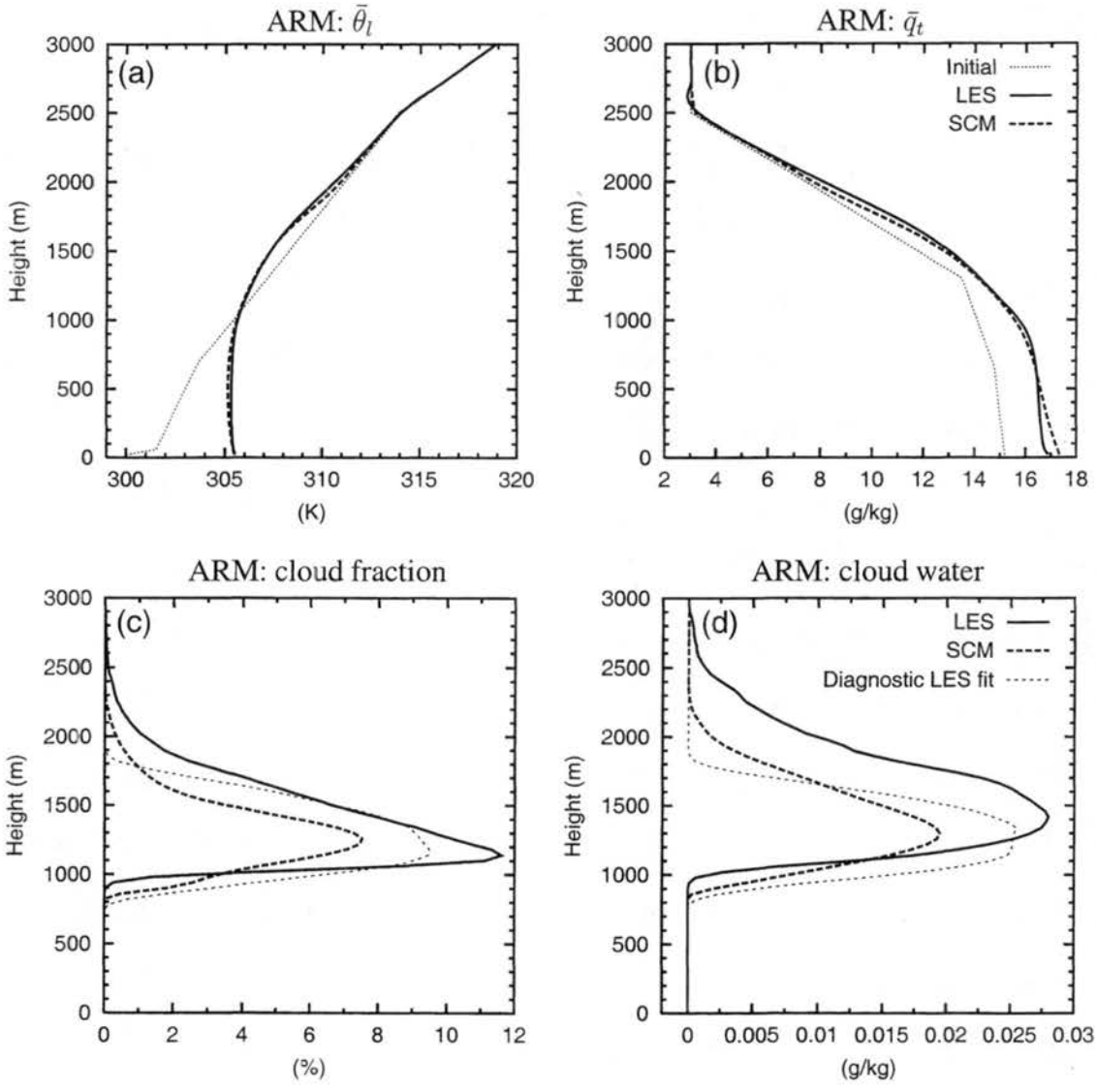

Figure 4.8: Mean profiles of liquid water potential temperature (a), total water specific humidity (b), cloud fraction (c), and liquid water (d) for the ARM case. Thick solid lines LES results and thick dashed line SCM results, both averaged between 1900 and 2000 UTC. Thin dotted lines in panels (a) and (b) represent initial profiles; thin dashed lines in (c) and (d) show cloud properties obtained using a diagnostic PDF fit to the LES data.

Also shown in Figs. 4.8c,d are the diagnostic cloud properties obtained by fitting the family of PDFs to the LES moments. As was the case for BOMEX, cloud base and cloud top are also underestimated, which indicates that the family of PDFs is at least partially responsible for this underestimation in the SCM. However, the magnitudes of cloud fraction and liquid water obtained by the diagnostic LES fit are closer to the true LES values in the lower part of the cloud than they are to the SCM predicted values. This points to the misprediction of the SCM moments as the most likely culprit for the underestimation of cloud amounts in the SCM.

The vertical velocity variance profile ($\overline{w'^2}$, Fig. 4.9a) has a structure similar to BOMEX, with one maximum in the subcloud layer, another in the cloud layer and a minimum near cloud base. However, the actual values are much larger reflecting a more vigorous mixing due to the strong surface heating over land. The SCM variance is comparable to the LES except in the upper part of the domain where it drops off too rapidly, presumably because of the lower cloud top. The SCM subcloud $\overline{w'^2}$ peak is too low compared to the LES, similar to Wangara. The $\overline{w'^3}$ profiles (Fig. 4.9b) are comparable with the exception of larger in-cloud values produced by the SCM. We will discuss this further when we present plots of PDFs of w. The difference in the buoyancy flux between the LES and the parameterization (Fig. 4.9c) is greatest in the cloud layer and is associated with the smaller SCM cloud water amount and the lower cloud top. The total water flux (Fig. 4.9d) is generally smaller in the parameterization, indicating less vigorous mixing. Between the surface and 1500 m, the gradient of $\overline{w'q_t'}$ has a different sign in the LES and the SCM. The LES gradient indicates a drying of this layer, whereas the SCM gives a slight moistening. As mentioned before, the LES time evolution exhibits considerable intermittency in convective activity over short periods of time. When the cumulus activity is very strong, the clouds vent moisture out of the boundary layer faster than the surface latent heat flux can replenish, leading to a

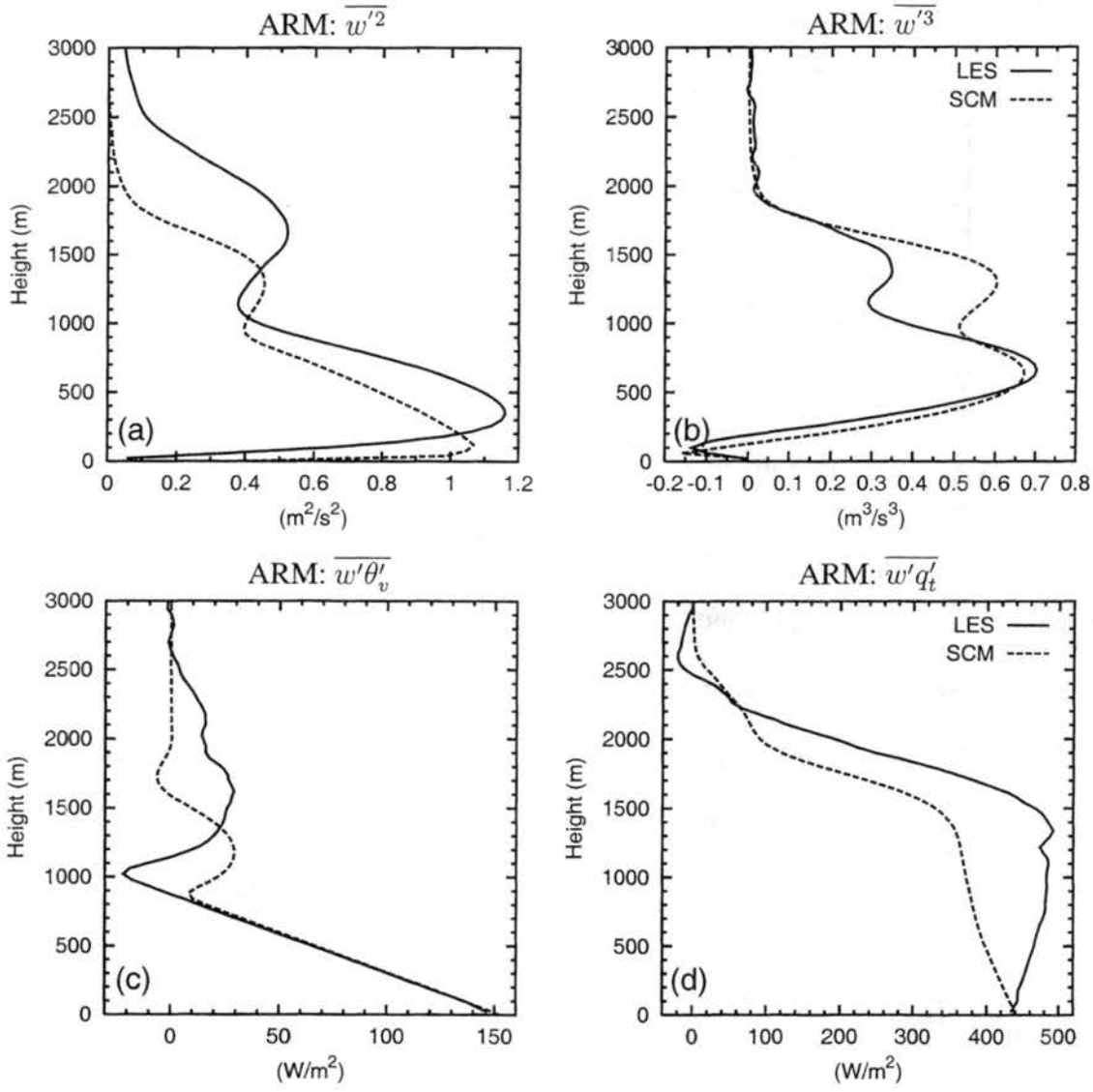

Figure 4.9: Profiles of $\overline{w'^2}$ (a), $\overline{w'^3}$ (b), $\overline{w'\theta'_v}$ (c), and $\overline{w'q'_t}$ (d), averaged between 1900 and 2000 UTC of the ARM simulation. Solid lines are LES results and dashed lines SCM outputs.

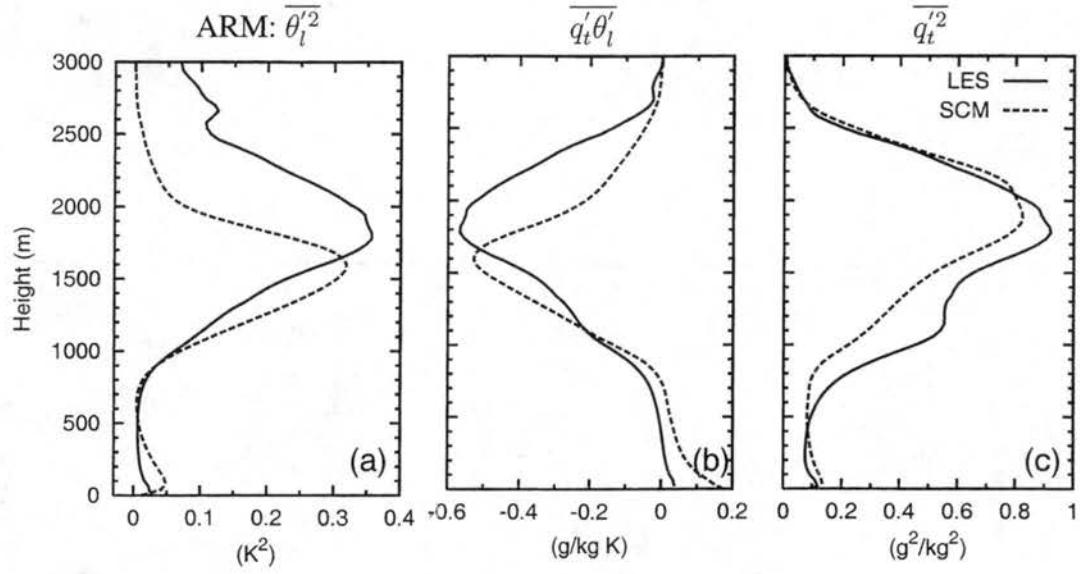

Figure 4.10: Profiles of $\overline{\theta_l'^2}$ (a), $\overline{q_t'\theta_l'}$ (b), and $\overline{q_t'^2}$ (c) averaged between 1900 and 2000 UTC of the ARM simulation. Solid lines are LES results and dashed lines SCM outputs.

temporary drying of the subcloud layer and a positive $\overline{w'q_t'}$ gradient. By contrast, when the cumulus activity is weak, the moisture in the subcloud layer is replenished by the surface flux and the $\overline{w'q_t'}$ gradient is negative. We believe that the sign difference in the $\overline{w'q_t'}$ gradient in Fig. 4.9d is thus in large part a reflection of the LES intermittency. The LES $\overline{w'q_t'}$ one hour earlier has indeed a shape that much more closely resembles the SCM. Siebesma et al. (2001) observed comparable intermittency in $\overline{w'q_t'}$ (see their Figure 4) and alleviated the problem by choosing a three-hour averaging period. However, due to the non steady-state nature of the ARM surface forcing, a longer averaging period for this case is not desirable. The temperature and moisture variances and covariance (Fig. 4.10) are quite similar to BOMEX and so are the differences between the LES and the SCM. One notable difference with BOMEX is the absence of a local maximum in $\overline{q_t'^2}$ near cloud base. Such a maximum is not present in ARM because the mean moisture profile (Fig. 4.8b) has a smaller gradient at cloud base compared to BOMEX (Fig. 4.3b).

Figure 4.11 shows examples of PDFs near cloud base (z=1060 m) and higher in the

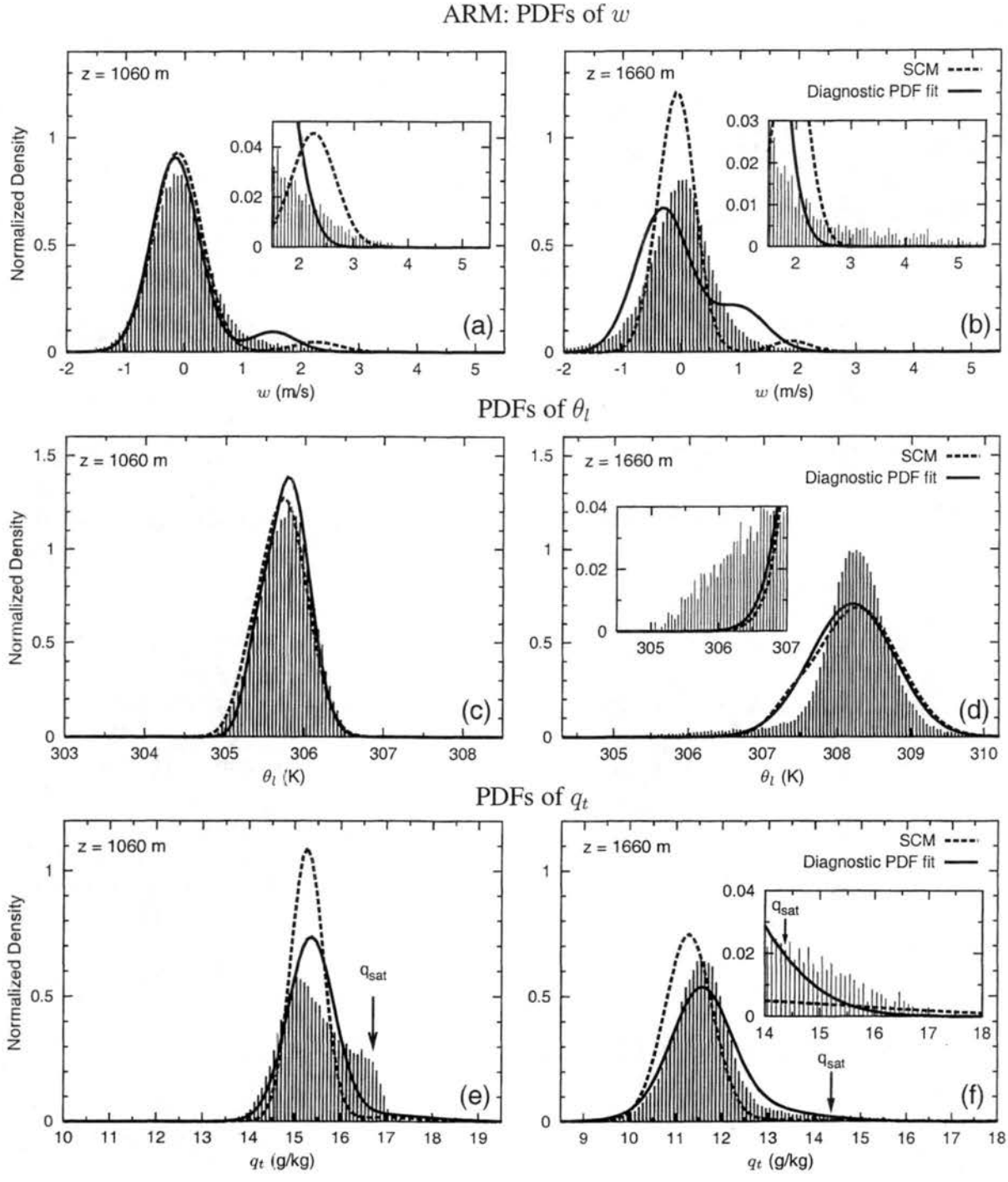

Figure 4.11: Examples of PDFs of w, θ_l, and q_t between 1900 and 2000 UTC of the ARM simulation. Thin vertical lines show the actual LES distributions, thick dashed lines the PDFs predicted by the SCM, and thick solid lines the PDF fits to the LES data. Vertical arrows in (e) and (f) indicate the mean state saturation specific humidity.

cloud (z=1660 m). In many respects, those PDFs are similar to BOMEX. The LES PDFs of w have long tails, extending to nearly 4 m s^{-1} at cloud base and 6 m s^{-1} in the middle of the cloud. The longer tail at 1660 m is due to the fact that w in the cloud cores increases between 1060 and 1660 m. The SCM and LES PDF fit produce positive tails, but they are not as elongated as in the original data. Interestingly, the SCM tails are longer than the diagnostic PDF fit, and therefore slightly more realistic. Recall from Fig. 4.9b that the SCM overpredicts $\overline{w'^3}$ between 1000 and 1600 m, and thus the resulting PDF is more elongated. The θ_l distribution at 1060 m (Fig. 4.11c) is nearly symmetrical with a Gaussian-like form. Both the SCM and the PDF fit represent it well, illustrating that the double Gaussian family of PDFs can reduce to a nearly single-Gaussian shape. At higher elevation (Fig. 4.11d), the distribution has a long negative tail. It is not captured well by either the SCM or the PDF fit since the family of PDFs used does not require the θ_l skewness of the fitted distribution to match the skewness of the underlying data. In the upper portion of the cloud, the PDF of q_t exhibits a long positive tail (Fig. 4.11f) formed by the cloud cores. The maximum specific humidity value in this tail (17 g kg^{-1}) is similar to the mean surface value (Fig. 4.8b). The diagnostic PDF fit captures the tail quite nicely, but the SCM underestimates the magnitude.

4.4 Stratocumulus (FIRE)

We now present results from the nocturnal stratocumulus cloud based on FIRE (see Section 2.2.4, p. 20). The SCM was configured and initialized similarly to the LES. The same simple longwave radiation transfer model was used (Eq. 2.3, p. 20). The vertical grid spacing was 25 m. The model time step was 6 s with a nested time step of 1.2 s. The relatively short time step was needed because the initial sounding (see Fig. 2.9, p. 21)

produces a high initial liquid water content and therefore a high initial longwave cloud-top cooling rate.

The LES and SCM were integrated for a total of three hours and the results shown are averaged over the last hour of the simulation. Figures 4.12a,b compare $\bar{\theta}_l$ and $\bar{q}_t$ from the LES and the SCM. Differences between the two appear mostly near the inversion region; the SCM produces an inversion in both $\bar{\theta}_l$ and $\bar{q}_t$ that is more smoothed out than that of the LES. The height of the inversion is also slightly lower in the parameterization, indicating a smaller entrainment rate. Consequences of these inversion layer differences can be seen in the plots of cloud fraction and water (Figs. 4.12c,d). The cloud fraction profiles, although very similar in shape and magnitude between the two models, appears to be shifted downward by 50 m for the parameterization. The smoother SCM inversion also leads to 40% less maximum liquid water in the SCM. Because the SCM's inversion is smoother, there is less total water available just below the inversion than in the LES (Fig. 4.12b), and therefore not as much condensed water. As a result, the LWP in the SCM (21.23 g m^2) is also smaller than in the LES (33.57 g m^2).

Cloud properties diagnosed by fitting the family of PDFs directly to the LES moments are almost identical to the LES cloud profiles (Figs. 4.12c,d). This indicates that, to the first order, the discrepancies in cloud fraction and liquid water between the SCM and the LES result from the poor prediction of certain moments by the SCM and not from the family of PDFs. However, the family of PDFs might play a secondary role if it is responsible for the poor prediction of these moments. Other possible factors leading to errors in the SCM moments include the damping terms or the numerical discretization of the predictive equations across the inversion layer. Because of the strong and complicated interaction between the PDF closure and the ten prognostic equations, it is unfortunately not clear to us

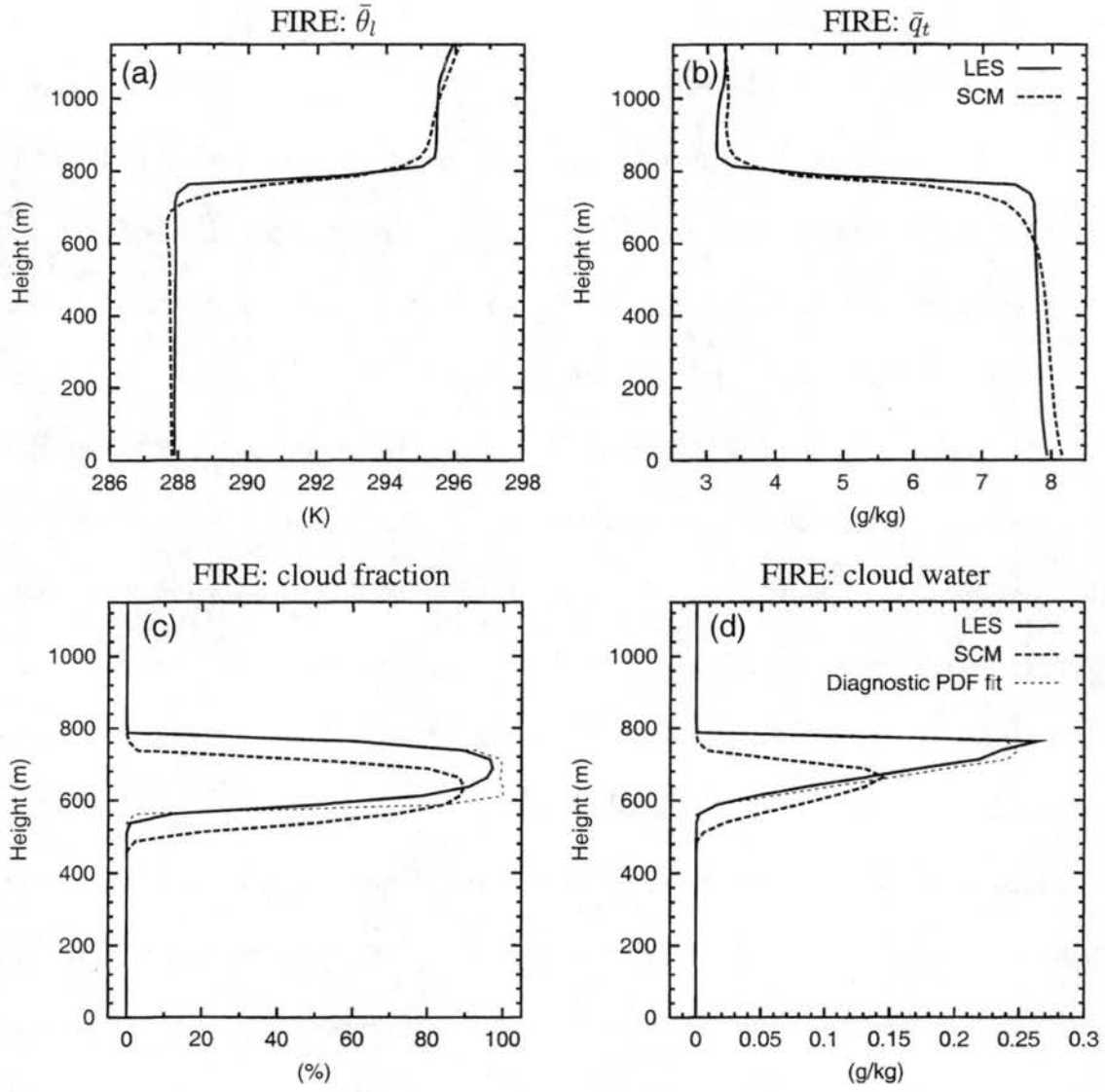

Figure 4.12: Mean profiles of liquid water potential temperature (a), total water specific humidity (b), cloud fraction (c), and liquid water (d) for the FIRE case. Thick solid lines LES results and thick dashed line SCM results, both averaged over the last hour of the simulation. Thin dashed lines in (c) and (d) show cloud properties obtained using a diagnostic PDF fit to the LES data.

if one factor in particular or a combination of factors are responsible for the misprediction of the moments.

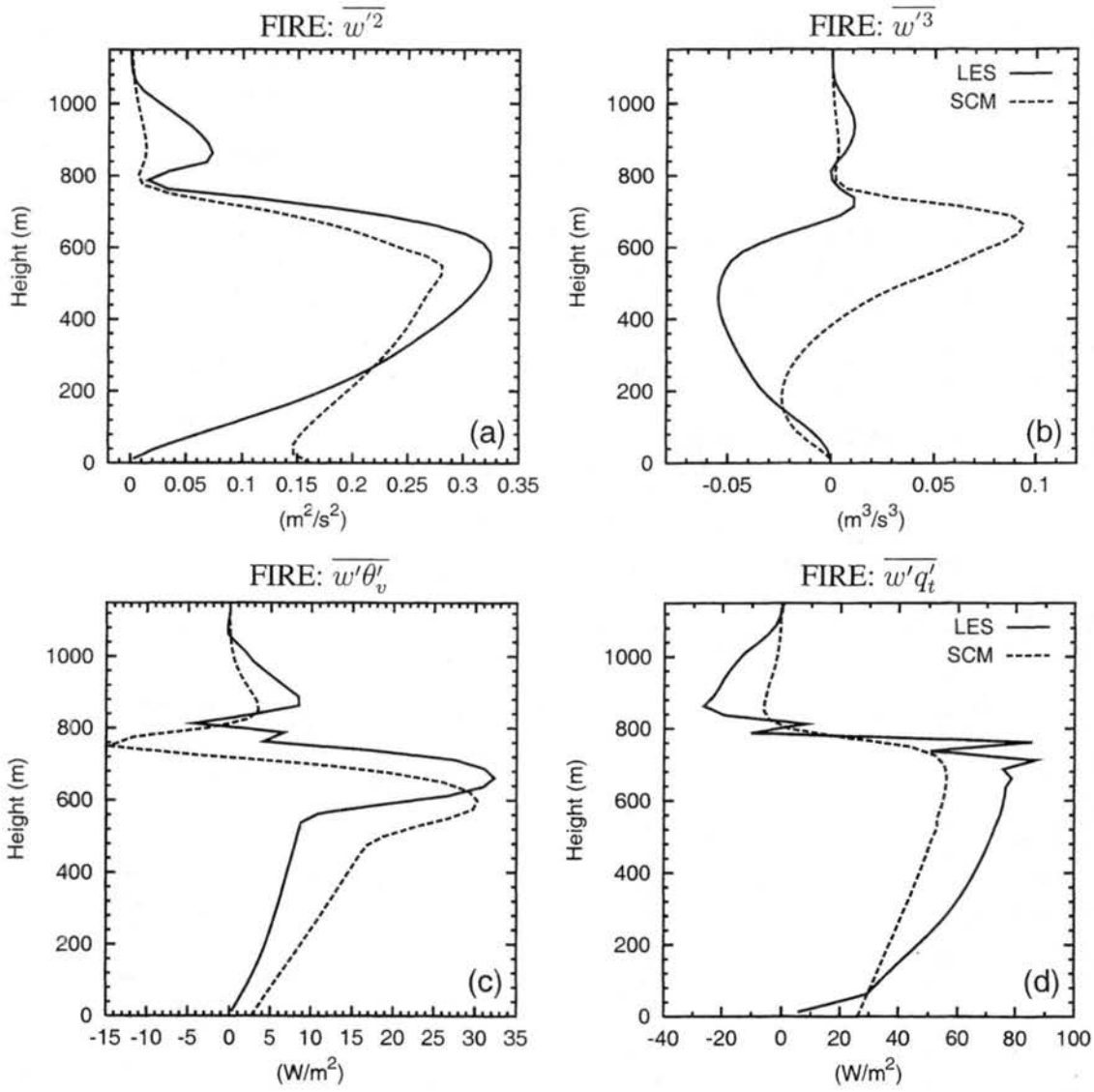

Figure 4.13: Profiles of $\overline{w'^2}$ (a), $\overline{w'^3}$ (b), $\overline{w'\theta'_v}$ (c), $\overline{w'q'_t}$ (d). Solid lines are LES results and dashed lines SCM outputs.

Profiles of the turbulent quantities $\overline{w'^2}$ and $\overline{w'^3}$ are shown in Figs. 4.13a,b. They are very different from the cumulus cloud layers and exhibits a large maximum near cloud top caused by the generation of turbulence by longwave radiative cooling. $\overline{w'^2}$ is similar

between the the LES and SCM, except near the surface and above the inversion. The secondary maximum in the LES above the inversion is related to wave activity in the stable layer. The LES $\overline{w'^3}$ is small compared to the cumulus cases because stratocumulus layers typically have little skewness. It is also negative throughout the entire boundary layer, which corresponds to relatively few and narrow downdrafts as one would expect for a cloud-topped cooling driven turbulence. $\overline{w'^3}$ is very different in the SCM. Negative values are only produced near the surface, and most of the layer has positive skewness with a maximum in $\overline{w'^3}$ just below cloud top that is not realistic. However, this discrepancy does not seem to degrade the overall simulation too much, possibly because skewness values in stratocumulus layers tend to be relatively small.

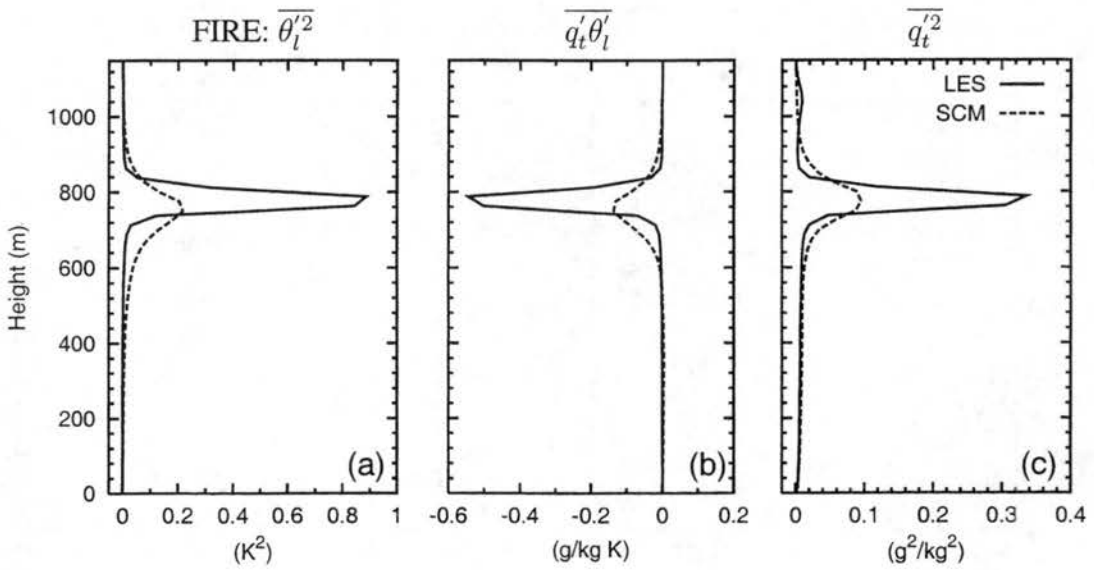

Figure 4.14: Profiles of $\overline{\theta_l'^2}$ (a), $\overline{q_t'\theta_l'}$ (b), and and $\overline{q_t'^2}$ (c) averaged over the last hour of the FIRE simulation. Solid lines are LES results and dashed lines SCM outputs.

The turbulent buoyancy and total water fluxes are depicted in Figs. 4.13c,d. The buoyancy flux peaks near cloud top. The SCM flux is slightly larger in the subcloud layer, but comparable in the cloud layer. The LES produces a larger value of total water flux throughout most of the boundary layer. The variances $\overline{\theta_l'^2}$ and $\overline{q_t'^2}$ as well as the covariance $\overline{q_t'\theta_l'}$

(Fig. 4.14) produced by the SCM are much smaller than the ones from the LES. Because the SCM predicted inversion is much smoother, the gradients of $\bar{\theta}_l$ and $\bar{q}_t$ produced by the SCM at cloud top are much smaller. This translates to considerably smaller turbulent production terms $\overline{w'\theta_l'}\frac{\partial\bar{\theta}_l}{\partial z}$ and $\overline{w'q_t'}\frac{\partial\bar{q}_t}{\partial z}$ appearing in the prognostic equations for $\overline{\theta_l'^2}$, $\overline{q_t'^2}$, and $\overline{q_t'\theta_l'}$.

Finally, Figure 4.15 shows some PDFs at 662 m (lower part of the cloud) and 787.5 m (just below LES cloud top). The LES PDFs are very different from the PDFs of cumulus layers. At 662 m, they have little skewness and tend to be narrow. The PDF of w extends from -1.5 to 1.5 m s^{-1} reflecting the smaller vertical velocities commonly observed in stratocumulus clouds. The spread is also much smaller along the θ_l and q_t axes than in cumulus layers. However, the picture is strikingly different just below LES cloud top. There, the PDF of w is even narrower, spanning a range of under 1 m s^{-1}, whereas the PDFs of temperature and moisture become extremely broad. This broadening results from two related factors: the entrainment of air from above the inversion into the cloud layer and the fact that the inversion top varies in altitude throughout the horizontal layer near cloud top. The PDF at 787.5 m therefore samples two air masses with very distinct characteristics. Overall, the diagnostic PDF fit produces reasonable fits to the underlying LES data at both heights. This shows that the family of PDFs is flexible enough to also fit relatively unskewed data. Because the SCM does not predict an accurate $\overline{w'^3}$ in the cloud layer, the SCM PDF of w at 662 m has a different shape from the LES. The SCM PDF of θ_l at the same height is too broad and shifted to the left. It is too broad because the SCM variance at this altitude is too large (Fig. 4.14a) and it is shifted to the left because $\bar{\theta}_l$ is slightly smaller than the LES (Fig. 4.12a). The SCM PDF of q_t at 662 m looks better, except that it is centered around a lower moisture value due to the smaller SCM $\bar{q}_t$. The SCM PDFs at 787.5 m are very different from the LES. This is not surprising since this level is *above* the SCM predicted

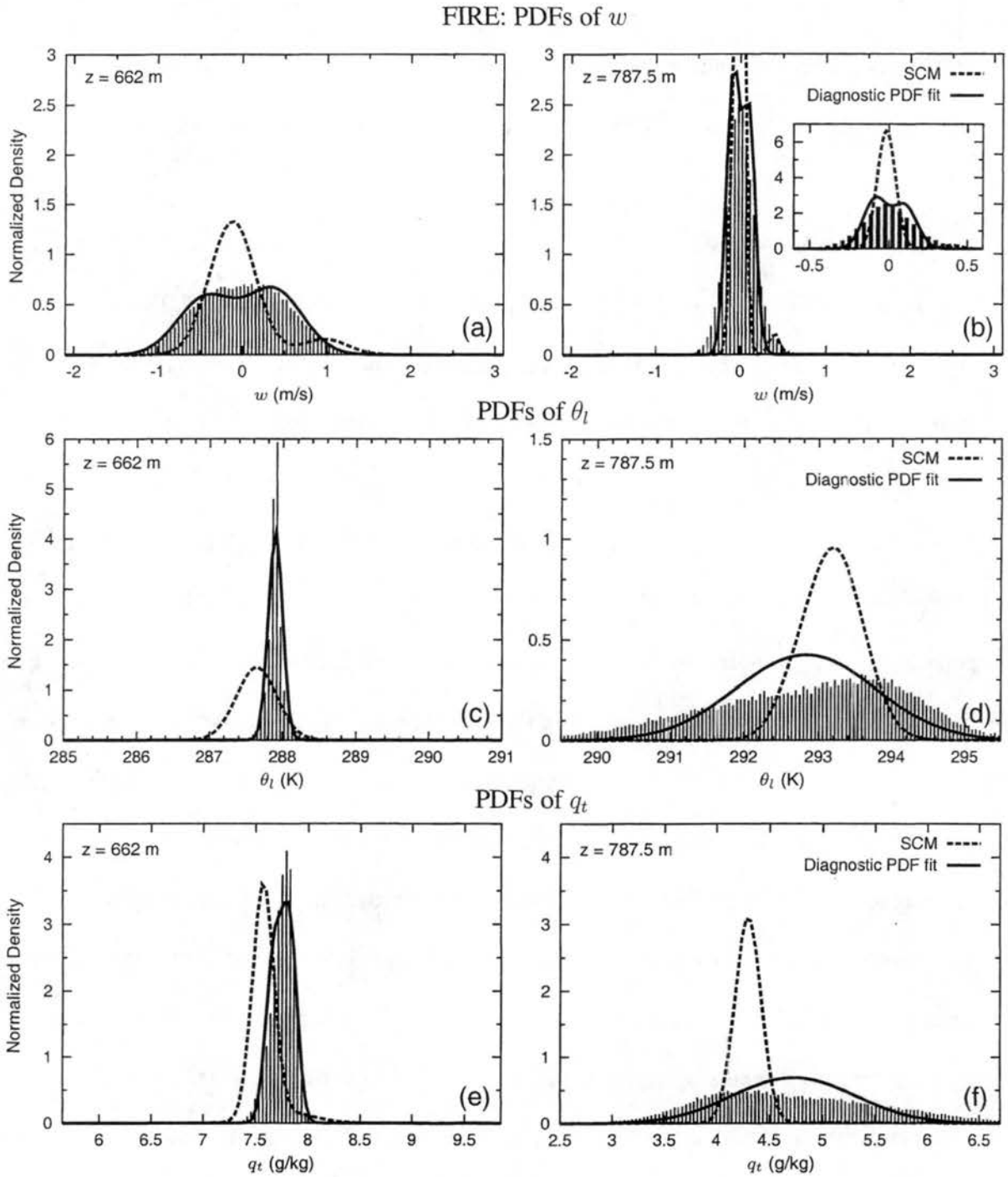

Figure 4.15: Examples of PDFs of w, θ_l, and q_t over the last hour of the FIRE simulation. Thin vertical lines show the actual LES distributions, thick dashed lines the PDFs predicted by the SCM, and thick solid lines the PDF fits to the LES data.

inversion, and thus samples only air with above-inversion characteristics, in contrast to the LES.

4.5 Mixed-regime (ATEX)

Finally, we present results from the mixed-regime case based on ATEX (see Section 2.2.5, p. 22). It should be noted that there was considerable spread between the results from different LES models for this particular case (Stevens et al. 2001). The RAMS LES can be thus considered to represent one particular realization from an ensemble of LES models with differing results. This complicates the evaluation of the SCM performance. But, to be consistent with our earlier evaluation of the SCM, we proceed with evaluating the SCM against the RAMS LES realization.

Initialization and configuration of the SCM was similar to the LES. The same vertical grid spacing of 20 m was used. The SCM main timestep was 10 s and the nested timestep was set to 2 s.

Comparison of the time evolution of the cloud fraction between the two models is depicted in Fig. 4.16. LES cloud base is located at 700 m and cloud top around 1500 m. Both remain stable during the course of the simulation, as the imposed large-scale subsidence almost exactly compensates cloud-top entrainment. The SCM predicted cloud base is lower by about 100 m and cloud top tends to rise slightly during the course of the simulation. The cloud fraction in the cumulus layer located between 700 m and 1300 m is smaller in the SCM than in the LES. The situation is reversed in the broken stratiform layer, where the maximum LES cloud fraction is of the order of 35% compared to 60% for the SCM.

The mean profiles of θ_l and q_t are shown in Fig. 4.17. As in Stevens et al. (2001), they are averaged over the last five hours of the simulation. The SCM produced $\bar{\theta}_l$ is cooler than the LES throughout most of the boundary layer. This is related to the fact that the SCM

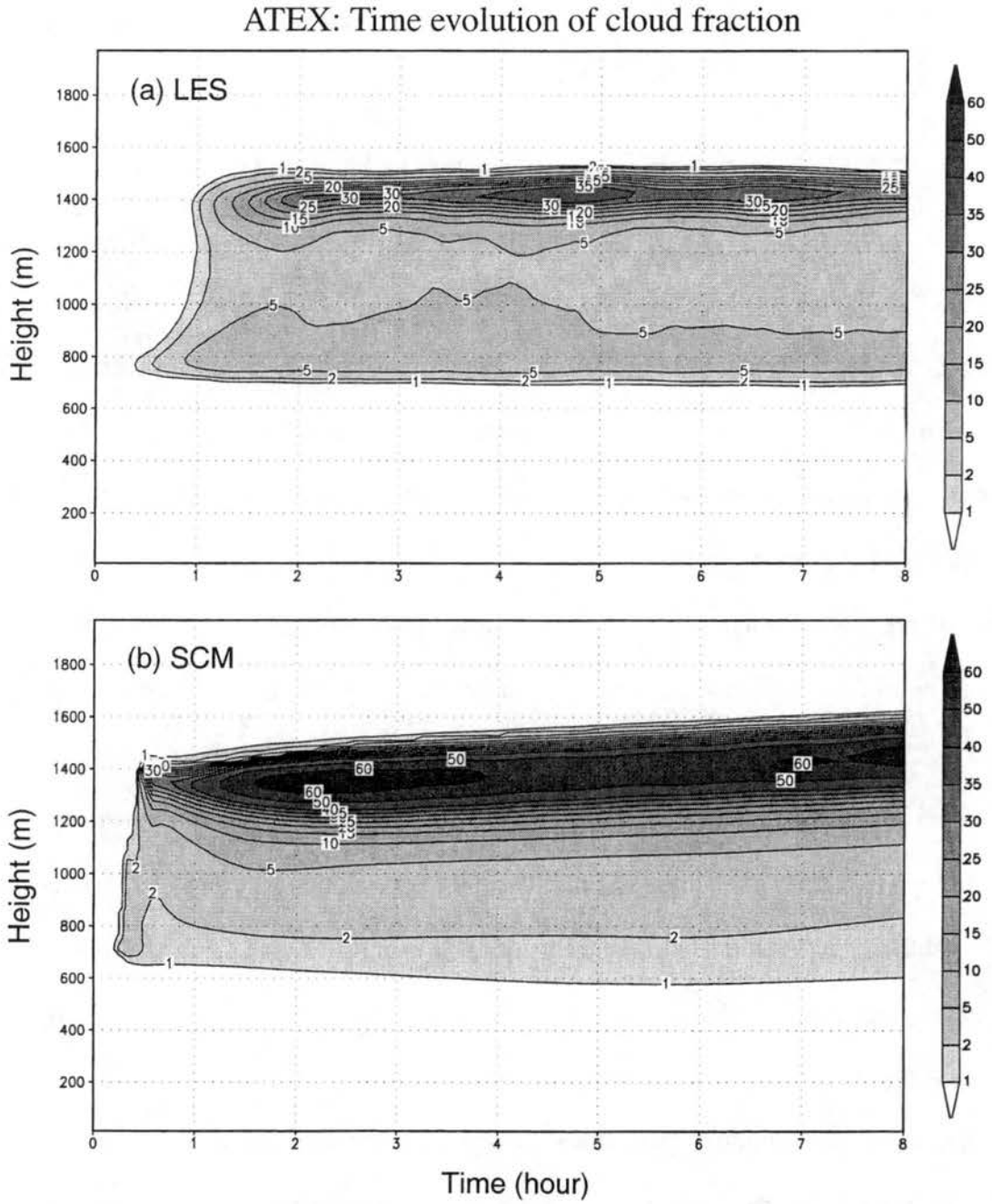

Figure 4.16: Time evolution of the cloud fraction (%) produced by the LES (a) and the SCM (b) for the ATEX case. A 60 minutes running average has been applied to the LES cloud fraction to smooth out intermittency in the cumulus layer.

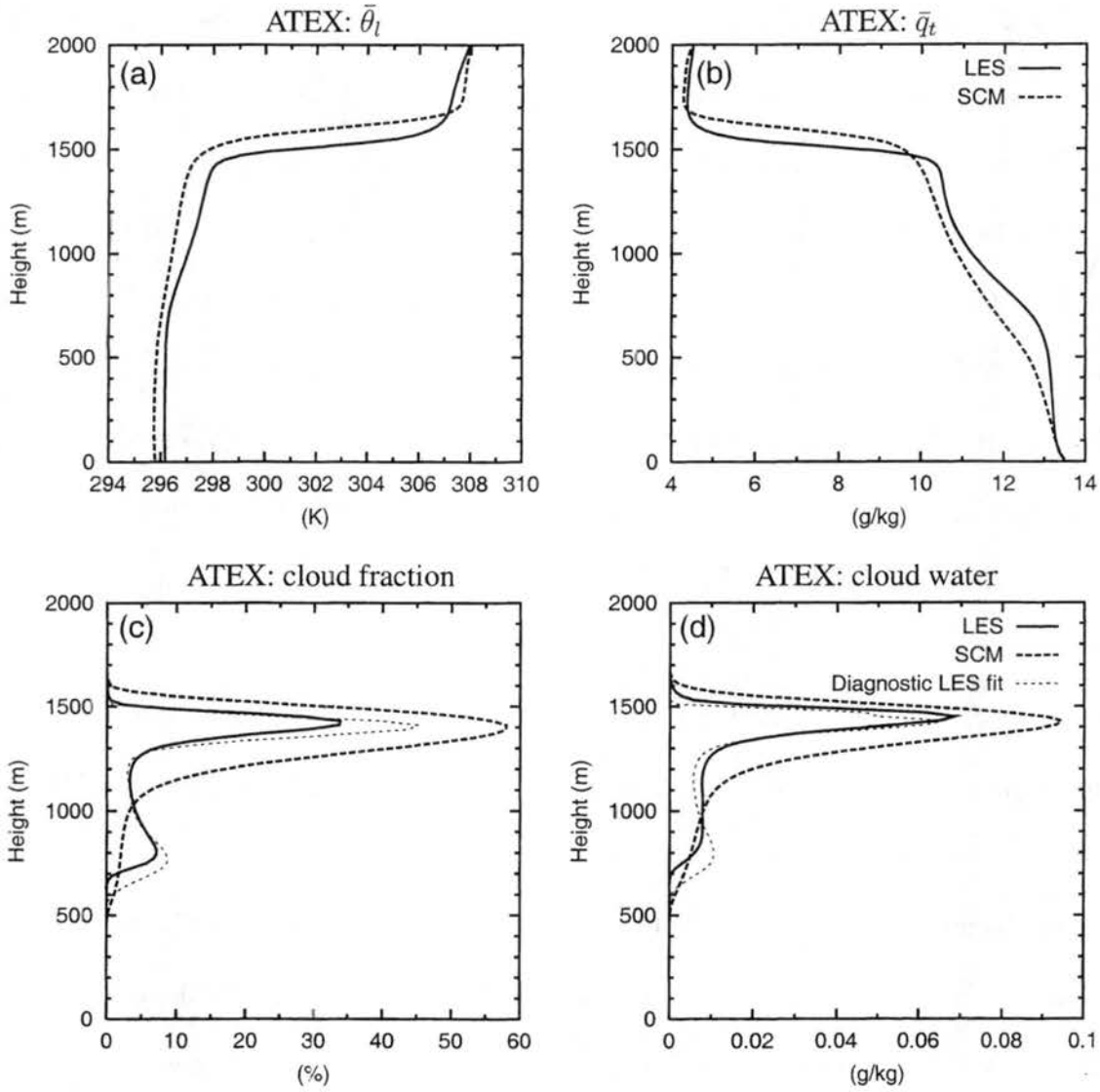

Figure 4.17: Mean profiles of liquid water potential temperature (a), total water specific humidity (b), cloud fraction (c), and liquid water (d) for the ATEX case. Thick solid lines LES results and thick dashed line SCM results, both averaged over the last five hours of the simulation. Thin dashed lines in (c) and (d) show cloud properties obtained using a diagnostic PDF fit to the LES data.

produces larger cloud fraction and liquid water values, which translate into larger longwave radiative cooling. The SCM $\bar{\theta}_l$ is also slightly better mixed in the layer between 700 m and 1400 m, because the larger cloud-top cooling induces a stronger turbulent mixing.

The SCM moisture gradient (Fig. 4.17b) is more uniform than in the LES. The LES produces two relatively well-mixed layers, one in the subcloud layer between the surface and 700 m and another near cloud top with a relatively large moisture gradient in between, whereas the SCM moisture profile decreases more uniformly with height. This leads to a smaller total moisture amount at the cumulus cloud base around 800 m in the SCM, and, in turn, translates into smaller SCM cloud amount at this altitude. As was the case for the stratocumulus, the SCM also tends to produce a smoother inversion near cloud top. The maximum LES cloud fraction in the cumulus layer is just under 10% compared to a few per cent in the SCM (Fig. 4.17c). As mentioned previously, the SCM exhibits a larger cloud cover than the LES in the stratiform layer. Differences in liquid water are similar (Fig. 4.17d), with the SCM overestimating condensate in the upper portion of the cloud by approximately 36%. This also results in an overestimation of the LWP. The SCM LWP is 27.0 g m^{-2} and the LES value is 13.9 g m^{-2}.

The diagnostic LES fits obtained by fitting the family of PDFs to the LES moments are also shown in Figs. 4.17c,d. They indicate that the family of PDFs is capable of accurately representing the cloud fraction and water profiles in this mixed-regime case. They also indicate that the misprediction of the moments explains a large fraction of the differences between the SCM and LES cloud properties.

Because of the differences in liquid water near cloud top and the use of an interactive longwave radiation, profiles of the turbulent moments in the LES and SCM are not strictly speaking directly comparable. They are displayed here with the caveat that other LES models with higher cloud amounts would have profiles of turbulent moments significantly

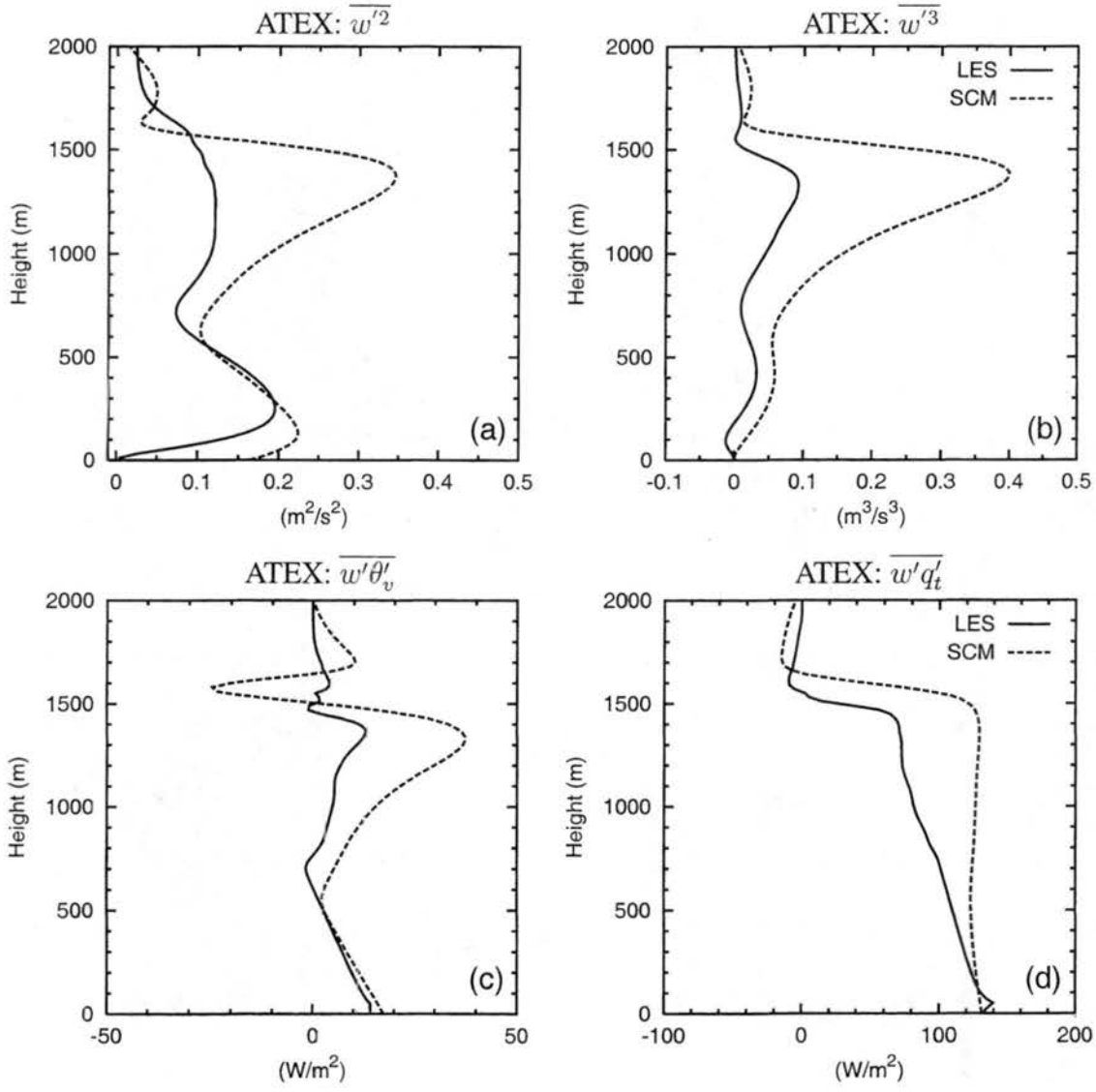

Figure 4.18: Profiles of $\overline{w'^2}$ (a), $\overline{w'^3}$ (b), $\overline{w'\theta'_v}$ (c), $\overline{w'q'_t}$ (d). Solid lines are LES results and dashed lines SCM outputs.

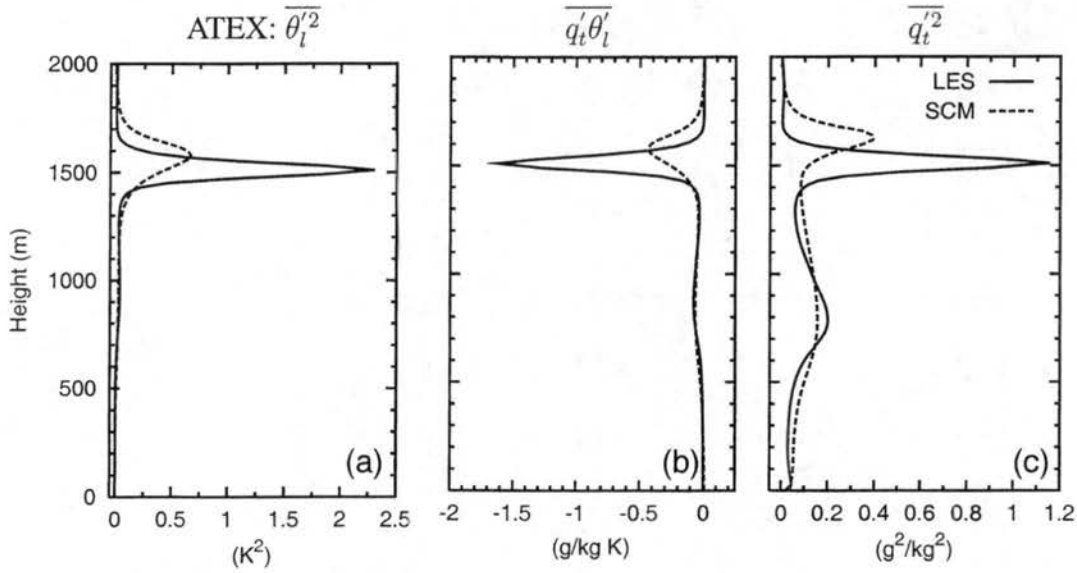

Figure 4.19: Profiles of $\overline{\theta_l'^2}$ (a), $\overline{q_t'\theta_l'}$ (b), and and $\overline{q_t'^2}$ (c) averaged over the last five hours of the ATEX simulation. Solid lines are LES results and dashed lines SCM outputs.

different from the RAMS LES. The variance and third-order of the vertical velocity are depicted in Figs. 4.18a,b. The subcloud profiles are comparable between the two models, but the cloud layer values are much larger in the SCM than the LES owing to the stronger cloud top cooling. Despite the differences in magnitude, the actual shapes of the profiles are however similar. The buoyancy flux (Fig. 4.18c) in the SCM is also much larger in the upper portion of the boundary layer. The SCM total water flux is larger and almost constant, whereas the LES flux decreases nearly uniformly with height (Fig. 4.18d). The differences in total water flux translate into differing total specific humidity profiles (Fig. 4.17b).

Finally, the second-order moments $\overline{\theta_l'^2}$, $\overline{q_t'\theta_l'}$ and $\overline{q_t'^2}$ are shown in Fig. 4.19. The magnitudes of the SCM moments are smaller than the LES, despite the stronger cloud-top cooling. The profiles and the differences between the two models closely resemble the nocturnal stratocumulus case (see Fig. 4.14, p. 84).

Overall, the comparison between the SCM and the RAMS LES for this particular is not

as good as the other test cases. This can, in part, be explained by the fact that we have showed comparisons with only one LES model realization. The SCM is, however, capable of representing the main characteristics of the cumulus under stratus regime, which in itself is a major advance for SCMs.

4.6 Sensitivity to vertical grid spacing

We conclude this chapter with sample results obtained with the SCM using a coarser vertical grid spacing to test the sensitivity to vertical resolution. We show results for three of the five cases. We select BOMEX, FIRE, and ATEX since they represent a wide range of boundary layer cloudiness regimes. The BOMEX and FIRE cases are both run with a vertical grid spacing that is doubled compared the original value, from 40 m to 80 m for BOMEX and from 25 m to 50 m for FIRE. Two additional runs are performed for the ATEX case, one with double (40 m) and one with quadruple (80 m) grid spacing.

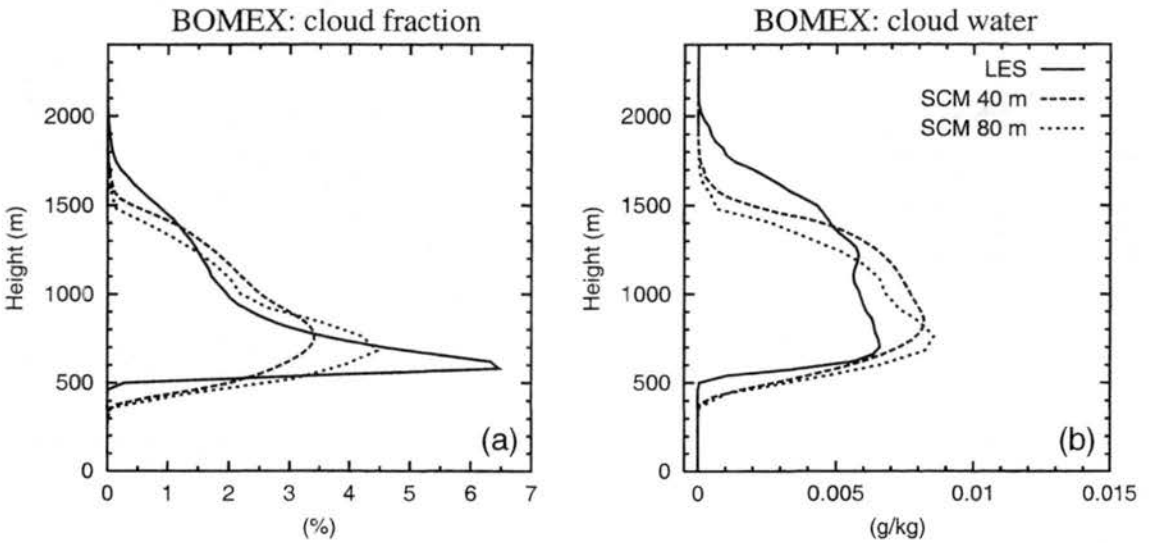

Figure 4.20: Profiles of cloud fraction (a), and cloud water (b) for the BOMEX case. Solid lines are LES results, long dashed lines SCM outputs with vertical grid spacing of 40 m, and short dashed lines SCM with grid spacing of 80 m.

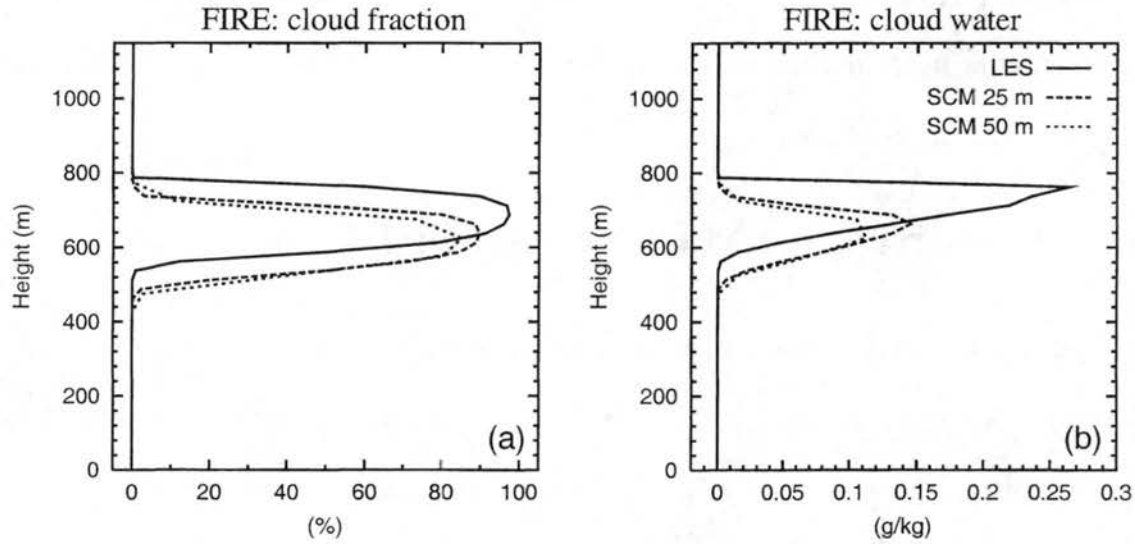

Figure 4.21: Profiles of cloud fraction (a), and cloud water (b) for the FIRE case. Solid lines are LES results, long dashed lines SCM outputs with vertical grid spacing of 25 m, and short dashed lines SCM with grid spacing of 50 m.

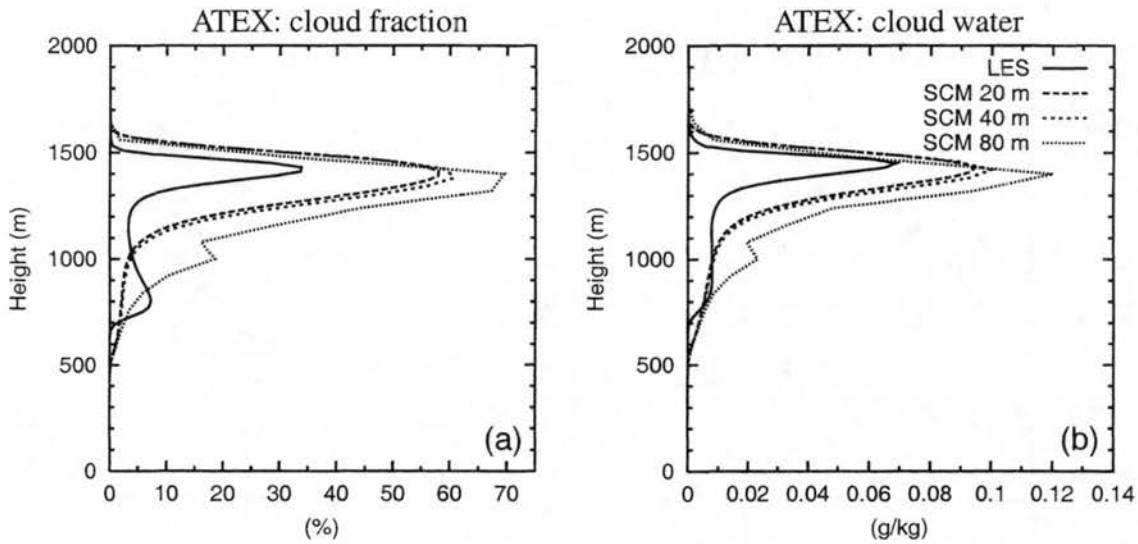

Figure 4.22: Profiles of cloud fraction (a), and cloud water (b) for the ATEX case. Solid lines are LES results, long dashed lines SCM outputs with vertical grid spacing of 20 m, short dashed lines SCM with grid spacing of 40 m, and dotted lines SCM with grid spacing of 80 m.

Figure 4.20 depicts the cloud fraction and liquid water for the BOMEX case. The differences between the 40 m and 80 m SCM simulations are rather small. The maximum value of cloud fraction is actually slightly better with the 80 m than with the 40 m grid spacing, but cloud top is lower with the coarser resolution. Liquid water profiles are similar with the main difference being the lower cloud top.

The results for the nighttime stratocumulus case are shown in Fig. 4.21. Compared to the 25 m grid spacing simulation, the 50 m run is slightly degraded and produces smaller cloud fraction and cloud water values. The maximum cloud fraction is approximately 85% compared to 90%, and the maximum liquid water 0.11 g kg^{-1} compared to 0.15 g kg^{-1} in the original simulation.

Finally, cloud properties for the ATEX case are depicted in Fig. 4.22. The differences between the 20 m and 40 m grid spacing simulations are almost negligible, indicating that 40 m is a sufficient grid spacing to resolve the vertical features for this particular case. However, the solution at 80 m shows signs of degradation. Both cloud fraction and cloud water become larger and depart further from the LES, especially in the cumulus layer underneath the broken stratocumulus deck.

Overall, it appears that a doubling of the vertical grid spacing still yields results with reasonable cloud properties. However, when the vertical grid spacing is further increased, the results start to degrade much more rapidly due to the model's inability to accurately resolve important features such as the presence of an inversion layer. In its current configuration, the parameterization performance is satisfactorily up a 50 to 80 m grid spacing. Above that, a modification to the numerical discretization to reconstruct the inversion (e.g. Grenier and Bretherton 2001) would probably be needed to obtain reasonable cloud properties.

Chapter 5

Summary and Conclusion

5.1 Model summary

A new cloudy boundary layer parameterization is described that utilizes a joint PDF for representing the subgrid-scale variability of vertical velocity, temperature, and moisture content. The PDF representation is incorporated into a higher-order turbulence closure model and is used to close all higher-order and buoyancy terms, as well as diagnose cloud fraction and liquid water, all in a manner consistent with the PDF. For each grid point and time step, a particular PDF is selected from an underlying family of PDFs, therefore allowing for the PDF to vary in space and evolve in time.

The family of PDFs used in this work is the LGC Double Gaussian proposed by Larson et al. (2001c). It is based on aircraft observations and LES model outputs of various types of boundary layer clouds, including shallow cumulus and stratocumulus clouds. This family of PDFs depends on ten free parameters. The values of these parameters are determined from the grid box mean values of the vertical velocity ($\bar{w}$), liquid water potential temperature ($\bar{\theta}_l$), total water specific humidity ($\bar{q}_t$), the six second-order moments ($\overline{w'\theta'_l}$, $\overline{w'q'_t}$, $\overline{q'_t\theta'_l}$, $\overline{w'^2}$, $\overline{\theta'^2_l}$, $\overline{q'^2_t}$), and the third-order moment of the vertical velocity ($\overline{w'^3}$). Filtered prognostic equations are integrated to yield the time evolution of these moments. The assumed PDF method can be summarized in three major steps that are carried out for each model time

step and at each grid box:

(i) Predict mean quantities and higher-order turbulent moments.

(ii) Use the predicted moments to select a PDF member from the family of PDFs.

(iii) Use the particular PDF selected to close higher-order moments and diagnose the buoyancy terms, cloud fraction, and liquid water.

5.2 Summary of results

Five test cases were used to evaluate the performance of the new PDF-based parameterization. The first case was a clear convective boundary layer based on day 33 of the Wangara experiment. The parameterization produced a reasonable time evolution of the mixed-layer growth, compared both to observations and LES. Mixed-layer temperatures were within a fraction of degree of the LES. The SCM predicted a layer which was slightly less well mixed than the LES. The boundary layer top was a little bit lower, reflecting slower entrainment.

The second case was a trade-wind cumulus layer based on BOMEX. The SCM was found to be capable of producing very low cloud fraction and liquid water values, similar to the LES. Maximum cloud fraction in the parameterization was 3.5% compared to 6% for the LES, and cloud water was approximately 30% larger than in the LES. Cloud base was underestimated by 100 m and cloud top by a few hundred meters. The profile of the vertical velocity variance was typical of a cumulus layer, with a region of maximum value in the cloud and a secondary maximum in the subcloud layer. The third-order moment of the vertical velocity, the turbulent fluxes, and the temperature and moisture variances all exhibited comparable profiles and magnitudes between the SCM and the LES. With the

exception of the moisture variance, these moments tended to drop off at a lower altitude in the parameterization due to the underestimation of cloud top height.

The parameterization was also tested with a case of cumulus clouds over land based on observations taken at the SGP ARM site. In contrast to BOMEX, this case had a diurnal variation, with the clouds forming on top of a previously clear convective layer and dissipating before sunset. The timing of the onset and decay of the clouds was very well captured by the parameterization. The evolution of the mean profiles of temperature and moisture during the course of the day was also represented accurately. Cloud fraction and liquid water were slightly smaller in the SCM. As was the case in BOMEX, cloud base height was lower in the parameterization by approximately 100 m, and so was cloud top, but by a larger margin. Overall, turbulent moments were comparable between the SCM and the LES, with differences similar to the ones observed in BOMEX.

The fourth case was a nocturnal stratocumulus-topped boundary layer with much larger cloud fraction and liquid water. Maximum liquid water was 40% lower in the SCM compared to the LES. This was attributed to the fact that the inversion at the top of the boundary layer was not as sharp in the parameterization as in the LES, therefore reducing the amount of total water available near cloud top. The turbulence statistics were comparable with the exception of the vertical velocity skewness. The SCM produced a positive skewness near cloud top that was not observed in the LES.

The last case was a mixed-regime case based on ATEX. It consisted of cumulus clouds rising into a broken stratocumulus layer. This is a particularly challenging case because it simultaneously involves the presence of two very different cloud regimes. In the past, parameterizations have typically been unable to simulate intermediate regimes like this one. The SCM was capable of reproducing the main characteristics features of this case, including the presence of cumulus underneath a broken stratiform cloud layer. In the cumulus

layer, the SCM produced cloud fraction values that were smaller than the LES. However, the condensate amount was comparable. In the broken stratiform cloud layer, the SCM produced larger cloud amounts. The maximum cloud fraction was 60% in the SCM compared to 35% in the LES. Liquid water at cloud top was overestimated by the SCM by approximately 36%.

In conclusion, the new SCM based on a PDF parameterization was tested with a variety of boundary layer regimes and was found to be capable of producing reasonable results without the need for any case-specific adjustments. It was able to capture a very low cloud fraction regime, such as a trade-wind cumulus layer, as well as a nearly solid stratocumulus layer. Overall, the amount of liquid water produced was typically within 40% of the LES. This is encouraging considering the fact that a wide range of liquid water values were represented in the different test cases, from 0.006 to 0.3 g kg^{-1}. We believe that this work demonstrates the potential of the assumed PDF method when used in conjunction with a flexible and realistic family of PDFs.

5.3 Suggestions for future research

The present work opens the door to some exciting future research opportunities. One direction involves the use of the subgrid-scale PDF to improve the representation of certain microphysical processes in numerical models. As of today, the vast majority of microphysical parameterizations neglect all subgrid-scale variability and compute the effect of all processes as if the grid box vertical velocity, temperature, and moisture were uniform. Because microphysical processes are generally non-linear, this leads to errors. In certain cases, these errors can become biases. Biases are worse than errors because they are systematic and do not even partially cancel out.

One of the microphysical process leading to biases is the autoconversion scheme based on the Kessler formulation (Kessler 1969) and variants thereof. Autoconversion is the process by which non precipitating cloud droplets formed by nucleation grow to larger sizes rain drops. When subgrid scale variability is neglected, Larson et al. (2001a) showed that the autoconversion rate is systematically underpredicted. Although the subgrid-scale PDF does not provide information about the spatial organization of the variability, it contains all the necessary information to remove such a bias.

Another important microphysical process is the activation of CCN and ice forming nuclei (IFN). The CCN and IFN activation depends critically on local supersaturations values, which in turn depend on the local, in cloud, vertical velocity. Microphysical parameterizations with explicit activation schemes typically use the grid box mean supersaturation to activate CCN and IFN. However, even in numerical models with grid boxes as small as a few kilometers, the grid box mean supersaturation can differ dramatically from local values due to its strong dependence on the local vertical velocity. Significant errors can therefore occur when the subgrid-scale variability is ignored. The assumed PDF method offers the opportunity to correct some of these errors and improve CCN and IFN activation by making use of the knowledge of the subgrid-scale variability provided by the PDF.

Another direction for future research work involves the generalization of the PDF method for the parameterization of deep convection. In theory, the assumed PDF framework should be able to represent subgrid-scale convection of any scale, including deep convection. The practical implementation is, however, likely to be more complicated than for boundary layer clouds. A more general and complicated family of PDFs is probably needed to represent the highly skewed PDFs observed in deep convective clouds. Also, because precipitation plays a crucial role in deep convection, the coupling of a microphysical scheme to a PDF parameterization would be needed. Additional source and sink terms

Appendix A

Fitting families of PDFs

This appendix describes how we solve for the parameters that specify the five families of PDFs, given moments calculated from LES outputs or prognosed by the SCM. We also list formulas for cloud fraction (C), average specific liquid water content ($\overline{q_l}$), and turbulent flux of liquid water ($\overline{w'q_l'}$).

A.1 Double Delta function

The double delta family of PDFs depends on 7 parameters. They are determined by the input moments: $\overline{w}$, $\overline{w'^2}$, $\overline{w'^3}$, $\overline{\theta_l}$, $\overline{w'\theta_l'}$, $\overline{q_t}$, and $\overline{w'q_t'}$. This function is given by

$$P_{dd} = a\delta(w - w_1)\delta(\theta_l - \theta_{l1})\delta(q_t - q_{t1}) + (1 - a)\delta(w - w_2)\delta(\theta_l - \theta_{l2})\delta(q_t - q_{t2}),$$

where $0 \leq a \leq 1$ is the relative amplitude of the first delta function, and $(w_1, \theta_{l1}, q_{t1})$ and $(w_2, \theta_{l2}, q_{t2})$ are the positions of the first and second delta functions, respectively, in (w, θ_l, q_t) space. To determine these parameters, we follow the procedure of Randall et al. (1992) and Lappen and Randall (2001a). The strategy is to relate these known moments to the PDF parameters using the definitions of the moments, e.g.,

$$\overline{w'^2} = \int_{-\infty}^{\infty} dw \int_{-\infty}^{\infty} d\theta_l \int_{-\infty}^{\infty} dq_t \; P_{dd}(w, \theta_l, q_t)(w - \overline{w})^2 = a(w_1 - \overline{w})^2 + (1 - a)(w_2 - \overline{w})^2.$$

We first compute a, w_1 and w_2 from $\overline{w}$, $\overline{w'^2}$, and $\overline{w'^3}$ via the following formulas (Randall et al. 1992; Lappen and Randall 2001a):

$$a = \frac{1}{2}\left(1 - \frac{Sk_w}{\sqrt{4 + Sk_w^2}}\right),$$

$$w_1 = \overline{w} + \sqrt{\overline{w'^2}}\sqrt{\frac{1-a}{a}},$$

and

$$w_2 = \overline{w} - \sqrt{\overline{w'^2}}\sqrt{\frac{a}{1-a}}.$$

Here $Sk_w = \overline{w'^3}/(\overline{w'^2}^{3/2})$ is the skewness of w. Next we compute θ_{l1} and θ_{l2} from $\overline{\theta_l}$ and $\overline{w'\theta_l'}$:

$$\theta_{l1} = \overline{\theta_l} - \frac{\overline{w'\theta_l'}}{w_2 - \overline{w}}$$

$$\theta_{l2} = \overline{\theta_l} - \frac{\overline{w'\theta_l'}}{w_1 - \overline{w}}.$$

We use analogous formulas to compute q_{t1} and q_{t2} from $\overline{q_t}$ and $\overline{w'q_t'}$. The procedure guarantees that the delta function PDF satisfies the fluxes $\overline{w'\theta_l'}$ and $\overline{w'q_t'}$, but does not guarantee accurate diagnosis of the scalar variances, $\overline{\theta_l'^2}$ and $\overline{q_t'^2}$. Despite the simplicity of the double delta function, use of this PDF in a numerical model still requires the prediction of $\overline{w'^3}$, which is non-trivial.

A.2 Single Gaussian

The single Gaussian family depends on 9 parameters. The input moments are: $\overline{w}$, $\overline{w'^2}$, $\overline{\theta_l}$, $\overline{w'\theta_l'}$, $\overline{q_t}$, $\overline{w'q_t'}$, $\overline{q_t'\theta_l'}$, $\overline{\theta_l'^2}$, and $\overline{q_t'^2}$. This function is given by (Stuart and Ord 1994, p. 511)

$$P_{sg}(w, \theta_l, q_t) = (2\pi)^{-3/2}\sqrt{|\mathbf{A}|}\exp\left[-\frac{1}{2}(x_i - \overline{x_i})A_{ij}(x_j - \overline{x_j})\right]. \qquad \text{(A.1)}$$

The indices i and j range from 1 to 3, and $x_1 = w$, $x_2 = \theta_l$, and $x_3 = q_t$. $\mathbf{A}$ is the inverse of the covariance matrix, $\mathbf{A} = \mathbf{C}^{-1}$, where

$$C_{ij} = \overline{(x_i - \overline{x_i})(x_j - \overline{x_j})}.$$

For the single Gaussian, we are spared the inconvenience of translating from moments to the PDF parameters, since the two are the same.

Given the PDF parameters, we need to compute cloud fraction C, mean specific liquid water content $\overline{q_l}$, and mean liquid water flux $\overline{w'q_l'}$. For a Gaussian PDF, these quantities are calculated as follows (see Lewellen and Yoh 1993; Sommeria and Deardorff 1977; Mellor 1977; Bougeault 1982; Chen 1991; Larson et al. 2001b). We first need to compute a quantity s, which equals q_l when $s > 0$ but also can be negative and is conserved under condensation. We find that

$$s = q_t - q_s(T_l, p)\frac{(1 + \beta q_t)}{[1 + \beta q_s(T_l, p)]}, \tag{A.2}$$

where

$$q_s(T_l, p) = \frac{R_d}{R_v}\frac{e_s(T_l)}{p - [1 - (R_d/R_v)]e_s(T_l)}, \tag{A.3}$$

$$\beta = \beta(T_l) = \frac{R_d}{R_v}\left(\frac{L}{R_d T_l}\right)\left(\frac{L}{c_p T_l}\right), \tag{A.4}$$

and

$$T_l \equiv T - \frac{L}{c_p} q_l. \tag{A.5}$$

Here q_s is the saturation specific humidity, e_s is the saturation vapor pressure over liquid, T_l is the liquid water temperature, T is temperature, L is the latent heat of vaporization, c_p

is the specific heat at constant pressure, and R_d and R_v are the gas constants for dry air and water vapor. Then it turns out that

$$C = \frac{1}{2}\left[1 + \text{erf}\left(\frac{\overline{s}}{\sqrt{2}\sigma_s}\right)\right] \tag{A.6}$$

and

$$\overline{q_l} = \overline{s}C + \frac{\sigma_s}{\sqrt{2\pi}}\exp\left[-\frac{1}{2}\left(\frac{\overline{s}}{\sigma_s}\right)^2\right]. \tag{A.7}$$

Here erf is the error function and σ_s is the standard deviation of s:

$$\sigma_s^2 = c_{\theta_l}^2\sigma_{\theta_l}^2 + c_{q_t}^2\sigma_{q_t}^2 - 2c_{\theta_l}\sigma_{\theta_l}c_{q_t}\sigma_{q_t}r_{q_t\theta_l},$$

where we have defined

$$c_{q_t} = \frac{1}{1 + \beta(\overline{T_l})q_s(\overline{T_l}, p)}$$

and

$$c_{\theta_l} = \frac{1 + \beta(\overline{T_l})\overline{q_t}}{[1 + \beta(\overline{T_l})q_s(\overline{T_l}, p)]^2}\frac{c_p}{L}\beta(\overline{T_l})q_s(\overline{T_l}, p)\left(\frac{p}{p_0}\right)^{R_d/c_p},$$

where p_0 is a reference pressure. Here σ_{θ_l} and σ_{q_t} are the respective standard deviations of θ_l and q_t. Also $r_{q_t\theta_l}$ is the correlation coefficient between q_t and θ_l. The flux of liquid water is given by

$$\overline{w'q_l'} = C\overline{w's'}, \tag{A.8}$$

where

$$\overline{w's'} = c_{q_t}\sigma_w\sigma_{q_t}r_{wq_t} - c_{\theta_l}\sigma_w\sigma_{\theta_l}r_{w\theta_l}.$$

Here σ_w is the standard deviation of w.

To derive the LGC Double Gaussian closure used in the SCM, the following formulas are essential building blocks:

$$\overline{w'^2q_l'} = \frac{1}{\sqrt{2\pi}\sigma_s}\left(\overline{w's'}\right)^2\exp\left[-\frac{1}{2}\left(\frac{\overline{s}}{\sigma_s}\right)^2\right],$$

$$\overline{\theta_l' q_l'} = \sigma_{\theta_l} \left(c_{q_t} \sigma_{q_t} r_{q_t \theta_l} - c_{\theta_l} \sigma_{\theta_l} \right) C,$$

and

$$\overline{q_t' q_l'} = \sigma_{q_t} \left(c_{q_t} \sigma_{q_t} - c_{\theta_l} \sigma_{\theta_l} r_{q_t \theta_l} \right) C.$$

A.3 LY Double Gaussian

The Lewellen-Yoh Double Gaussian family of PDFs depends on 12 parameters that can be determined by the input moments: $\overline{w}$, $\overline{w'^2}$, $\overline{w'^3}$, $\overline{\theta_l}$, $\overline{w'\theta_l'}$, $\overline{q_t}$, $\overline{w'q_t'}$, $\overline{\theta_l'^2}$, $\overline{q_t'^2}$, $\overline{q_t'\theta_l'}$, $\overline{\theta_l'^3}$, and $\overline{q_t'^3}$. This PDF is based on a double Gaussian form:

$$P_{LY}(w, \theta_l, q_t) = aG_1(w, \theta_l, q_t) + (1 - a)G_2(w, \theta_l, q_t),$$

where G_1 and G_2 are three-dimensional Gaussian PDFs, each representing one "plume":

$$G_1(w, \theta_l, q_t) = (2\pi)^{-3/2} \sqrt{|\mathbf{A}_1|} \exp \left[-\frac{1}{2} (x_i - x_{i1}) A_{ij1} (x_j - x_{j1}) \right]. \qquad \text{(A.9)}$$

The second plume G_2 has an analogous form. Here $\mathbf{A}_1 = \mathbf{C}_1^{-1}$ is the inverse of the covariance matrix of the within-plume correlations, where

$$C_{ij,1} = \overline{(x_i - x_{i1})(x_j - x_{j1})}.$$

Here i and j vary between 1 and 3, with $x_1 = w$, $x_2 = \theta_l$, and $x_3 = q_t$. The mean values of plume 1 are $x_{11} = w_1$, $x_{21} = \theta_{l1}$, and $x_{31} = q_{t1}$.

The PDF parameters are the amplitude of plume 1 (a); the means of plume 1 (w_1,q_{t1},θ_{l1}); the standard deviations of plume 1 (σ_{w1}, $\sigma_{q_t 1}$, $\sigma_{\theta_l 1}$); and the within-plume correlations of plume 1 ($r_{w\theta_l 1}$, $r_{wq_t 1}$, $r_{q_t \theta_l 1}$). There are analogous PDF parameters for the second plume. This leads to a total of 19 PDF parameters. Lewellen and Yoh (1993) use diagnostic assumptions to obtain these 19 parameters from the 12 prognosed moments. A detailed description of the procedure is provided in Lewellen and Yoh (1993) and is summarized here.

Lewellen and Yoh's PDF parameters satisfy the equations obtained by integrating the 12 relevant moments over the double Gaussian PDF. We list four of these equations; the others are analogous:

$$\bar{w} = aw_1 + (1-a)w_2$$

$$\overline{w'^2} = a\left[(w_1 - \bar{w})^2 + \sigma_{w1}^2\right] + (1-a)\left[(w_2 - \bar{w})^2 + \sigma_{w2}^2\right]$$

$$\overline{w'^3} = a\left[(w_1 - \bar{w})^3 + 3(w_1 - \bar{w})\sigma_{w1}^2\right] + (1-a)\left[(w_2 - \bar{w})^3 + 3(w_2 - \bar{w})\sigma_{w2}^2\right]$$

$$\overline{w'q_t'} = a\left[(w_1 - \bar{w})(q_{t1} - \overline{q_t}) + r_{wq_t1}\sigma_{w1}\sigma_{q_t1}\right] + (1-a)\left[(w_2 - \bar{w})(q_{t2} - \overline{q_t}) + r_{wq_t2}\sigma_{w2}\sigma_{q_t2}\right].$$

To satisfy these equations for the moments, we first select the skewness with the largest magnitude:

$$Sk_{max} = \max\left(|Sk_w|, |Sk_{\theta_l}|, |Sk_{q_t}|\right).$$

Then we compute a via

$$a = 0.75 \qquad \text{if } |Sk_{max}| < 0.84$$

$$a^6 - Sk_{max}^2(1-a) = 0 \qquad \text{if } |Sk_{max}| > 0.84.$$

The transcendental equation for a must be solved numerically.

Next we compute the locations, w_1 and w_2, and standard deviations, σ_{w1} and σ_{w2}, of the two Gaussians in the w-coordinate. First, we compute $B_w \equiv w_2 - w_1$ according to

$$B_w = \text{sign}(Sk_w)\sqrt{\overline{w'^2}}\left(\frac{|Sk_w|}{1-a}\right)^{1/3}.$$

Then we write

$$w_1 = \overline{w} - B_w(1-a)$$

$$w_2 = \overline{w} + B_w a$$

$$\sigma_{w1}^2 = \overline{w'^2} - B_w^2(1-a)(1+a+a^2)/(3a)$$

$$\sigma_{w2}^2 = \overline{w'^2} + B_w^2(1-a)^2/3.$$

Analogous formulas hold for the means and widths of the Gaussians in θ_l and q_t.

The within-plume correlation between w and θ_l is given by

$$r_{w\theta_l 1} = \frac{\overline{w'\theta_l'} - B_w B_{\theta_l} a(1-a)}{a\sigma_{w1}\sigma_{\theta_{l1}} + (1-a)\sigma_{w2}\sigma_{\theta_l 2}}. \tag{A.10}$$

Physically, we must have $-1 \leq r_{w\theta_l 1} \leq 1$. For certain values of the moments, however, the above formula yields a value outside this range. To avoid this, when $r_{w\theta_l 1} > 1$, we set $r_{w\theta_l 1} = 1 - r_{\text{thresh}}$. When $r_{w\theta_l 1} < -1$, we set $r_{w\theta_l 1} = -1 + r_{\text{thresh}}$. We choose $r_{\text{thresh}} = 0.05$. We find $r_{wq_t 1}$ and $r_{q_t\theta_l 1}$ using formulas analogous to (A.10). We use the same value of r_{thresh} to restrict $r_{wq_t 1}$ and $r_{q_t\theta_l 1}$ to physically possible values. Furthermore, we set the within-plume correlations in the two plumes equal: $r_{w\theta_l 2} = r_{w\theta_l 1}$ and $r_{wq_t 2} = r_{wq_t 1}$.

Despite the adjustments to the within-plume correlations, for some PDFs the determinant of $\mathbf{A}_1$, $|\mathbf{A}_1|$, can still turn out to be negative. In this case, the factor $\sqrt{|\mathbf{A}_1|}$ renders the PDF imaginary. To prevent this, we ensure

$$1/|\mathbf{A}_1| \propto 1 - r_{w\theta_l 1}^2 - r_{wq_t 1}^2 - r_{q_t\theta_l 1}^2 + 2r_{w\theta_l 1} r_{wq_t 1} r_{q_t\theta_l 1} > 0$$

by adjusting $r_{q_t\theta_l 1}$ such that

$$r_{w\theta_l 1} r_{wq_t 1} - \sqrt{(1 - r_{w\theta_l 1}^2)(1 - r_{wq_t 1}^2)} < r_{q_t\theta_l 1} < r_{w\theta_l 1} r_{wq_t 1} + \sqrt{(1 - r_{w\theta_l 1}^2)(1 - r_{wq_t 1}^2)}.$$

Finally, we set $r_{q_t\theta_l 2} = r_{q_t\theta_l 1}$.

Cloud fraction, $\overline{q_l}$, and $\overline{w'q_l'}$ for the Lewellen-Yoh scheme are

$$C = a(C)_1 + (1-a)(C)_2, \tag{A.11}$$

$$\overline{q_l} = a(\overline{q_l})_1 + (1-a)(\overline{q_l})_2, \tag{A.12}$$

and

$$\overline{w'q_l'} = a\left[(w_1 - \overline{w})(\overline{q_l})_1 + (\overline{w'q_l'})_1\right] + (1-a)\left[(w_2 - \overline{w})(\overline{q_l})_2 + (\overline{w'q_l'})_2\right]. \quad \text{(A.13)}$$

Here $(C)_1$, $(\overline{q_l})_1$, and $(\overline{w'q_l'})_1$ are given respectively by the single Gaussian eqns. (A.6), (A.7), (A.8), except that they are evaluated with respect to the mean and variances and covariances of Gaussian 1, which has amplitude a. Likewise, $(C)_2$, $(\overline{q_l})_2$, and $(\overline{w'q_l'})_2$ are associated with Gaussian 2.

In addition, we have the formulas

$$\begin{aligned} &\overline{w'^2 q_l'} \qquad \text{(A.14)} \\ &= a\left\{\left[(w_1 - \overline{w})^2 + \sigma_{w1}^2\right]\left[(\overline{q_l})_1 - \overline{q_l}\right] + 2(w_1 - \overline{w})(\overline{w'q_l'})_1 + (\overline{w'^2 q_l'})_1\right\} \\ &\quad + (1-a)\left\{\left[(w_2 - \overline{w})^2 + \sigma_{w2}^2\right]\left[(\overline{q_l})_2 - \overline{q_l}\right] + 2(w_2 - \overline{w})(\overline{w'q_l'})_2 + (\overline{w'^2 q_l'})_2\right\}, \end{aligned}$$

$$\overline{\theta_l' q_l'} = a\left[(\theta_{l1} - \overline{\theta_l})(\overline{q_l})_1 + (\overline{\theta_l' q_l'})_1\right] + (1-a)\left[(\theta_{l2} - \overline{\theta_l})(\overline{q_l})_2 + (\overline{\theta_l' q_l'})_2\right],$$

and

$$\overline{q_t' q_l'} = a\left[(q_{t1} - \overline{q_t})(\overline{q_l})_1 + (\overline{q_t' q_l'})_1\right] + (1-a)\left[(q_{t2} - \overline{q_t})(\overline{q_l})_2 + (\overline{q_t' q_l'})_2\right].$$

A.4 LGC Double Gaussian

The LGC family was proposed by Larson et al. (2001c). It depends on 10 parameters with the input moments given by: $\overline{w}$, $\overline{w'^2}$, $\overline{w'^3}$, $\overline{\theta_l}$, $\overline{w'\theta_l'}$, $\overline{q_t}$, $\overline{w'q_t'}$, $\overline{\theta_l'^2}$, $\overline{q_t'^2}$, and $\overline{q_t'\theta_l'}$.

Like the LY formulation, the LGC Double Gaussian families of PDFs is based on the double Gaussian:

$$P_{LGC}(w, \theta_l, q_t) = aG_1(w, \theta_l, q_t) + (1-a)G_2(w, \theta_l, q_t), \quad \text{(A.15)}$$

where G_1 and G_2 are Gaussians. For the LGC Double Gaussian, however, the parameters can be found analytically. To achieve this simplicity, we invoke several assumptions. First,

we assume that *subplume* variations in w are uncorrelated with those in q_t or θ_l. Then, if we let $i = 1$ or 2, the individual Gaussians are given by:

$$\begin{aligned} G_i(w,\theta_l,q_t) &= \frac{1}{(2\pi)^{3/2}\,\sigma_{wi}\,\sigma_{q_t i}\,\sigma_{\theta_l i}\,(1-r^2_{q_t\theta_l i})^{1/2}} \\ &\times \exp\left\{-\frac{1}{2}\left(\frac{w-(w_i-\bar{w})}{\sigma_{wi}}\right)^2\right\} \\ &\times \exp\left\{-\frac{1}{2(1-r^2_{q_t\theta_l i})}\left[\left(\frac{q_t-(q_{ti}-\bar{q}_t)}{\sigma_{q_t i}}\right)^2+\left(\frac{\theta_l-(\theta_{li}-\bar{\theta}_l)}{\sigma_{\theta_l i}}\right)^2\right.\right. \\ &\left.\left. -\,2r_{q_t\theta_l i}\left(\frac{q_t-(q_{ti}-\bar{q}_t)}{\sigma_{q_t i}}\right)\left(\frac{\theta_l-(\theta_{li}-\bar{\theta}_l)}{\sigma_{\theta_l i}}\right)\right]\right\}. \end{aligned}$$

The parameters of P_{LGC} are determined by the following procedure. If there is no variability in w, i.e. $\overline{w'^2} = 0$, then the skewness of w, $Sk_w \equiv \overline{w'^3}/(\overline{w'^2}^{3/2})$, is undefined and we cannot determine the PDF parameters. In the data, $\overline{w'^2} = 0$ never occurs. In a numerical model, however, $\overline{w'^2} = 0$ is an important special case. We assume that in this case the PDF reduces to a single delta function. If $\overline{w'^2} \neq 0$, then we determine the relative amplitude of the Gaussians, a, and the centers of the Gaussians in w-space, w_1 and w_2, by integrating over the PDF to obtain moment equations for $\overline{w}$, $\overline{w'^2}$, and $\overline{w'^3}$. We assume that the widths of the two Gaussians in w are equal, i.e. $\sigma_{w1} = \sigma_{w2}$. Then we find:

$$a = \frac{1}{2}\left\{1 - Sk_w\left[\frac{1}{4(1-\tilde{\sigma}_w^2)^3 + Sk_w^2}\right]^{1/2}\right\}, \tag{A.16}$$

$$\tilde{w}_1 \equiv \frac{w_1-\overline{w}}{\sqrt{\overline{w'^2}}} = \left(\frac{1-a}{a}\right)^{1/2}(1-\tilde{\sigma}_w^2)^{1/2}, \tag{A.17}$$

and

$$\tilde{w}_2 \equiv \frac{w_2-\overline{w}}{\sqrt{\overline{w'^2}}} = -\left(\frac{a}{1-a}\right)^{1/2}(1-\tilde{\sigma}_w^2)^{1/2}. \tag{A.18}$$

To avoid dividing by a vanishingly small number in Eqns. (A.17) and (A.18), we insist that $0.01 < a < 0.99$. We have defined $\tilde{\sigma}_w \equiv \sigma_{w1}/\sqrt{\overline{w'^2}} = \sigma_{w2}/\sqrt{\overline{w'^2}}$. We choose $\tilde{\sigma}_w^2 = 0.4$.

As shown below, the widths of the individual Gaussians in θ_l are permitted to differ in the LGC Double Gaussian, and likewise for q_t. The assumption that $\sigma_{w1} = \sigma_{w2}$ is relaxed in the LHH Double Gaussian family of PDFs.

Now we solve for θ_{l1} and θ_{l2} from the equations for $\overline{\theta_l}$ and $\overline{w'\theta'_l}$. If there is no variability in θ_l, i.e. $\overline{\theta_l'^2} = 0$, then we set the means of the Gaussians equal, $\theta_{l1} = \theta_{l2} = \overline{\theta_l}$, and the widths of the Gaussians in the θ_l direction to zero, $\sigma_{\theta_l 1} = \sigma_{\theta_l 2} = 0$. Otherwise, we set

$$\tilde{\theta}_{l1} \equiv \frac{\theta_{l1} - \overline{\theta_l}}{\sqrt{\overline{\theta_l'^2}}} = -\frac{\overline{w'\theta'_l} \Big/ \left(\sqrt{\overline{w'^2}}\sqrt{\overline{\theta_l'^2}}\right)}{\tilde{w}_2} \tag{A.19}$$

$$\tilde{\theta}_{l2} \equiv \frac{\theta_{l2} - \overline{\theta_l}}{\sqrt{\overline{\theta_l'^2}}} = -\frac{\overline{w'\theta'_l} \Big/ \left(\sqrt{\overline{w'^2}}\sqrt{\overline{\theta_l'^2}}\right)}{\tilde{w}_1}. \tag{A.20}$$

Although the widths of the Gaussians in the w direction are set equal, $\sigma_{w1} = \sigma_{w2}$, we allow the widths of the Gaussians in the θ_l direction, $\sigma_{\theta_l 1}$ and $\sigma_{\theta_l 2}$, to differ. Specifically, we integrate over the PDF to relate $\overline{\theta_l'^2}$ and $\overline{\theta_l'^3}$ to $\tilde{\sigma}_{\theta_l 1,2}$. We find

$$\frac{\sigma^2_{\theta_l 1}}{\overline{\theta_l'^2}} = \frac{3\tilde{\theta}_{l2}\left[1 - a\tilde{\theta}_{l1}^2 - (1-a)\tilde{\theta}_{l2}^2\right] - \left[Sk_{\theta_l} - a\tilde{\theta}_{l1}^3 - (1-a)\tilde{\theta}_{l2}^3\right]}{3a(\tilde{\theta}_{l2} - \tilde{\theta}_{l1})} \tag{A.21}$$

$$\frac{\sigma^2_{\theta_l 2}}{\overline{\theta_l'^2}} = \frac{-3\tilde{\theta}_{l1}\left[1 - a\tilde{\theta}_{l1}^2 - (1-a)\tilde{\theta}_{l2}^2\right] + \left[Sk_{\theta_l} - a\tilde{\theta}_{l1}^3 - (1-a)\tilde{\theta}_{l2}^3\right]}{3(1-a)(\tilde{\theta}_{l2} - \tilde{\theta}_{l1})}. \tag{A.22}$$

One difficulty of the expressions (A.21) and (A.22) is that the denominators vanish if $\tilde{\theta}_{l2} = \tilde{\theta}_{l1}$. Furthermore, a Gaussian cannot have negative width. Therefore we impose the condition

$$0 < \frac{\sigma^2_{\theta_l 1,2}}{\overline{\theta_l'^2}} < 100. \tag{A.23}$$

To find $\tilde{q}_{t1}$, $\tilde{q}_{t2}$, $\sigma^2_{q_t 1}$, and $\sigma^2_{q_t 2}$, we use equations that are exactly analogous to (A.19), (A.20), (A.21), (A.22), and (A.23), with q_t replacing θ_l everywhere.

Equations (A.21,A.22) depend on the skewness Sk_{θ_l}, and the analogous equations for q_t depend on Sk_{q_t}. However, we want the LGC Double Gaussian closures to be usable in models that eschew the computational burden of predicting Sk_{θ_l} or Sk_{q_t}. Therefore, we make a diagnostic assumption for these quantities, as does the single Gaussian PDF, which assumes that the skewnesses are zero, and as does the double delta PDF discussed above, which implicitly assumes relationships for Sk_{θ_l} and Sk_{q_t}. For the LGC Double Gaussians, we simply set $Sk_{\theta_l} = 0$. To better represent the skewness in cumulus layers, we set $Sk_{q_t} = 1.2Sk_w$. However, this leads to a noisy solution when $|\tilde{q}_{t2} - \tilde{q}_{t1}|$ is small and hence the denominators of the expressions for $\sigma^2_{q_t1}$ and $\sigma^2_{q_t2}$ are small. To reduce the noisiness, we adjust Sk_{q_t} so that the numerator becomes small when the denominator becomes small. Namely, we set $Sk_{q_t} = 1.2Sk_w$ when $|\tilde{q}_{t2} - \tilde{q}_{t1}| > 0.4$, we set $Sk_{q_t} = 0$ when $|\tilde{q}_{t2} - \tilde{q}_{t1}| < 0.2$, and we linearly interpolate between these extremes when $0.2 < |\tilde{q}_{t2} - \tilde{q}_{t1}| < 0.4$. These formulas for Sk_{θ_l} and Sk_{q_t} are expedient, but it would be worthwhile to attempt to construct more sophisticated and realistic formulas in the future. An approximate upper bound on the possible improvement can be gleaned from the performance of the Lewellen-Yoh scheme, which assumes that all skewnesses are prognosed.

Finally, to compute the within-plume correlations, $r_{q_t\theta_l1,2}$, we set $r_{q_t\theta_l1} = r_{q_t\theta_l2}$ and integrate over the PDF to obtain an equation for $\overline{q_t'\theta_l'}$. We find

$$r_{q_t\theta_l1,2} = \frac{\overline{q_t'\theta_l'} - a(q_{t1} - \overline{q_t})(\theta_{l1} - \overline{\theta_l}) - (1-a)(q_{t2} - \overline{q_t})(\theta_{l2} - \overline{\theta_l})}{a\sigma_{q_t1}\sigma_{\theta_l1} + (1-a)\sigma_{q_t2}\sigma_{\theta_l2}}. \tag{A.24}$$

If $\sigma_{q_t1}\sigma_{\theta_l1}$ and $\sigma_{q_t2}\sigma_{\theta_l2}$ have been set to zero, then the denominator of Eqn. (A.24) vanishes. In this case, we set $r_{q_t\theta_l1,2} = 0$. Since a correlation must lie between -1 and 1, we also insist that

$$-1 < r_{q_t\theta_l1,2} < 1.$$

The formulas for C, $\overline{q_l}$, $\overline{w'q_l'}$, and $\overline{w'^2 q_l'}$ are exactly as for the Lewellen-Yoh scheme [Eqns. (A.11), (A.12), (A.13), (A.15)] except that the within-Gaussian correlation between w and the conserved scalars vanishes: $r_{wq_t 1,2} = r_{w\theta_l 1,2} = 0$. Therefore, $(\overline{w's'})_{1,2}$, $(\overline{w'q_l'})_{1,2}$, and $(\overline{w'^2 q_l'})_{1,2}$ vanish.

A.5 LHH Double Gaussian

This family of PDFs depends on 10 parameters and uses the same input moments as the LGC family: $\overline{w}$, $\overline{w'^2}$, $\overline{w'^3}$, $\overline{\theta_l}$, $\overline{w'\theta_l'}$, $\overline{q_t}$, $\overline{w'q_t'}$, $\overline{\theta_l'^2}$, $\overline{q_t'^2}$, and $\overline{q_t'\theta_l'}$.

This scheme is exactly the same as LGC Double Gaussian except that we follow the procedure of Luhar et al. (1996) to find the widths and positions of the Gaussians in w. Luhar et al. (1996) proposed an analytic one-dimensional PDF that allows the widths of the individual Gaussians to differ and that reduces to a single Gaussian when $Sk_w = 0$. We modify their closure trivially to permit both negative and positive Sk_w. We also extend their closure to joint three-dimensional PDFs by following the procedure for the LGC Double Gaussian. The only formulas that change are those for the relative amplitude a (A.16), $\tilde{w}_1$ (A.17), and $\tilde{w}_2$ (A.18). They become, respectively,

$$a = \frac{1}{2}\left[1 - Sk_w \left(\frac{1}{4/M + Sk_w^2}\right)^{1/2}\right],$$

$$\tilde{w}_1 = m\tilde{\sigma}_{w1},$$

and

$$\tilde{w}_2 = -m\tilde{\sigma}_{w2}.$$

Here

$$M = \frac{(1+m^2)^3}{(3+m^2)^2 m^2},$$

$$\tilde{\sigma}_{w1} = \frac{\sigma_{w1}}{\sigma_w} = \left[\frac{(1-a)}{a(1+m^2)}\right]^{1/2},$$

$$\tilde{\sigma}_{w2} = \frac{\sigma_{w2}}{\sigma_w} = \left[\frac{a}{(1-a)(1+m^2)}\right]^{1/2},$$

and

$$m = \frac{2}{3}|Sk_w|^{1/3}.$$

These equations have the reasonable property that $\sigma_{w1} > \sigma_{w2}$ when Sk_w is positive, thereby producing a long tail in w. A long tail is on the opposite side of the PDF is produced when Sk_w is negative. When $Sk_w = 0$, this scheme reduces to a single Gaussian, and hence $\tilde{w}_1$ and $\tilde{w}_2$ vanish. This leads to infinite values of $\tilde{\theta}_{l1}$ (A.19), $\tilde{\theta}_{l2}$ (A.20), $\tilde{q}_{t1}$, and $\tilde{q}_{t2}$. To prevent this, we enforce $|\tilde{w}_1| > 0.05$ and $|\tilde{w}_2| > 0.05$.

Appendix B

List of Acronyms

ARM Atmospheric Radiation Measurement

ASTEX Atlantic Stratocumulus Experiment

ATEX Atlantic Trade Wind Experiment

BOMEX Barbados Oceanographic and Meteorological Experiment

CCN cloud condensation nuclei

FIRE First ISCCP Regional Experiment

GCSS GEWEX Cloud Study System

GEWEX Global Water and Energy Experiment

IFN ice forming nuclei

ISCCP International Satellite Cloud Climatology Project

LES large-eddy simulation

LGC Larson, Golaz and Cotton double Gaussian

LHH Luhar, Hibberd and Hurkley double Gaussian

LST Local Standard Time

LW long wave

LWP liquid water path

LY Lewellen and Yoh double Gaussian

NCAR National Center for Atmospheric Research

PDF probability density function

RAMS Regional Atmospheric Modeling System

SCM single-column model

SGP Southern Great Plains

SST sea surface temperature

SW short wave

UTC Universal Time Coordinate

References

Ackerman, A. S., O. B. Toon, and P. V. Hobbs, 1993: Dissipation of marine stratiform clouds and collapse of the marine boundary layer due to the depletion of cloud condensation nuclei by clouds. *Science*, **262**, 226–229.

Ackerman, A. S., O. B. Toon, D. E. Stevens, A. J. Heymsfield, V. Ramanathan, and E. J. Welton, 2000: Reduction of tropical cloudiness by soot. *Science*, **288**, 1042–1047.

Albrecht, B. A., 1981: Parameterization of trade-cumulus cloud amounts. *J. Atmos. Sci.*, **38**, 97–105.

Albrecht, B. A., 1989: Aerosols, cloud microphysics, and fractional cloudiness. *Science*, **245**, 1227–1230.

André, J. C., G. de Moor, P. Lacarrère, and R. du Vachat, 1976a: Turbulence approximation for inhomogeneous flows: Part I. The clipping approximation. *J. Atmos. Sci.*, **33**, 476–481.

André, J. C., G. de Moor, P. Lacarrère, and R. du Vachat, 1976b: Turbulence approximation for inhomogeneous flows: Part II. The numerical simulation of a penetrative convection experiment. *J. Atmos. Sci.*, **33**, 482–491.

André, J. C., G. de Moor, P. Lacarrère, G. Therry, and R. du Vachat, 1978: Modeling the 24-hour evolution of the mean and turbulent structures of the planetary boundary layer. *J. Atmos. Sci.*, **35**, 1861–1883.

André, J. C., P. Lacarrère, and K. Traoré, 1982: Pressure effects on triple correlations in turbulent convective flows. *Turbulent Shear Flows 3: Selected Papers from the Third International Symposium on Turbulent Shear Flows*, L. J. S. Bradbury, F. Durst, L. E. Launder, F. W. Schmidt, and J. H. Whitelaw, Eds., Springer Verlag, 243–252.

Arakawa, A. and W. H. Schubert, 1974: Interaction of a cumulus cloud ensemble with the large-scale environment, part I. *J. Atmos. Sci.*, **31**, 674–701.

Augstein, E., H. Riehl, F. Ostapoff, and V. Wagner, 1973: Mass and energy transports in an undisturbed Atlantic trade-wind flow. *Mon. Wea. Rev.*, **101**, 101–111.

Augstein, E., H. Schmidt, and F. Ostapoff, 1974: The vertical structure of the atmospheric planetary boundary layer in undisturbed trade winds over the Atlantic Ocean. *Bound.-Layer Meteor.*, **6**, 129–150.

Bechtold, P., C. Fravalo, and J. P. Pinty, 1992: A model of marine boundary-layer cloudiness for mesoscale applications. *J. Atmos. Sci.*, **49**, 1723–1744.

Bechtold, P., J. W. M. Cuijpers, P. Mascart, and P. Trouilhet, 1995: Modeling of trade wind cumuli with a low-order turbulence model: Toward a unified description of Cu and Sc clouds in meteorological models. *J. Atmos. Sci.*, **52**, 455–463.

Bechtold, P., S. K. Krueger, W. S. Lewellen, E. van Meijgaard, C.-H. Moeng, D. A. Randall, A. van Ulden, and S. Wang, 1996: Modeling a stratocumulus-topped PBL: Intercomparison among different one-dimensional codes and with large eddy simulation. *Bull. Amer. Meteor. Soc.*, **77**, 2033–2042.

Betts, A. K. and R. Boers, 1990: A cloudiness transition in a marine boundary layer. *J. Atmos. Sci.*, **47**, 1480–1497.

Bony, S. and K. A. Emanuel, 2001: A parameterization of the cloudiness associated with cumulus convection; Evaluation using TOGA COARE data. *J. Atmos. Sci.*, **58**, 3158–3183.

Bougeault, P., 1981a: Modeling the trade-wind cumulus boundary layer. Part I: Testing the ensemble cloud relations against numerical data. *J. Atmos. Sci.*, **38**, 2414–2428.

Bougeault, P., 1981b: Modeling the trade-wind cumulus boundary layer. Part II: A higher-order one-dimensional model. *J. Atmos. Sci.*, **38**, 2429–2439.

Bougeault, P., 1982: Cloud-ensemble relations based on the Gamma probability distribution for the higher-order models of the planetary boundary layer. *J. Atmos. Sci.*, **39**, 2691–2700.

Bougeault, P., 1985: The diurnal cycle of the marine stratocumulus layer: A higher-order model study. *J. Atmos. Sci.*, **42**, 2826–2843.

Bougeault, P. and J.-C. André, 1986: On the stability of the third-order turbulence closure for the modeling of the stratocumulus-topped boundary layer. *J. Atmos. Sci.*, **43**, 1574–1581.

Bougeault, P. and P. Lacarrère, 1989: Parameterization of orography-induced turbulence in a mesobeta-scale model. *Mon. Wea. Rev.*, **117**, 1872–1890.

Brown, A. R., 1999: The sensitivity of large-eddy simulations of shallow cumulus convection to resolution and subgrid model. *Quart. J. Roy. Meteor. Soc.*, **125**, 469–482.

Brown, A. R., R. T. Cederwall, A. Chlond, P. G. Duynkerke, J.-C. Golaz, M. Khairoutdinov, D. C. Lewellen, A. P. Lock, M. K. MacVean, C.-H. Moeng, R. A. J. Neggers, A. P. Siebesma, and B. Stevens, 2002: Large-eddy simulation of the diurnal cycle of shallow

cumulus convection over land. Accepted to *Quarterly Journal of the Royal Meteorological Society*.

Brümmer, B., E. Augstein, and H. Riehl, 1974: On the low-level wind structure in the Atlantic trade. *Quart. J. Roy. Meteor. Soc.*, **100**, 109–121.

Cahalan, R. F., W. Ridgway, W. J. Wiscombe, and T. L. Bell, 1994: The albedo of fractal stratocumulus clouds. *J. Atmos. Sci.*, **51**, 2434–2455.

Chen, C. and W. R. Cotton, 1987: The physics of the marine stratocumulus-capped mixed layer. *J. Atmos. Sci.*, **44**, 2951–2977.

Chen, J.-M., 1991: Turbulence-scale condensation parameterization. *J. Atmos. Sci.*, **48**, 1510–1512.

Clarke, R. H., A. J. Dyer, R. R. Brook, D. G. Reid, and A. J. Troup, 1971: The Wangara experiment: Boundary layer data. Technical Report 19, Division of Meteorological Physics, CSIRO, Australia.

Colucci, P. J., F. A. Jaberi, and P. Givi, 1998: Filtered density function for large eddy simulation of turbulent flows. *Phys. Fluids*, **10**, 499–515.

Cotton, W. R. and R. A. Anthes, 1989: *Storm and Cloud Dynamics*. Academic Press, 884 pp.

Cotton, W. R., R. A. Pielke Sr., R. L. Walko, G. E. Liston, C. J. Tremback, H. Jiang, R. L. McAnelly, J. Y. Harrington, and M. E. Nicholls, 2002: Rams 2001: Current status and future directions. Accepted to *Meteorology and Atmospheric Physics*.

Cuijpers, J. W. M. and P. G. Duynkerke, 1993: Large eddy simulation of trade wind cumulus clouds. *J. Atmos. Sci.*, **50**, 3894–3908.

Cuijpers, J. W. M., P. G. Duynkerke, and F. T. M. Nieuwstadt, 1996: Analyses of variance and flux budgets in cumulus-topped boundary layers. *Atmos. Res.*, **40**, 307–337.

Deardorff, J. W., 1966: The counter-gradient heat flux in the lower atmosphere and in the laboratory. *J. Atmos. Sci.*, **23**, 503–506.

Deardorff, J. W., 1972: Numerical investigation of neutral and unstable planetary boundary layers. *J. Atmos. Sci.*, **29**, 91–115.

Deardorff, J. W., 1974: Three-dimensional numerical study of the height and mean structure of a heated planetary boundary layer. *Bound.-Layer Meteor.*, **7**, 81–106.

Deardorff, J. W., 1980: Stratocumulus-capped mixed layers derived from a three-dimensional model. *Bound.-Layer Meteor.*, **18**, 495–527.

Donaldson, C., 1973: Construction of a dynamic model of the production of atmospheric turbulence and the dispersal of atmospheric pollutants. *Workshop on Micrometeorology,* Boston, D. A. Haugen, Ed., Amer. Meteor. Soc., 313–392.

Duynkerke, P. G. and A. G. M. Driedonks, 1987: A model for the turbulent structure of the stratocumulus-topped atmospheric boundary layer. *J. Atmos. Sci.*, **44**, 43–64.

Duynkerke, P. G. and A. G. M. Driedonks, 1988: Turbulent structure of a shear-driven stratus-topped atmospheric boundary layer: A comparison of model results with observations. *J. Atmos. Sci.*, **45**, 2343–2351.

Duynkerke, P. G., P. J. Jonker, A. Chlond, M. C. Van Zanten, J. Cuxart, P. Clark, E. Sanchez, G. Martin, G. Lenderink, and J. Teixeira, 1999: Intercomparison of three- and one-dimensional model simulations and aircraft observations of stratocumulus. *Bound.-Layer Meteor.*, **92**, 453–487.

Ebert, E. E., U. Schumann, and R. B. Stull, 1989: Nonlocal turbulent mixing in the convective boundary layer evaluated from large-eddy simulation. *J. Atmos. Sci.*, **46**, 2178–2207.

Germano, M., 1992: Turbulence: the filtering approach. *J. Fluid Mech.*, **238**, 325–336.

Golaz, J.-C., H. Jiang, and W. R. Cotton, 2001: A large-eddy simulation study of cumulus clouds over land and sensitivity to soil moisture. *Atmos. Res.*, **59-60**, 373–392.

Gregory, D. and P. R. Rowntree, 1990: A mass flux convection scheme with representation of cloud ensemble characteristics and stability-dependent closure. *Mon. Wea. Rev.*, **118**, 1483–1506.

Grenier, H. and C. S. Bretherton, 2001: A moist PBL parameterization for large-scale models and its application to subtropical cloud-topped marine boundary layers. *Mon. Wea. Rev.*, **129**, 357–377.

Hartmann, D. L., M. E. Ockert-Bell, and M. L. Michelsen, 1992: The effect of cloud type on Earth's energy balance: Global analysis. *J. Climate*, **5**, 1281–1304.

Holland, J. Z. and E. M. Rasmusson, 1973: Measurement of atmospheric mass, energy and momentum budgets over a 500-kilometer square of tropical ocean. *Mon. Wea. Rev.*, **101**, 44–55.

Kessler, E., 1969: *On the Distribution and Continuity of Water Substance in Atmospheric Circulation. Meteor. Monogr. No. 10.* Amer. Meteor. Soc., 84 pp.

Krueger, S. K., 1988: Numerical simulation of tropical cumulus clouds and their interaction with the subcloud layer. *J. Atmos. Sci.*, **45**, 2221–2250.

Krueger, S. K., G. T. McLean, and Q. Fu, 1995a: Numerical simulation of the stratus-to-cumulus transition in the subtropical marine boundary layer. Part I: Boundary-layer structure. *J. Atmos. Sci.*, **52**, 2839–2850.

Krueger, S. K., G. T. McLean, and Q. Fu, 1995b: Numerical simulation of the stratus-to-cumulus transition in the subtropical marine boundary layer. Part II: Boundary-layer circulation. *J. Atmos. Sci.*, **52**, 2851–2868.

Lappen, C.-L., 1999: The unification of mass flux and higher-order closure in the simulation of boundary layer turbulence. Ph.D. dissertation, Dept. of Atmospheric Science paper no 679, Colorado State University, Fort Collins, CO, USA, 329 pp.

Lappen, C.-L. and D. A. Randall, 2001a: Toward a unified parameterization of the boundary layer and moist convection. Part I: A new type of mass-flux model. *J. Atmos. Sci.*, **58**, 2021–2036.

Lappen, C.-L. and D. A. Randall, 2001b: Toward a unified parameterization of the boundary layer and moist convection. Part II: Lateral mass exchanges and subplume-scale fluxes. *J. Atmos. Sci.*, **58**, 2037–2051.

Lappen, C.-L. and D. A. Randall, 2001c: Toward a unified parameterization of the boundary layer and moist convection. Part III: Simulations of clear and cloudy convection. *J. Atmos. Sci.*, **58**, 2052–2072.

Larson, V. E., R. Wood, P. R. Field, J.-C. Golaz, T. H. Vonder Haar, and W. R. Cotton, 2001a: Systematic biases in the microphysics and thermodynamics of numerical models that ignore subgrid-scale variability. *J. Atmos. Sci.*, **58**, 1117–1128.

Larson, V. E., R. Wood, P. R. Field, J.-C. Golaz, T. H. Vonder Haar, and W. R. Cotton, 2001b: Small-scale and mesoscale variability of scalars in cloudy boundary layers: One-dimensional probability density functions. *J. Atmos. Sci.*, **58**, 1978–1994.

Larson, V. E., J.-C. Golaz, and W. R. Cotton, 2001c: Mesoscale variability in cloudy boundary layers: Joint three-dimensional probability density functions. Submitted to *Journal of the Atmospheric Sciences*.

Launder, B. E., 1975: On the effects of a gravitational field on the turbulent transport of heat and momentum. *J. Fluid Mech.*, **67**, 569–581.

Lenschow, D. H., 1998: Observations of clear and cloud-capped convective boundary layers, and techniques for probing them. *Buoyant Convection in Geophysical Flows*, E. J. Plate, E. E. Fedorovich, D. X. Viegas, and J. C. Wyngaard, Eds., Kluwer Academic Publishers, 185–206.

Lenschow, D. H., J. C. Wyngaard, and W. T. Pennell, 1980: Mean-field and second-moment budgets in a baroclinic, convective boundary layer. *J. Atmos. Sci.*, **37**, 1313–1326.

Lewellen, W. S. and S. Yoh, 1993: Binormal model of ensemble partial cloudiness. *J. Atmos. Sci.*, **50**, 1228–1237.

Lock, A. P., A. R. Brown, M. R. Bush, G. M. Martin, and R. N. B. Smith, 2000: A new boundary layer mixing scheme. Part I: Scheme description and single-column model tests. *Mon. Wea. Rev.*, **128**, 3187–3199.

Luhar, A. K., M. F. Hibberd, and P. J. Hurley, 1996: Comparison of closure schemes used to specify the velocity PDF in Lagrangian stochastic dispersion models for convective conditions. *Atmos. Environ.*, **30**, 1407–1418.

Lumley, J. L. and B. Khajeh-Nouri, 1974: Computational modeling of turbulent transport. *Advances in Geophysics,* Vol. 18A, Academic Press, 169–192.

Mason, P. J., 1994: Large-eddy simulation: A critical review of the technique. *Quart. J. Roy. Meteor. Soc.*, **120**, 1–26.

Mellor, G. L., 1977: The Gaussian cloud model relations. *J. Atmos. Sci.*, **34**, 356–358.

Meyers, M. P., R. L. Walko, J. Y. Harrington, and W. R. Cotton, 1997: New RAMS cloud microphysics parameterization. Part II: The two-moment scheme. *Atmos. Res.*, **45**, 3–39.

Millionshchikov, M., 1941: On the theory of homogeneous and isotropic turbulence. *C. R. Acad. Sci. URSS*, **32**, 145–161.

Moeng, C.-H., 1984: A large-eddy-simulation model for the study of planetary boundary-layer turbulence. *J. Atmos. Sci.*, **41**, 2052–2062.

Moeng, C.-H. and D. A. Randall, 1984: Problems in simulating the stratocumulus-topped boundary layer with a third-order closure model. *J. Atmos. Sci.*, **41**, 1588–1600.

Moeng, C.-H. and J. C. Wyngaard, 1984: Statistics of conservative scalars in the convective boundary layer. *J. Atmos. Sci.*, **41**, 3161–3169.

Moeng, C.-H. and J. C. Wyngaard, 1988: Spectral analysis of large-eddy simulations of the convective boundary layer. *J. Atmos. Sci.*, **45**, 3573–3587.

Moeng, C.-H. and J. C. Wyngaard, 1989: Evaluation of turbulent transport and dissipation closures in second-order modeling. *J. Atmos. Sci.*, **46**, 2311–2330.

Moeng, C.-H., W. R. Cotton, C. Bretherton, A. Chlond, M. Kairoutdinov, S. Krueger, W. S. Lewellen, M. K. MacVean, J. R. M. Pasquier, H. A. Rand, A. P. Siebesma, B. Stevens, and R. I. Sykes, 1996: Simulation of a stratocumulus-topped planetary boundary layer: Intercomparison among different numerical codes. *Bull. Amer. Meteor. Soc.*, **77**, 261–278.

Pielke, R. A., W. R. Cotton, R. L. Walko, C. J. Tremback, W. A. Lyons, L. D. Grasso, M. E. Nicholls, M. D. Moran, D. A. Wesley, T. J. Lee, and J. H. Copeland, 1992: A comprehensive meteorological modeling system – RAMS. *Meteor. Atmos. Phys.*, **49**, 69–91.

Pincus, R. and S. A. Klein, 2000: Unresolved spatial variability and microphysical process rates in large-scale models. *J. Geophys. Res.*, **105**, 27059–27065.

Randall, D. A., 1987: Turbulent fluxes of liquid water and buoyancy in partly cloudy layers. *J. Atmos. Sci.*, **44**, 850–858.

Randall, D. A., J. A. Coakley Jr., C. Fairall, R. A. Kropfli, and D. H. Lenschow, 1984: Outlook for research on subtropical marine stratiform clouds. *Bull. Amer. Meteor. Soc.*, **65**, 1290–1301.

Randall, D. A., Q. Shao, and C.-H. Moeng, 1992: A second-order bulk boundary-layer model. *J. Atmos. Sci.*, **49**, 1903–1923.

Riehl, H., T. C. Yeh, J. S. Malkus, and N. E. La Seur, 1951: The north-east trade of the Pacific Ocean. *Quart. J. Roy. Meteor. Soc.*, **77**, 598–626.

Rotstayn, L. D., 2000: On the "tuning" of autoconversion parameterizations in climate models. *J. Geophys. Res.*, **105**, 15495–15507.

Rotta, J., 1951: Statistiche theorie nichthomogener turbulenz. *Z. Phys.*, **129**, 547–572.

Schmidt, H. and U. Schumann, 1989: Coherent structure of the convective boundary layer derived from large-eddy simulations. *J. Fluid Mech.*, **200**, 511–562.

Siebesma, A. P. and J. W. M. Cuijpers, 1995: Evaluation of parametric assumptions for shallow cumulus convection. *J. Atmos. Sci.*, **52**, 650–666.

Siebesma, A. P., C. S. Bretherton, A. R. Brown, A. Chlond, J. Cuxart, P. G. Duynkerke, V. Grubisic, H. Jiang, M. Khairoutdinov, D. Lewellen, C.-H. Moeng, B. Stevens, and D. E. Stevens, 2001: An intercomparison study for cloud resolving models of shallow cumulus convection. Submitted to *Bulletin of the American Meteorological Society*.

Slingo, A., 1990: Sensitivity of the Earth's radiation budget to changes in low clouds. *Nature*, **343**, 49–51.

Sommeria, G. and J. W. Deardorff, 1977: Subgrid-scale condensation in models of non-precipitating clouds. *J. Atmos. Sci.*, **34**, 344–355.

Stevens, B., 1996: On the dynamics of precipitating stratocumulus. Ph.D. dissertation, Dept. of Atmospheric Science paper no 618, Colorado State University, Fort Collins, CO, USA, 140 pp.

Stevens, B., A. S. Ackerman, B. A. Albrecht, A. R. Brown, A. Chlond, J. Cuxart, P. G. Duynkerke, D. C. Lewellen, M. K. MacVean, R. A. J. Neggers, E. Sánchez, A. P. Siebesma, and D. E. Stevens, 2001: Simulations of trade wind cumuli under a strong inversion. *J. Atmos. Sci.*, **58**, 1870–1891.

Stuart, A. and J. K. Ord, 1994: *Kendall's Advanced Theory of Statistics*, volume 1. 6th edition, Edward Arnold, 676 pp.

Stull, R. B., 1988: *An Introduction to Boundary Layer Meteorology*. Kluwer Academic Publishers, 666 pp.

Tiedtke, M., 1989: A comprehensive mass flux scheme for cumulus parameterization in large-scale models. *Mon. Wea. Rev.*, **117**, 1779–1800.

Tiedtke, M., W. A. Heckley, and J. Slingo, 1988: Tropical forecasting at ECMWF: The influence of physical parameterization on the mean structure of forecasts and analyses. *Quart. J. Roy. Meteor. Soc.*, **114**, 639–664.

Twomey, S., 1974: Pollution and the planetary albedo. *Atmos. Environ.*, **8**, 1251–1256.

Walko, R. L., W. R. Cotton, M. P. Meyers, and J. Y. Harrington, 1995: New RAMS cloud microphysics parameterization. Part I: The single-moment scheme. *Atmos. Res.*, **38**, 29–62.

Wyant, M. C. and C. S. Bretherton, 1997: Numerical simulations and a conceptual model of the stratocumulus to trade cumulus transition. *J. Atmos. Sci.*, **54**, 168–192.

Wyngaard, J. C., O. R. Coté, and K. S. Rao, 1974: Modeling the atmospheric boundary layer. *Advances in Geophysics,* Vol. 18A, Academic Press, 193–211.

Xu, K.-M. and D. A. Randall, 1996: Evaluation of statistically based cloudiness parameterizations used in climate models. *J. Atmos. Sci.*, **53**, 3103–3119.